

Titre: Analysis and Modelling of Li-Ion Cells Degassing and Combustion
Title: under Thermal Runaway

Auteur: Vincent Goupil
Author:

Date: 2021

Type: Mémoire ou thèse / Dissertation or Thesis

Référence: Goupil, V. (2021). Analysis and Modelling of Li-Ion Cells Degassing and
Citation: Combustion under Thermal Runaway [Mémoire de maîtrise, Polytechnique
Montréal]. PolyPublie. <https://publications.polymtl.ca/10009/>

 **Document en libre accès dans PolyPublie**
Open Access document in PolyPublie

URL de PolyPublie: <https://publications.polymtl.ca/10009/>
PolyPublie URL:

**Directeurs de
recherche:** Étienne Robert
Advisors:

Programme: Génie mécanique
Program:

POLYTECHNIQUE MONTRÉAL

affiliée à l'Université de Montréal

**Analysis and Modelling of Li-Ion Cells Degassing and Combustion under
Thermal Runaway**

VINCENT GOUPIL

Département de génie mécanique

Mémoire présenté en vue de l'obtention du diplôme de *Maîtrise ès sciences appliquées*

Génie mécanique

Novembre 2021

POLYTECHNIQUE MONTRÉAL

affiliée à l'Université de Montréal

Ce mémoire intitulé :

Analysis and Modelling of Li-Ion Cells Degassing and Combustion under Thermal Runaway

présenté par **Vincent GOUPIL**

en vue de l'obtention du diplôme de *Maîtrise ès sciences appliquées*

a été dûment accepté par le jury d'examen constitué de :

Clara SANTATO, présidente

Étienne ROBERT, membre et directeur de recherche

Sylvain TURENNE, membre

DEDICATION

This thesis would not have been possible without the infinite support of my family. I warmly thank my parents, my sisters, and my grandparents for having been there throughout these two years.

This thesis is dedicated to you.

I would like to thank all the people I met or who accompanied me to Quebec for all the moments spent with you. Loïc, Jérémie, Constantin, Clara, you are much more than my roommates. Eva, you are part of my family. Guillaume, Florent, thank you for all these moments and all these discussions, I can't wait to see you again. Thanks to Maxime, Guillaume, Emile and all my friends in Quebec, I am happy to have shared this adventure with you. Thank you to my neighbours, Rose, Manu, Chloé, Jez, Alvin, the covid lockdown would not have been the same without you.

I thank my friends who stayed in France. Hugo, Gaëtan, Martin, Pierre-Emmanuel, Claude, Lisa, Matthieu, Julie, Tapo, Guillaume, and all the others, thank you for being there despite the distance and the time difference.

Finally, the best for last... This master's thesis would not have the same flavour without you, Jeanne. Thank you for brightening my life for the past few months. Thank you to your caring family. Your support, good humour and love have comforted me when I needed it most. I cherish every moment I spend with you.

Translation (traduction):

Ce mémoire n'aurait pas vu le jour sans le soutien infini de ma famille. Je remercie chaleureusement mes parents, mes sœurs ainsi que mes grands-parents pour avoir été là tout au long de ces deux années. Ce mémoire vous est dédié.

Je remercie toutes les personnes rencontrées ou m'ayant accompagné au Québec pour tous ces moments passés avec vous. Loïc, Jérémie, Constantin, Clara, vous êtes bien plus que mes coloc. Eva, tu fais partie de ma famille. Guillaume, Florent, merci pour tous ces moments et toutes ces discussions, j'ai hâte de vous revoir. Merci à Maxime, Guillaume, Emile et tous mes amis de

Québec, je suis heureux d'avoir pu partager cette aventure avec vous. Merci aux voisines et voisins, Rose, Manu, Chloé, Jez, Alvin, le confinement n'aurait pas été le même sans vous.

Je remercie mes amis restés en France. Hugo, Gaëtan, Martin, Pierre-Emmanuel, Claude, Lisa, Matthieu, Julie, Tapo, Guillaume, et tous les autres, merci d'avoir été là malgré la distance et le décalage horaire.

Enfin, la meilleure pour la fin... Ce mémoire n'aurait pas la même saveur sans toi, Jeanne. Merci d'éclairer ma vie depuis quelques mois. Merci à ta famille si bienveillante. Ton soutien, ta bonne humeur et ton amour m'ont réconforté quand j'en avais le plus besoin. Je chérie chaque instant passé avec toi.

ACKNOWLEDGEMENTS

I would like to warmly thank Professor Étienne Robert, my research supervisor. Your advice and your assistance through the project have been very helpful to me. Thank you for believing in me during these two years.

I would also like to thank Safran S.A. and particularly Caroline Gaya (Safran Electrical and Power) and Aurélie Boisard (Safran Tech) for their support during this project. The discussions we had during our regular meetings have been much appreciated, especially during these two years of pandemic. It is a pity we did not have the opportunity to meet in person.

I am also grateful to Telops and particularly to Jean-Philippe Gagnon for his expertise concerning the multispectral camera.

Last, but definitely not least, I would like to thank all my research colleagues: Cristian, Tanja, Pablo, Elie, Olivier, Kobra, Antonella, Jean, Yao, Dominic, Mathieu, Xavier, Marianne, Alain, and the others. It has been a pleasure to share the lab with all of you. You are always welcomed in France or wherever I live.

RÉSUMÉ

L'emballement thermique est un phénomène inhérent aux cellules lithium-ion à électrolyte liquide. Il se caractérise par une montée soudaine en température suivie d'une éjection de gaz à haute vitesse généralement accompagnée d'une flamme. Le phénomène ne dure que quelques secondes (i.e. entre 5 s et 30 s) mais libère une grande quantité d'énergie (i.e. jusqu'à 100 kJ) et de gaz inflammables et toxiques.

Dans ce travail, une revue de littérature sur l'emballement thermique est d'abord présentée. Celle-ci décrit le phénomène, retrace les différentes normes industrielles liées à cette instabilité thermique et présente les effets de paramètres tels que l'état de charge (SOC) et le vieillissement sur le comportement des cellules durant l'emballement thermique. Ensuite, des tests expérimentaux permettant d'étudier les effets du taux de chauffe et du vieillissement sont réalisés à l'aide d'un calorimètre à cône couplé à un système de chauffe. La composition du relâchement gazeux est étudiée grâce à un spectromètre de masse et deux spectromètres à particule permettent d'obtenir les distributions de taille. Des mesures de température par thermographie infrarouge sont aussi réalisées à l'aide d'une caméra multispectrale. Enfin, trois modélisations numériques de la combustion sont implémentées dans l'environnement Cantera.

Cette étude montre que le taux de chauffe a une influence sur la température initiale de l'emballement thermique, celle-ci étant plus importante lorsque la montée en température est plus rapide. Le taux de chauffe impacte aussi la chronologie de l'emballement thermique (i.e. emballement thermique spontané ou non). Les effets du vieillissement ne sont pas clairement identifiés dans le faible nombre d'expériences réalisées mais l'énergie dégagée durant l'emballement thermique semble être minimale pour les cellules vieilles de manière cyclique. Plusieurs espèces gazeuses (H_2 , H_2O , CO_2 , DMC, C_3H_6 , C_6H_6 et LiF) sont identifiées durant deux phases distinctes de dégazage. Deux pics de concentration sont identifiés dans la distribution de taille de particules, le premier se situant pour des particules de diamètre inférieur à 50 nm et le deuxième pour des particules de diamètre compris entre 100 nm et 150 nm. Enfin, les modélisations de combustion permettent d'approximer les températures de flamme produites lors des expériences d'emballement thermique et d'identifier les produits de combustion.

ABSTRACT

The thermal runaway is a phenomenon inherent to lithium-ion cells with liquid electrolyte, characterized by a sudden rise in temperature followed by a high-speed gas ejection that generally results in a flame. The phenomenon lasts only a few seconds (i.e. between 5 s and 30 s) but releases a large amount of energy (i.e. up to 100 kJ) as well as flammable and toxic gases.

In this work, a state of the art on the thermal runaway of Li-ion cells is first presented. It describes the phenomenon, gives an overview of the different industrial standards associated with this thermal instability, and presents the effects of parameters such as the state of charge (SOC) and cell ageing. The second part presents experimental tests that allow the effects of heating rate and ageing to be studied, carried out using a cone calorimeter coupled to a heating system. The outgassing composition is studied with a mass spectrometer and the particle distributions are obtained using two particle-size spectrometers. Temperature measurements based on infrared thermography are performed with a multispectral camera. Finally, three numerical models for the combustion of the outgassing are implemented in the Cantera software.

This study shows that the heating rate has an influence on the initial temperature of the thermal runaway, the latter being higher when the temperature increases more rapidly. The heating rate also impacts the timeline of the thermal runaway (i.e. spontaneous thermal runaway or not). The effects of ageing are not clearly identified because of the relatively small number of tests, but the heat release seems minimal for cells subjected to cyclic ageing. Several gas species (H_2 , H_2O , CO_2 , DMC, C_3H_6 , C_6H_6 and LiF) are identified during two distinct degassing phases. Two peaks are identified in the particle size distribution, the first one being for particles with a diameter smaller than 50 nm and the second one for particles with a diameter between 100 nm and 150 nm. Finally, the combustion models allow an approximation of the flame temperatures reached during the thermal runaway tests and the identification of the combustion products.

TABLE OF CONTENTS

DEDICATION	III
ACKNOWLEDGEMENTS	V
RÉSUMÉ.....	VI
ABSTRACT.....	VII
TABLE OF CONTENTS	VIII
LIST OF TABLES	XI
LIST OF FIGURES.....	XII
LIST OF SYMBOLS AND ABBREVIATIONS.....	XV
LIST OF APPENDICES	XVIII
CHAPTER 1 INTRODUCTION.....	1
CHAPTER 2 LITERATURE REVIEW.....	5
2.1 The thermal runaway phenomenon.....	5
2.1.1 General description	5
2.1.2 Causes and successive steps for thermal runaway	7
2.1.3 Gas production during thermal runaway.....	11
2.1.4 Safety approaches implemented in Li-ion cells	12
2.1.5 The ageing phenomenon	13
2.2 Certification standards.....	14
2.2.1 The DO-311A standard	14
2.2.2 Other standards.....	17
2.3 State of the art on the thermal runaway of Li-ion cells.....	19
2.3.1 Experimental studies	19
2.3.2 Solid phases modelling.....	25

2.3.3	Gas combustion modelling.....	27
2.4	Discussion on the test methods in certification standards.....	28
2.5	Project objectives	28
CHAPTER 3 TEST PROTOCOL AND MODELLING APPROACHES.....		30
3.1	Experimental methods.....	30
3.1.1	Equipment	30
3.1.2	Test protocol.....	35
3.1.3	Error analysis.....	36
3.2	Modelling	37
3.2.1	Modelling approaches	37
3.2.2	Critical discussion.	41
CHAPTER 4 ARTICLE 1: ANALYSIS OF LI-ION CELLS DEGASSING AND COMBUSTION UNDER THERMAL RUNAWAY		42
4.1	Abstract	42
4.2	Introduction	43
4.3	Experimental methodology	46
4.3.1	Li-ion cells and heating system.....	46
4.3.2	Cone calorimeter	47
4.3.3	Particle size spectrometers	47
4.3.4	Mass spectrometer.....	48
4.3.5	Infrared and high-speed cameras.....	49
4.3.6	Experimental methodology	49
4.4	Results	50
4.4.1	Cell, outgassing and flame temperature	50

4.4.2	Effect of the heating rate	55
4.4.3	Gas emission	58
4.5	Discussion	61
4.6	Conclusion.....	63
CHAPTER 5	AGEING EFFECTS	65
5.1	Design of experiment	65
5.2	Results and discussion.....	66
5.2.1	Temperatures	66
5.2.2	Heat release rate and total energy released	67
CHAPTER 6	MODELLING	69
6.1	0D simulation	69
6.2	1D simulations.....	72
6.2.1	Counterflow diffusion flame	72
6.2.2	Premixed flame	74
6.3	Critical analysis.....	77
CHAPTER 7	GENERAL DISCUSSION.....	79
CHAPTER 8	CONCLUSION, IMPACT AND OUTLOOK	81
8.1	Conclusion.....	81
8.2	Impact and outlook.....	81
REFERENCES	83
APPENDICES	91

LIST OF TABLES

Table 2.1: Incidents on Li-ion cell batteries (adapted from [11, 20, 21])	7
Table 2.2: Pre-failure processes and their description [3, 11, 16, 22].....	8
Table 2.3: Abbreviations used in Figure 2.2 [11]	10
Table 2.4: Procedures from the DO-311A standard.....	15
Table 2.5: Criteria tested in the different standards	18
Table 2.6: EUCAR hazard levels and descriptions [47]	19
Table 3.1: Description of the eight filters of the multispectral infrared camera	35
Table 3.2: Overview of the inputs/outputs of the 0D simulation	38
Table 3.3: Overview of the inputs/outputs of the counterflow diffusion flame model	40
Table 3.4: Overview of the inputs/outputs of the premixed flame model.....	40
Table 4.1: Maximum heat release rate and total energy released for the different heating rates...57	57
Table 4.2: Maximum volumetric smoke production rate and total volume of smoke for different heating rates.....57	57
Table 4.3: Mass loss for different heating rates	57
Table 4.4: Major venting duration for different heating rates.....	62
Table 5.1: Overview of the experiments	65

LIST OF FIGURES

Figure 1.1: Volumetric energy density as a function of specific energy density (Ni-Cd: nickel-cadmium; Ni-MH: nickel-metal hydride; PLiON: lithium polymer) [4], reproduced with permission	1
Figure 1.2: A fire induced by the Li-ion battery of a Tesla car.....	2
Figure 1.3: Structure of a 18650 Li-ion cell [7], reproduced with permission	3
Figure 2.1: Schematic representation of the heat-temperature-reaction loop	5
Figure 2.2: Heat generated by the different reactions and temperature of reaction (abbreviations in Table 2.3) [11], reproduced with permission	10
Figure 2.3: Cross-section of a typical 18650 Li-ion cell showing the PTC and the CID [33], reproduced with permission	13
Figure 2.4: A cone calorimeter used for combustion analysis [30], reproduced with permission.	20
Figure 2.5: Classic profiles of cell temperature (a) and HRR (b) for different SOC during the thermal runaway of 18650 LMO Li-ion cells [48], reproduced with permission	23
Figure 3.1: Picture of the cone calorimeter at Polytechnique Montreal.....	31
Figure 3.2: Picture of the SAMSUNG 18650 25R Li-ion cells	32
Figure 3.3: Schematic representation of the heating setup.....	33
Figure 3.4: High-speed camera recording of Li-ion cell TR.....	35
Figure 3.5: Schematic representation of the counterflow diffusion flame model.....	39
Figure 3.6: Schematic representation of the premixed flat flame	40
Figure 4.1: Li-ion cell temperature evolution during TR.....	44
Figure 4.2: Overview of the heating setup: schematic representation (a) and picture of the real setup with TC0, TC1 and TC2 visible (b)	47
Figure 4.3: Overview of the gas sampling line	48
Figure 4.4: The main stages of TR.....	50

Figure 4.5: Description of the temperature measurements	51
Figure 4.6: Frames extracted from high-speed infrared imaging, for an effective heating rate of 14°C/min. (a) Images taken just before TR when the casing temperature is 95 °C and the positive pole temperature is 130°C. (b) During TR, the positive pole and outgassing temperatures are 700°C and 450°C, respectively	52
Figure 4.7: Comparisons between the infrared camera and the thermocouple measurements	53
Figure 4.8: Infrared camera measurements of the positive pole temperature during combustion using a through-flame infrared filter	53
Figure 4.9: Frames extracted from infrared (a) and high-speed (b) imaging recorded during the thermal runaway of a Li-ion cell (both videos are available as supplemental material). The infrared frames were recorded with two broadband filters that have different temperature ranges. “t0” represents the opening of the security vent	54
Figure 4.10: First venting temperature of the cell as a function of the heating rate	55
Figure 4.11: Max TC1 and Max TC2 (a), Max TC3 (b) as functions of the heating rate	56
Figure 4.12: Comparison of mass spectrometry measurements between spontaneous (a) and non-spontaneous (b) TR. The first peak in both cases is associated with the initial venting without flames, while the second follows TR and combustion of the outgassing	58
Figure 4.13: Relative gas concentration for major species after calibration, during the first venting (a) and the combustion following the major venting (b). The error bars represent standard deviations	59
Figure 4.14: Particle size distributions measured by the number of particles (a) and by the mass of the particles (b) with the GRIMM spectrometer. The standard deviation is represented by the shaded area	60
Figure 4.15: Particle size distribution measured by the number of particles (a) and by the mass of the particles (b) with the SMPS spectrometer. The standard deviation is represented by the shaded area	61
Figure 4.16: Comparison before (a) and during (b) the major venting of the TR.....	62

Figure 5.1: Cell temperature at first venting as a function of CL	66
Figure 5.2: Maximum temperatures measured by TC1 (a) and TC2 (b) as functions of CL	67
Figure 5.3: Maximum temperatures measured by TC3 (a) and TC4 (b) as functions of CL	67
Figure 5.4: Maximum HRR (a) and total energy released (b) during the thermal runaway as functions of CL.....	68
Figure 6.1: Gas composition as a function of time for $\Phi = 0.5$ (a), $\Phi = 1$ (b) and $\Phi = 2$ (c)	70
Figure 6.2: Temperatures profiles over time for different fuel-air equivalence ratios.....	71
Figure 6.3: Enthalpy of combustion for different fuel-air equivalence ratios.....	71
Figure 6.4: Gas temperature as a function of the distance from the fuel inlet	73
Figure 6.5: Gas composition as a function of the distance from the fuel inlet.....	73
Figure 6.6: Volumetric heat release rate as a function of the distance from the fuel inlet.....	74
Figure 6.7: Gas temperature as a function of the distance from the inlet	75
Figure 6.8: Gas composition as a function of the distance from the inlet.....	76
Figure 6.9: Volumetric heat release rate as a function of the distance from the inlet.....	77
Figure 7.1: Comparison with or without the chimney for: (a) HRR and (b) smoke production rate. Uncertainties are represented as standard deviations	79

LIST OF SYMBOLS AND ABBREVIATIONS

AC	Alternating current
amu	Atomic mass unit
ANSI	American National Standards Institute
ARC	Accelerating rate calorimetry
BC	Black carbon
CID	Current interrupt device
CL	Capacity loss
DC	Direct current
DEC	Diethyl carbonate
DMC	Dimethyl carbonate
DOT	United States Department of Transportation
DSC	Differential scanning calorimetry
EC	Ethyl carbonate
EMC	Ethyl methyl carbonate
EU	European union
EUCAR	European Council for Automotive Research and Development
EV	Electric vehicle
FTIR	Fourier-transform infrared spectroscopy
GC-MS	Gas chromatography - Mass spectrometry
HeNe	Helium-neon
JIS	Japanese Industrial Standards
LCO	Lithium cobalt oxide
LFP	Lithium iron phosphate

Li	Lithium
Li-ion	Lithium-ion
LMO	Lithium manganese oxide
HRR	Heat release rate
IEC	International Electrotechnical Commission
IEEE	Institute of Electrical and Electronics Engineers
MS	Mass spectrometry
NCA	Lithium nickel cobalt aluminium oxides
NDIR	Non-dispersive infrared
Ni-Cd	Nickel-cadmium battery
Ni-MH	Nickel metal hydride battery
NMC	Lithium nickel manganese cobalt
PC	Propylene carbonate
PE	Polyethylene
PID	Proportional-integral-derivative
PP	Polypropylene
ppb	Parts per billion
PTC	Positive temperature coefficient
RTCA	Radio Technical Commission for Aeronautics
SAE	Society of Automotive Engineers
SEI	Solid electrolyte interface
SMPS	Scanning mobility particle sizer
SOC	State of charge
SSR	Solid-state relay

TC1	Thermocouple number one (near the negative pole of the cell)
TC2	Thermocouple number two (near the positive pole of the cell)
TC3	Thermocouple number three (2cm above the security vent of the cell)
TC4	Thermocouple number four (12cm above the security vent of the cell)
THC	Total hydrocarbons
TR	Thermal runaway
UL	Underwriters laboratories
UN	United Nations

LIST OF APPENDICES

Appendix A	Wiring diagram of the setup	91
Appendix B	Smoke obscuration system (taken from S.C. Boenta)	92
Appendix C	Uncertainty on the heat release rate (HRR)	93
Appendix D	Governing equations for the 0D simulation	95
Appendix E	Governing equations for the 1D simulations	97

CHAPTER 1 INTRODUCTION

The strong incentives to use renewable energies to replace fossil fuels and the rapid growth in portable electronic devices during the past three decades have pushed the development of light and rechargeable batteries with high energy density [1]. The lithium-ion (Li-ion) battery technology has become the main electricity storage technology in several fields: cell phones, laptops, electric vehicles, aeronautics, etc. This technology replaced metallic lithium batteries, which have safety issues caused by dendrites formation. It provides better energetic performances, in terms of mass and volumetric energy densities, than older battery technologies such as lead-acid, nickel-cadmium or nickel-metal hydride batteries, as shown in Figure 1.1 [1, 2]. Li-ion battery can also deliver higher electrical voltage (up to 3.6V) than these other technologies, which means that they are useable in high-power applications. Moreover, Li-ion batteries don't require a large amount of poisonous metals such as lead, mercury or cadmium [3].

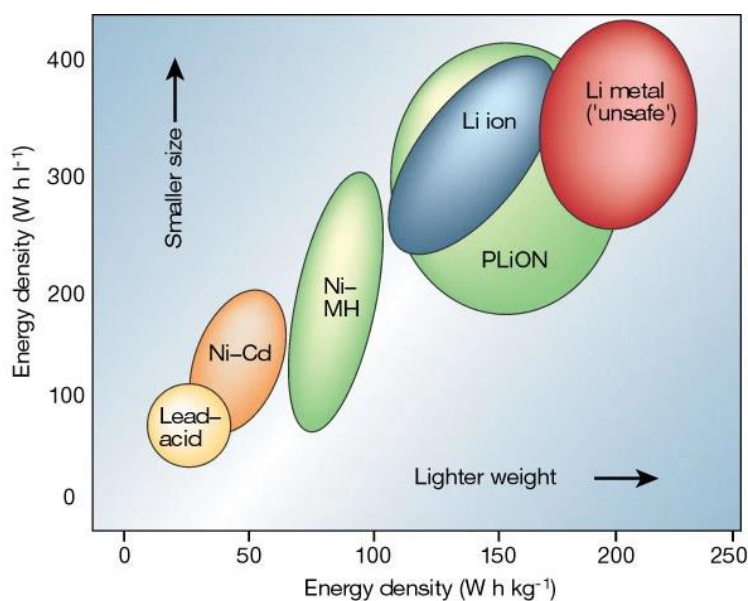


Figure 1.1: Volumetric energy density as a function of specific energy density (Ni-Cd: nickel-cadmium; Ni-MH: nickel-metal hydride; PLiON: lithium polymer) [4], reproduced with permission

Nevertheless, Li-ion cells with liquid electrolyte are subject to thermal runaway, a thermal instability that represents a significant risk when the cells are under abusive conditions (e.g. a fire, a mechanical damage, a short-circuit, or an overcharge) [1, 3, 5]. During this phenomenon, the cells experienced a rapid increase of temperature followed by a violent gas venting, often resulting in the apparition of a large flame. The consequence of such a phenomenon can be

catastrophic when a cell is part of a battery pack, triggering a potential chain reaction to the adjacent cells. Moreover, the outgassing is composed of both flammable and corrosive gas species, which is problematic when the cells power a vehicle or a portable device, as shown in Figure 1.2. This phenomenon is therefore a serious concern that limits the use of the lithium-ion technology in many fields where security is paramount.



Figure 1.2: A fire induced by the Li-ion battery of a Tesla car

The principal components of a Li-ion cell are the electrodes (anode and cathode), the electrolyte and the separator. The structure of a 18650 Li-ion cell is shown in Figure 1.3. The anode is generally composed of carbonaceous materials such as graphite. The composition of the cathode depends on the technology of Li-ion cells, but both electrodes are constructed from a polymer binder with a metallic support to allow the electrical current to pass. They can also require a conductive agent such as black carbon (BC) to enhance electric conductivity. The electrolyte is a mix of an organic solvent with a lithium salt. The solvent is typically composed of several alkyl carbonates, including ethylene carbonate (EC), propylene carbonate (PC), dimethyl carbonate (DMC) and diethyl carbonate (DEC) and the most common salt is lithium hexafluorophosphate (LiPF_6) [6]. The separator is composed of a porous material such as polyethylene (PE) and polypropylene (PP), which allows the ions to pass but inhibits electric conduction. Moreover, during the first cycles of charge/discharge, a passivation layer called the “solid electrolyte interphase” (SEI) is naturally formed on the anode surface by the products of the electrolyte decomposition. This layer is very important because it allows the lithium ions transport but blocks the electrons which could decompose the electrolyte and also prevents reactions between the anode and the electrolyte which could lead to a capacity loss [1, 3, 5].

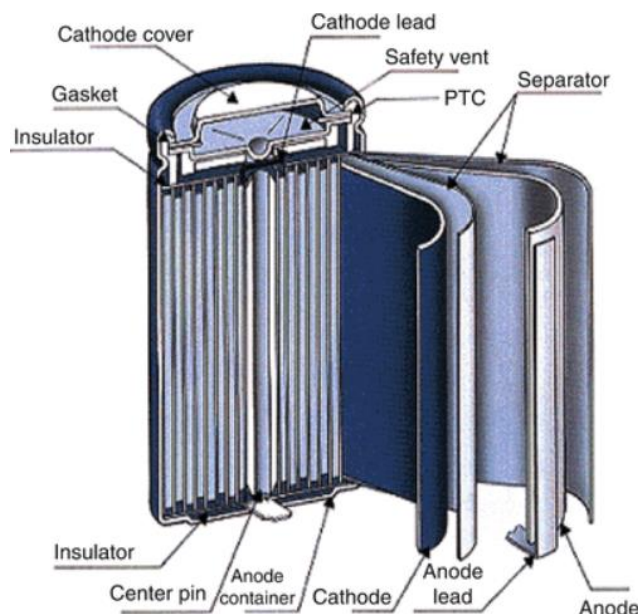


Figure 1.3: Structure of a 18650 Li-ion cell [7], reproduced with permission

Li-ion cells store electricity through the redox reactions which take place between the electrodes. Moreover, the Li-ion technology relies on solid chemical reactions known as insertion/disinsertion reactions: the lithium atoms are intercalated in the material structure of the anode and the cathode. During the charging process, Li^+ ions go from the cathode to the anode through the electrolyte while electrons go from the cathode to the anode through the external circuit. The process is inverted during the discharge. This is known as the “rocking chair” process [3, 5].

The present work is motivated by the need to increase the understanding of the thermal runaway of Li-ion cells. Such understanding is essential to properly assess risks associated with this energy storage technology, in an era when it is being deployed on a large scale in a broad range of technological fields. The focus will be towards applications in the aeronautic and aerospace industries, where the safety of the passengers is paramount. Both aircraft manufacturers and certification agencies are notoriously conservative when it comes to embracing new technologies. The electrification of air transport must therefore include an exhaustive assessment of fire risks and the development of design procedures and mitigation strategies to minimize them.

For this purpose, both experimental investigations and numerical simulation tools are needed, with the former providing data to guide the development and validate the latter. The investigation presented here will mainly follow an experimental approach, to address critical

research needs identified through an exhaustive literature review. By implementing advanced diagnostic tools to simple thermal runaway experiments mimicking the conditions of certification tests, it becomes possible to go beyond the limited pass/fail verdicts they provide and increase the fundamental understanding of the physical and chemical processes at play.

This work aims to determine the effects of both the heating rate and the ageing background on the behaviour of Li-ion cells during thermal runaway. The outgassing of the cells is also studied in an effort to identify the gas species released during this phenomenon as well as the particle size distribution. Moreover, the simple numerical combustion models developed are compared to experimental results and provide approximations of flame temperature and burnt gas composition.

In this work, tests were performed on a cone calorimeter that was modified to measure the combustion heat released during the thermal runaway of 18650 Li-ion cells, which are widely commercialized and have a cylindrical format with an 18mm diameter and a 65mm height. A cell holder was designed to heat the cells at a constant rate and to monitor their temperature during the experiments. In addition to these instruments, a mass spectrometer and two particle-size spectrometers were used to study the cells outgassing, and a multispectral camera allowed infrared measurements. The test protocol was adapted from the DO-311A standard [8] and calorimetry measurements were performed in respect of the ISO 5660-1 standard [9]. Three numerical combustion models were also implemented using the Cantera software, an open-source suite of tools that can be used in Python or MATLAB for problems involving chemical kinetics, thermodynamics, and transport processes.

This master's thesis is composed of eight chapters, including the present introduction as the first. The second chapter is a state of the art on the thermal runaway of Li-ion cells. The third chapter provides the test protocol and the instruments that were used as well as the modelling approaches. The fourth chapter is presented as a scientific article and deals with the effects of heating rate, gas emissions and particle distribution. The fifth chapter is about the effects of ageing on the thermal runaway of Li-ion cells. The sixth chapter presents the combustion models that were implemented and compares the simulations with the experimental results. The seventh chapter is a general discussion of the results. The eighth chapter presents the most significant results and discusses the impact of this work.

CHAPTER 2 LITERATURE REVIEW

2.1 The thermal runaway phenomenon

2.1.1 General description

Lithium-ion (Li-ion) batteries have become a reference for electrical energy storage because of their high energy and power density, as well as their high cell voltage [2, 3, 5, 10, 11]. These features are due to several factors specific to lithium: a relatively low density; a small ionic radius; a high electro positivity. This allows batteries with high energy density a lot smaller and lighter than other technologies such as lead-acid, Ni-Cd or Ni-MH [1].

When Li-ion cells exceed a certain heating rate, the heat produced inside the cell becomes more important than the heat that can be dissipated to the environment and this leads to a thermal runaway [2]. Heat is naturally produced inside the cell during the charge or discharge phases but can also be produced when a manufacturing defect, a mechanical damage or an abusive use induce a short-circuit. An external factor such as a fire can also provide additional heat to the cell. This phenomenon is fundamentally an uncontrolled exothermic reaction: the heat inside the cell is produced by exothermic reactions, this heat increases the temperature and therefore the reaction rates, which in turn further increases the thermal power to dissipate, and this cycle continues until the end of each reaction [3]. For Li-ion cells undergoing thermal runaway in an oxidative atmosphere, this endpoint will be the complete burning of combustible materials within the cell. This cycle is known as the heat-temperature-reaction loop [11]. Figure 2.1 illustrates this phenomenon.

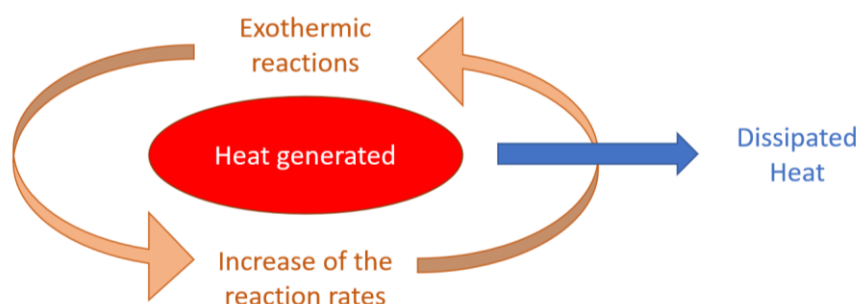


Figure 2.1: Schematic representation of the heat-temperature-reaction loop

This phenomenon is a significant obstacle to the development and increased use of Li-ion batteries because it mandates an extensive safety analysis and risk mitigation strategy in most

applications. Indeed, these batteries are often deployed into portable devices or electric vehicles (EV) [11], where thermal runaway can constitute a danger to the users. A risk multiplier is the fact that Li-ion cells are often assembled into batteries or battery packs. In these situations, the thermal runaway of a cell can propagate and generate a thermal runaway of the whole assembly, potentially leading to large scale fires [2, 12, 13]. The literature shows that the self-induce failure risk of EV is lower than the one for a conventional internal combustion engine vehicle [11], but the thermal runaway of Li-ion battery is still misunderstood so the perceived danger by users is often higher. In Table 2.1, a few examples of Li-ion battery incidents are presented. The majority occurs in the fields of transportation and portable devices and because they are often spectacular, these incidents are reported in mainstream news media.

The thermal runaway of Li-ion batteries involves other phenomena besides the visible fire. When it occurs, several gases are released. Some of these gases are flammable (CO, H₂, C₂H₄, CH₄, C₂H₆, C₃H₆, etc.) and can lead to an explosion if they are released inside a confined space [8, 14-16]. Other gases produced are toxic and corrosive (HF, HCl, NO, SO₂, etc.), representing a significant risk for people exposed to them, especially if they are trapped in a confined space [8, 17-19].

Table 2.1: Incidents on Li-ion cell batteries (adapted from [11, 20, 21])

Date	Location	Accident replay
June 2008	Columbia, US	The Li-ion battery pack of a modified Prius caught fire while driving on the highway.
May 2011	Burlington, US	A Chevy volt caught fire and destroyed adjacent cars.
May 2012	Shenzhen, China	A BYD E6 taxi caught fire after hitting a tree, killing 3 occupants.
January 2013	Boston, US	The APU battery pack caught fire and filled the cabin of a Boeing 787 Dreamliner with smoke.
January 2013	Takamatsu, Japan	The main battery pack caught fire during a Boeing 787 flight from Yamaguchi-Ube to Tokyo.
October 2013	Seattle/Tennessee, US	Two Tesla Model S ran over large metal objects at highway speed and caught fire.
April 2015	Shenzhen, China	Wuzhou Dragon EV bus caught fire during charging in a garage.
September 2015	Hangzhou, China	The battery pack of an HEV bus caught fire.
January 2016	Gjerstad, Norway	A Tesla model S caught fire while fast charging at a Supercharger station.
April 2016	Shenzhen, China	A Wuzhou Dragon EV bus caught fire.
June 2016	Beijing, China	An iEV5 caught fire before the landmark of Sanlitun.
July 2016	Nanjing, China	The battery pack of an EV bus caught fire after heavy rain.
July 2016	Rome, Italy	An EV police car caught fire in the street.
March 2018	Salt Lake City, US	A lithium battery caught fire in a passenger suitcase loaded in the cargo hold of an aircraft.
February 2020	Florida, US	A passenger's backup power source caught fire in an Airbus 320 flight.

2.1.2 Causes and successive steps for thermal runaway

The thermal runaway phenomenon is explained here by detailing the different processes that occurs inside the cell. Li-ion cells are a complex assembling of solid and liquid components. Hence, it is complicated to understand the sequence of reactions that occur during the thermal runaway, but several studies have shed light on the phenomenon. Different pre-failure processes are shown in Table 2.2.

Table 2.2: Pre-failure processes and their description [3, 11, 16, 22]

Pre-failure process	Description
Heating	If enough heat is produced in the environment (by a fire close to the cell for example), it will prevent the cell from cooling down normally. In this situation, the cell will heat up and reach thermal runaway.
Internal or external short-circuit	A defect inside the cell can lead to a short-circuit, producing heat that can trigger the thermal runaway. A defect in the wiring outside the cell can also produce large amount of heat.
Deformation	If the cell undergoes a mechanical damage like an impact or a perforation, it can induce an internal short-circuit.
Overcharge or overdischarge	When a cell is charged or discharged, heat is produced inside the cell. If the current becomes too important, the heat generated can be enough to trigger thermal runaway.

Detailed investigations of the failure modes found in the literature reveal that the four mechanisms above may not be the unique triggers for thermal runaway. Indeed, a phenomenon of chemical crossover between the cathode and the anode is also suspected to generate enough heat to start the thermal runaway [23]. Specifically, the oxygen released by the cathode can react with the anode to create a sharp heat generation enhancement that could be the trigger of thermal runaway. However, this phenomenon is not sufficiently studied to be considered by consensus a trigger for TR onset.

The thermal runaway can be divided into different phases. First, the battery begins to generate heat at a slow rate. In this phase, a small venting event of gases produced within the cell can occur, but the cell is still not in an irreversible runaway state. Second, if this heat generation continues until the cell reaches a critical temperature, thermal runaway is triggered (between 150°C and 300°C, depending on the technology of the cell). The events leading to catastrophic failure can last a few seconds to several minutes depending on the pre-failure process. When this threshold is reached, a rapid increase of temperature is observed, and a very large quantity of gas is released through a major venting event. The temperature can reach approximately 1000°C and a production of sparks can also be observed. The risk of fire or explosion is very important due to the production of flammable gases and high temperatures. This third phase lasts a few seconds, then the cell slowly cools down or the solid and liquid remnants of the cell begin to burn if an oxidizer is present [5, 24].

Li *et al.* presented an interesting interpretation of the thermal runaway of Li-ion cells, by comparing the phenomenon with the combustion process occurring in internal combustion engines [25], showing similarities between the two phenomena. In an internal combustion engine, a cycle can be divided in four steps: intake, compression, combustion, and exhaust. In the same way, Li-ion cell failure can be seen like a unique cycle with four steps: assembly of the cell, abuse, thermal runaway, eruption of the gases.

The sequence of major events internal to the cell occurring during thermal runaway can be described as follows [3, 11]. First, the exothermic reaction begins with the SEI layer breakdown. This reaction occurs at a relatively low temperature (between 100°C and 150°C). In this step, the temperature increases slowly and there is no visual manifestation of the reaction. When the temperature reaches approximately 150°C, the intercalate lithium in the anode begins to react with the organic solvent of the electrolyte. This reaction leads to the SEI regeneration and the production of light hydrocarbons, perhaps presenting an explanation for the small venting event. This continues until the temperature is high enough for the separator to melt. The separator is commonly composed of polyethylene (PE) and polypropylene (PP), that melt respectively at approximately 130°C and 160°C. This reaction is endothermic and produces a short slowdown in the temperature increase [11]. The melting of the separator leads to an internal short-circuit between the two electrodes and this produces more heat. When the temperature is high enough (between 150°C and 300°C depending on the cathode composition), the cathode breaks down, which releases gases including oxygen and produces a large amount of heat. In addition to reactions within the anode, the electrolyte decomposition produces flammable and toxic gases. When the pressure exceeds the threshold of the security vent, a major venting event occurs and releases the produced gases into the atmosphere. Then, these gases can ignite, providing a strong heat feedback to the cell, which can then reach very high temperatures.

Other reactions are also reported in the literature. The binder can react with the electrodes and produces additional heat. When the SEI layer decomposes, it can also lead to a reaction between the carbon/graphite in the anode and the electrolyte [3].

In Figure 2.2, the heat generated by each reaction is presented qualitatively [11, 26], revealing that these different reactions can occur simultaneously, and yield the heat-temperature-reaction loop that was mentioned previously. In addition to these reactions, that all occurs in the solid phase of the cell, the internal short-circuit releases the electrical energy stored in the cell and

the combustion of the gases emitted both release additional heat, respectively within and close to the cell undergoing thermal runaway.

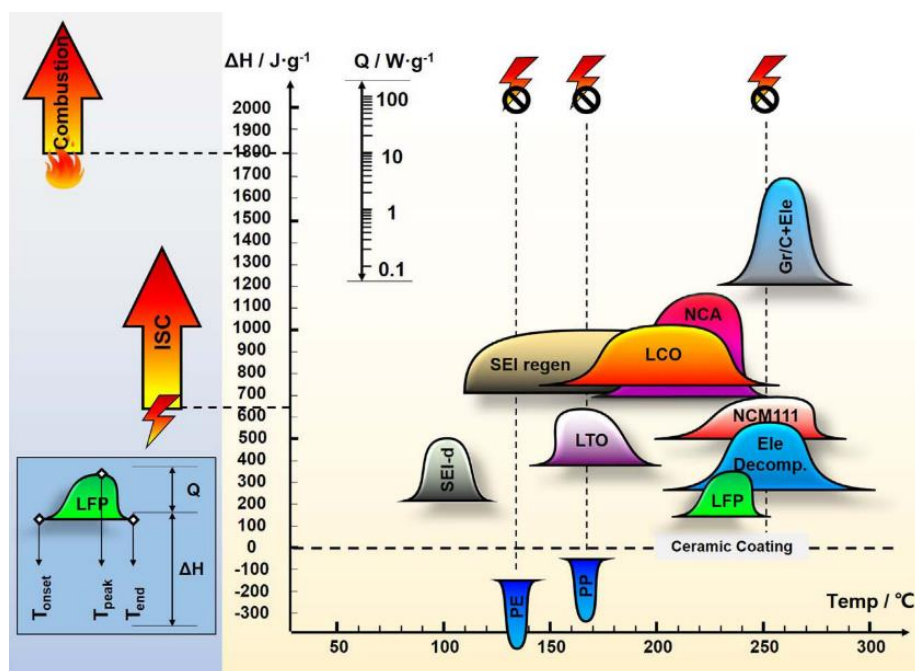


Figure 2.2: Heat generated by the different reactions and temperature of reaction (abbreviations in Table 2.3) [11], reproduced with permission

Table 2.3: Abbreviations used in Figure 2.2 [11]

Abbreviation	Description
ISC	Internal short-circuit
T_{onset}	The onset temperature of reaction
T_{peak}	The peak temperature of the reaction
T_{end}	The terminal temperature of the reaction
Q	The maximum heat generation power
ΔH	The enthalpy of the total energy released during reaction
SEI-d	The decomposition of SEI
SEI regen	The decomposition and regeneration of SEI
PE	The melting of the PE separator or PE base
PP	The melting of the PP separator or PP base
LTO	The decomposition of the $\text{Li}_4\text{Ti}_5\text{O}_{12}$ (LTO) anode with electrolyte
LCO	The decomposition of the LCO cathode with electrolyte
NCA	The decomposition of the NCA cathode with electrolyte
NCM111	The decomposition of the NCM111 cathode with electrolyte
Ele. Decomp.	The decomposition of the electrolyte
Gr/C+Ele	The decomposition of the graphite/carbon anode with the electrolyte

2.1.3 Gas production during thermal runaway

During the thermal runaway, a cell releases several different gases. A large proportion of the total released gases is made up of CO₂ and CO. Hydrocarbons and flammable species such as C₂H₄, CH₄, C₂H₆, C₃H₆ and hydrogen H₂ are also generated [15, 16, 27], as well as very toxic and corrosive gases, including HF, HCl, NO or SO₂ [17, 18, 28, 29]. Moreover, a small quantity of O₂ is produced by the cathode decomposition [3], contributing to the risk of fire.

The literature provides information on the source of these gases [3, 15, 17, 24, 27, 28, 30] but there are significant uncertainties. Indeed, although the detection of the different gases is based on precise analytical chemistry instrumentation, the detection of their source is more complex. Moreover, gas release often occurs through discrete short-lived events, and as a result the quantification of the cell outgassing in terms of composition and volume is often uncertain, with its origins somewhat speculative. To be more precise, certain studies focused on a single component of the Li-ion cell, for instance the combustion of the electrolyte. Nevertheless, different parts and different phases can react together during thermal runaway and lead to the production of other gases.

The current understanding of the origins of the different species emitted is as follows. HF, HCl, NO or SO₂ may come from the decomposition of the additives or the lithium salt in the electrolyte. HCl may also come from the binder, the separator, and the packaging of the cell. A possible source for H₂ is the reaction between the binder and the intercalated lithium. CH₄ may be produced by the reduction of the electrolyte. C₂H₄ and C₂H₆ may come from reactions between the components of the electrolyte with the anode. CO₂ can be generated by the decomposition of the different components of the cell or by the combustion which can take place during the thermal runaway. CO may come from the reduction of CO₂ on the anode, from the decomposition of the cathode or from the reaction of carbonaceous material with the O₂ released by the cathode. CO may also come from the incomplete combustion of other gaseous species. Literature shows that during the thermal runaway, CO is first produced inside the cell where there is an oxygen-lean atmosphere and then, CO₂ is produced when the combustion takes place outside the cell in the oxygen-rich atmosphere [29].

The quantity of oxygen generated by the decomposition of the cathode is generally not sufficient to permit combustion within the cells or in an inert atmosphere. Generally, the combustion takes place outside the cell with the oxygen supplied by the atmosphere. The

ignition source for the combustion can be an electric arc created by the short-circuit inside the battery or sparks generated by the friction of the high-speed gases released through the vent valve [11].

The electrolyte appears to be the source of a large quantity of several combustible gases, a problem difficult to avoid since electrolytes are often liquid hydrocarbons and this component of the cell plays a major role in its normal operation. Solid-state electrolytes are a promising solution to overcome the fire risk induced by the use of a liquid hydrocarbon electrolyte but this technology is under development and its performance is still lower than that of liquid-state electrolytes [31].

2.1.4 Safety approaches implemented in Li-ion cells

Several features integrated in Li-ion cells conception reduce the risk of thermal runaway. A lot of work has been done on the choice of materials used in the cells. For example, the use of materials resistant to high temperature in the separator delays the risk of internal short-circuit to higher temperatures [2]. Additives in the electrolyte can also increase its thermal stability and enhance the security of Li-ion cells [5]. Other approaches integrated into the cell conception to prevent major security events are detailed in the following paragraphs.

The “current interruption device” (CID) allows switching off the current in the cell if the internal temperature becomes too high [5] or if there is an overcharge during cell use [32]. When a CID is integrated into a cell conception, the cell contains additives which generate gas pressure before thermal runaway is irreversibly started [32]. The CID is then triggered by the internal pressure of the cell, with a threshold typically at approximately 7 bars [22]. This device irreversibly disables the cell. The “positive temperature coefficient” (PTC) approach allows the current to be limited if the temperature becomes too high [5, 32]. This reversible protection device is composed of a ring of metal laminated into a polymer located in the positive cell terminal. When the temperature rises, the electrical resistance of this device increases sharply, thus limiting the current but generating heat [32]. The “security vent” aims to avoid cell explosion by releasing the gases produced inside the cell [5, 18, 22]. It is basically a security valve which opens when the internal pressure exceeds a threshold value of several tens of bars [5].

Figure 2.3 illustrates the different security components mentioned previously.

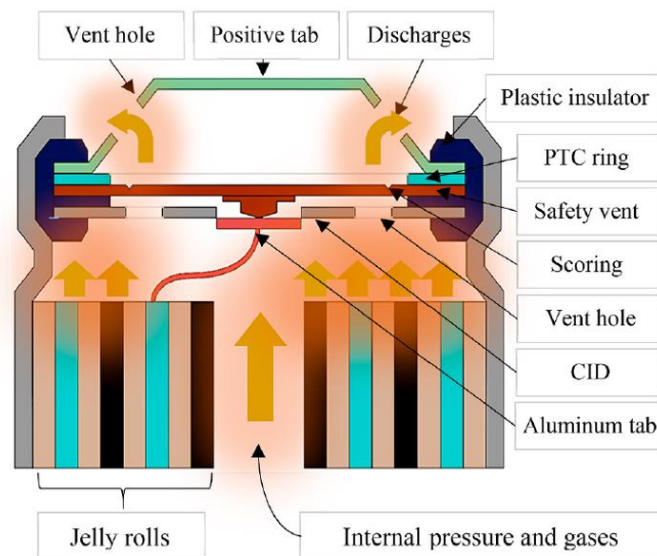


Figure 2.3: Cross-section of a typical 18650 Li-ion cell showing the PTC and the CID [33], reproduced with permission

It is important to note that all these security devices only work up to a certain extent. When the conditions become too abusive, for instance if there is an external fire or heat source, these systems cannot stop thermal runaway.

2.1.5 The ageing phenomenon

The ageing phenomenon of Li-ion cells can be decomposed in two parts. There are “calendar” and “cyclic” effects. The calendar effects represent the conditions that develop even if the cell is not used: they depend on the cell state of charge and the conditions of the environment in which it is stored. These effects are important because they build up over a significant part of the life of a Li-ion cell. Cyclic effects occur because of the charge/discharge cycles of the cell. Several factors must be considered: the number of cycles, the current of charge/discharge, the maximum state of charge and the minimum state of discharge, the temperature of the environment where the charge/discharge takes place, etc [5]. Therefore, it is important to have an exhaustive background of the Li-ion cells use history to assess its thermal runaway behaviour, as discussed in the following section.

Ageing leads to an increase of the cell electrical resistance, higher energy loss during charging and discharging and a decrease power for the cell [34]. This is due to several of complex mechanisms which take place in the cell chemistry. The major ones are the loss of cyclable lithium ions in the electrolyte and the deterioration of the electrodes [5]. On the negative

electrode, an increase in the SEI thickness can be observed due to the electrolyte decomposition and the loss of active material [2]. For low temperature cycling, a deposition of solid lithium (Li plating) on the anode was also highlighted [35]. On the positive electrode, structural damages can be noticed due to the insertion/disinsertion of lithium, as well as the formation of a film on the electrode surface because of electrolyte decomposition and a loss of active material [2, 36].

2.2 Certification standards

This section reviews certification standards that are applied for Li-ion cells and battery systems used in the industry. These standards provide performance and safety requirements and are particularly important in the aerospace sector. Indeed, governments impose testing prior to product certification, with the DO-311A standard a major reference for Li-ion cells and batteries.

2.2.1 The DO-311A standard

The DO-311A standard is provided by the Radio Technical Commission for Aeronautics (RTCA), a non-profit organization based in the United States. This organization sets up technical guidelines which are used by the government regulatory authorities and the industry [37]. The DO-311A is an international standard for rechargeable lithium batteries and battery systems. It establishes testing methods for the verification and characterization of the safety and performances of the batteries. These tests are carried out by battery manufacturers, aircraft manufacturers and end users within the aviation community. It applies for rechargeable batteries which are included in the design of the aircraft [8].

Two different requirements are tested in this standard [8]. First, the performance requirements test allows the verification of the battery performance. During this test phase, in addition to the nominal operating conditions, all the protection systems integrated in the battery are tested by submitting them to abusive conditions (overcharge, overdischarge, short-circuit, etc.). Second, the battery is submitted to abusive conditions with all the protection systems removed during the security requirements test. The security requirements test is the section of interest in the present work. All the procedures are described in Table 2.4.

Table 2.4: Procedures from the DO-311A standard

	Procedure	Verification
Performance requirements	Physical examination	Mass, dimensions, marking, manufacturer's workmanship standards
	Acceptance test	Functionality in nominal condition
	Insulation resistance	Insulation resistance between the poles
	Handle strength	Handles of the battery
	Rated capacity	Rated capacity shall comply the design documentation
	Capacity at low and high temperatures	Capacity shall comply the design documentation
	Constant voltage discharge	Current of discharge for a constant voltage discharge
	Charge acceptance	Chargeability
	Charge retention	Storage of energy during a given time
	Cycling	Cyclability
	Rapid discharge at high temperature	Battery must operate in these conditions
	Short-circuit protection	Functionality of the protection
	Overdischarge protection	Functionality of the protection
	Overcharge protection	Functionality of the protection
Safety requirements	Short-circuit	Material ejection, flame and gas emission
	Overdischarge	Material ejection, flame and gas emission
	Single cell thermal runaway containment	Material ejection, flame and gas emission
	Battery thermal runaway containment	Material ejection, flame and gas emission
	Explosion containment	Material ejection, flame and gas emission
	Drop impact containment	Material ejection, flame and gas, smoke, soot or liquid emissions

During the security requirements tests, the macroscopic behaviour of the battery is observed qualitatively. Thus, they are binary tests: either the battery passes the test, or the battery fails. For example, at the end of the “single cell thermal runaway containment”, the battery system shall have contained the different fragments and the possible flames, and the gas emission shall comply with the battery manufacturer declarations about venting [8].

It is important to note that this standard does not apply to an individual lithium cell but to a battery. Nevertheless, a method to trigger the thermal runaway of a single cell via overheating (“Test method for single cell thermal runaway via overheating”) is described. In this test, the overheated cell is part of a battery assembly, but the method can be adapted to study the thermal runaway of a single cell [8].

Several aircraft and battery manufacturers have expressed concerns about the DO-311A standard. Among these manufacturers, Boeing, Airbus and Saft wrote a letter to explain their thought. Their disagreement mostly concerns the single cell thermal runaway containment and the battery thermal runaway containment [8].

In their opinion, the thermal runaway containment test is too far from the reality. The test is done without any protection in the standard, but this situation never happens in a real situation because the protection systems are integrated in the design of the battery pack. The DO-311A standard also describes two different ways to trigger the thermal runaway, either by overcharge or by overheating. According to the manufacturers, these two situations can hardly happen in reality where the thermal runaway is most often triggered by a defect in the battery or in the cell conception. Moreover, the overcharge leads to an excess of energy and the overheating affects the structure of the battery in addition to the cells, therefore these two situations can affect the results of the test. In the “battery thermal runaway containment” test, the thermal runaway occurs in all the cells at the same time because the whole battery is heated but in a real situation, the propagation phenomenon between the cells plays a major role. Overall, the manufacturers think that the DO-311A standard does not contribute to improving the battery design and they suggest that the test should rely on the most plausible scenario for the trigger of the thermal runaway [8].

In response, the members of RTCA acknowledge that the test is far from the reality, but they think that this is a good way to observe the behaviour of the battery in extreme but consistent and easy to implement conditions. They also mention that this standard is intended to validate the use of a battery for aeronautic applications and that it does not replace the research work required to improve the design of the batteries. They add that other standards for research and design improvement exist and are complementary to this one [8].

2.2.2 Other standards

There are other organizations which provide certification standards or guidelines for lithium-ion batteries: The American National Standards Institute (ANSI), the United Nations (UN), the Underwriters laboratories (UL), the International Electrotechnical Commission (IEC), the Institute of Electrical and Electronics Engineers (IEEE), the Society of Automotive Engineers (SAE), the Japanese Industrial Standards (JIS), the European Union (EU), etc. Each one of these organizations focuses on particular aspects of the Li-ion safety problem (transport, conception, safety, etc.) [38, 39]. The safety consideration evaluated by these standards are summarized in Table 2.5.

The United Nations (UN) and the United States Department of Transportation (DOT) established the UN/DOT 38.3 standard. It concerns any lithium-ion or lithium metal batteries or cells that must be shipped [38, 40, 41]. This standard is composed of eight tests: altitude simulation (low-pressure test), thermal test, vibration, shock, external short-circuit, impact, overcharge and forced discharge [40]. In particular, the thermal test consists of exposing the battery to changes in temperature between $-40\text{ }^{\circ}\text{C}$ and $+75\text{ }^{\circ}\text{C}$. The battery is submitted to 10 cycles of 6 hours of storage at $-40\text{ }^{\circ}\text{C}$ and 6 hours of storage at $+75\text{ }^{\circ}\text{C}$ [40]. If a battery does not meet the requirements of this standard, its shipment will be restricted.

The Underwriters Laboratories (UL) is an independent product safety certification organization. Concerning lithium cells, they wrote the UL 1642 standard [38]. The standard is composed of several tests: external short-circuit, overcharge, overdischarge, crush, impact, shock, vibration, heating, temperature cycling, low pressure, drop and molded casing heating test [42]. The International Electrotechnical Commission (IEC) is a non-profits organization specialized in international standards for electrical and electronic technologies. IEC wrote three different standards for rechargeable lithium batteries: IEC 61960, IEC 62133 and IEC 62281 [38]. The IEC 62281 is similar to the UN/DOT 38.3. The IEC 62133 is very well known in the electric battery field and is the reference safety standard for applications in portable devices. The IEC 62960 is more specialized towards lithium batteries and cells [43]. The Institute of Electrical and Electronics Engineers (IEEE) is an international non-profits organization which develops standards for the industry [38]. There are two IEEE safety standards for rechargeable Li-ion batteries used in portable devices: IEEE 1625 and IEEE 1725. These two standards are more guidelines for conception than a description of safety tests. IEEE 1625 is for Li-ion batteries used in computing devices and IEEE 1725 is for the ones used in cellular phones [44, 45]. The

Society of Automotive Engineers (SAE) is a professional organization for the automotive industry [38]. SAE wrote two standards, SAE J 2929 and SAE J 2464, which are used for the batteries in electric vehicles.

Table 2.5: Criteria tested in the different standards

Criteria	DO-311A	UN/DOT 38.3	UL 1642	IEC 62133	IEC 62281	IEEE 1625	IEEE 1725	SAE J 2929	DO-160G
External short circuit	•	•	•	•	•	•	•	•	
Overcharge	•	•	•	•	•	•	•	•	
Overdischarge	•	•	•	•	•			•	
Crush			•	•	•			•	
Impact	•	•	•		•				•
Shock		•	•	•	•			•	•
Vibration		•	•	•	•			•	•
Heating	•	•	•	•		•	•		•
Temperature cycling		•	•	•	•			•	•
Low pressure		•	•	•	•				•
External fire	•		•			•	•	•	•
Drop	•			•		•	•	•	
Molded casing heating test				•					
Isolation resistance	•			•				•	
Internal short circuit				•					

The European Council for Automotive Research and Development (EUCAR) have created a scale for hazard levels concerning the Li-ion batteries. There are eight hazard levels that can be seen in Table 2.6: the higher the level is, the more critical is the situation [46, 47]. This scale is used in the automotive sector and aims to precisely define the expectations for Li-ion cells safety in the certification tests. Contrary to the DO-311A where the verdict of the tests is pass/fail, this approach allows a ranking of the hazards observed in tests.

Table 2.6: EUCAR hazard levels and descriptions [47]

Hazard Level	Description	Classification Criteria and Effect
0	No Effect	No effect. No loss of functionality.
1	Passive protection activated	No defect; no leakage; no venting, fire, or flame; no rupture; no explosion; no exothermic reaction or thermal runaway. Cell reversibly damaged. Repair of protection devices needed.
2	Defect/damage	No leakage; no venting, fire, or flame; no rupture; no explosion; no exothermic reaction or thermal runaway. Cell irreversibly damaged. Repair needed.
3	Leakage $\Delta_{\text{mass}} < 50\%$	No venting, fire, or flame; no rupture; no explosion. Weight loss $< 50\%$ of electrolyte weight (electrolyte = solvent + salt).
4	Leakage $\Delta_{\text{mass}} \geq 50\%$	No fire or flame; no rupture; no explosion. Weight loss $\geq 50\%$ of electrolyte weight (electrolyte = solvent + salt).
5	Fire or flame	No rupture; no explosion (i.e. no flying parts).
6	Rupture	No explosion but flying parts of the active mass.
7	Explosion	Explosion (i.e. disintegration of the cell).

2.3 State of the art on the thermal runaway of Li-ion cells

2.3.1 Experimental studies

This section provides a state of the art of the experimental investigations focused on the thermal runaway of Li-ion cells. The first part presents the facilities required for fire-calorimetry studies. The second part is focused on the key results obtained by fire-calorimetry methods. The last part outlines complementary results from other calorimetry studies and shows the influence of the ageing effect on the thermal stability of Li-ion cells.

2.3.1.1 The experimental setup for combustion studies

Combustion tests are commonly conducted in a cone calorimeter. This instrument is designed to evaluate the fire resistance of combustible materials by measuring the heat release rate (HRR) following exposure of samples to an external heat source. The standard ISO 5660-1 calorimeter [9] can be slightly modified to evaluate the heat released as a battery undergoes thermal runaway and combustion. The basic operations principle is usually the following: the heat released during the combustion is calculated based on the amount of oxygen that reacts. An example of cone calorimeter is presented schematically in Figure 2.4.

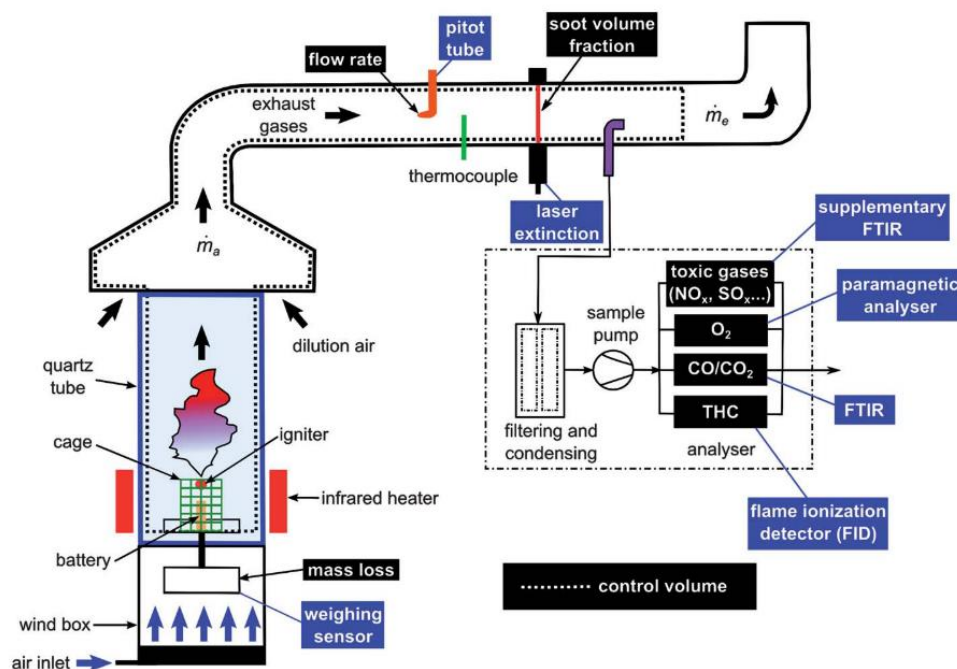


Figure 2.4: A cone calorimeter used for combustion analysis [30], reproduced with permission

First, the temperature of the sample is increased by a heating device, for instance a gas burner or an infrared heater. The advantage of an infrared heater is that it does not interfere with the combustion of the sample, as there is no additional fuel provided. A continuous flow of air is supplied below the sample holder and the weight of the sample is measured during the entire test to determine the mass loss rate. An igniter, usually a spark generator, is placed over the sample and ignites the gas released by the pyrolysis of the heated sample. The combustion gases are then diluted with air, collected by an exhaust hood, and analysed by different methods. This approach typically yields a simultaneous measure of the temperature of the combustion gases, the partial composition of the exhaust gases and the heat released rate (HRR) of the burning sample [17, 30, 48, 49].

The HRR is the rate at which a fire releases thermal energy, it is the power of the combustion, and it can be expressed in watts (W). There are different ways to measure the HRR. It can be determined by oxygen consumption, by mass loss or by the analysis of the production rates of CO₂, CO and soot [28]. Oxygen consumption is the most commonly used method and is based on the approximately constant heat released per unit of oxygen consumed for most hydrocarbons. This approach has many advantages. On the one hand, it is relatively easy to implement because the only values needed are the flow rate and the oxygen concentration in the exhaust pipe. On the other hand, the composition of the fuel is also not needed. The main

limitation of this method for lithium cell calorimetry is that it does not take account of oxygen produced by the cathode during thermal runaway. Nevertheless, literature shows that the oxygen produced by the cathode contributes for less than 13 % of the total energy released during the thermal runaway of a fully charged Li-ion cell [48]. This value was found by comparing the HRR obtained by the mass loss rate method with that obtained by oxygen depletion on LCO Li-ion cells. However, the literature also mentions that the very short duration of the thermal runaway distorts the results obtained by oxygen consumption and that correction algorithms exist to resolve this issue [50]. Conversely, the advantage of using the mass loss rate or the production of CO, CO₂ and soot for the analysis of Li-ion cell combustion is that these methods are not influenced by the oxygen that can be produced by the cathode during the thermal runaway.

The detailed testing method for combustion studies using a cone calorimeter is described in the ISO 5660-1 standard. This standard aims to measure the HRR and the dynamic smoke production rate of samples exposed to controlled irradiance with an external igniter [9]. In this method, the sample is heated continuously, without stopping when exothermic reactions become significant.

Different diagnostic tools can be used to analyse the gas composition [30, 48, 49, 51, 52] The oxygen analyser allows the measurement of the amount of oxygen in the combustion gases. For combustion studies in general, since the proportion of oxygen in the input is known, the HRR can be calculated from the oxygen consumption. Several types of oxygen sensors exist, the most common uses the paramagnetic sensibility of the oxygen molecule. The non-dispersive infrared (NDIR) analyser is used for the measurement of the concentration of CO and CO₂. It uses the principle of infrared absorbance of these two gases. The Fourier-transform infrared (FTIR) analyser allows the determination of the detailed composition of the combustion products and gives the concentration of each different gas. It uses the absorbance profile of a gas sample in the infrared spectrum to determine its composition. The flame ionization detector measures the total hydrocarbon content (THC) of the product of combustion. It is based on the detection of ions in the products of combustion. The gas chromatographer - mass spectrometer (GC-MS) allows a precise measurement of the composition of a gas. It works by the measurement of the mass-to-charge ratio of the ions created by ionization of the combustion product.

2.3.1.2 Key results from fire-calorimetry studies

This section reviews the results of several studies that were conducted to characterize the combustion of the outgassing during the thermal runaway of Li-ion cells. In particular, the literature reveals the effects of the state of charge (SOC) on the heat release rate (HRR) and the gas composition. In these experiments, the gas mixture released during the thermal runaway of a Li-ion cell or battery is intentionally ignited with air to obtain information on its heat of combustion, which can constitute a major heat feedback mechanism to the adjacent cells and therefore multiply the fire hazard.

The state of charge of the Li-ion cell has a large impact on the thermal runaway. This is due to the quantity of energy stored inside the cell and to the chemical composition of the electrodes (the intercalated lithium moves from the cathode to the anode during the charge). The literature shows that when the SOC increases, the time to thermal runaway is reduced [30, 48], the HRR peak magnitude increases [17, 30, 48, 49, 53] and the maximal temperature increases [30, 48, 50]. Therefore, a fully charged cell is significantly more dangerous than a discharged cell. Moreover, due to the possible combustion of its solid components and of the gases released, a Li-ion cell thermal runaway can generate significantly more thermal energy than what is stored in the form of chemical energy during the charge.

Figure 2.5 shows a typical profile for the cell temperature and HRR measurements for different SOC during a combustion test on 18650 LCO Li-ion cells [48]. The profile of temperature was obtained for a fully charged cell and all measurements were realized in a cone calorimeter with the same incident heat flux of 50 kW/m². It appears that there are two peaks of HRR during the Li-ion cell failure. The first peak rises to 1 kW or 1.5 kW for a few seconds and occurs when the burst disk cracks and liberates a small quantity of gases. This event does not seem to be affected by the SOC. The second peak reaches between 5.8 kW and 6.8 kW for cells within a high SOC (65 % to 100 %). For cells with a lower SOC (0 % to 50 %), the HRR in this second peak corresponding to the thermal runaway itself is much lower (1.1 kW to 1.5 kW). It therefore appears that the SOC has a strong influence on the magnitude and the timing of this second HRR peak. The higher the SOC is, the more dangerous is the thermal runaway. It is also interesting to note that these Li-ion cells did not explode with less than 50 % SOC and that 0 % SOC is the safest case with the lowest HRR. Moreover, the SOC has also an influence on the timing of the second HRR peak, the latter occurring sooner when the SOC increases.

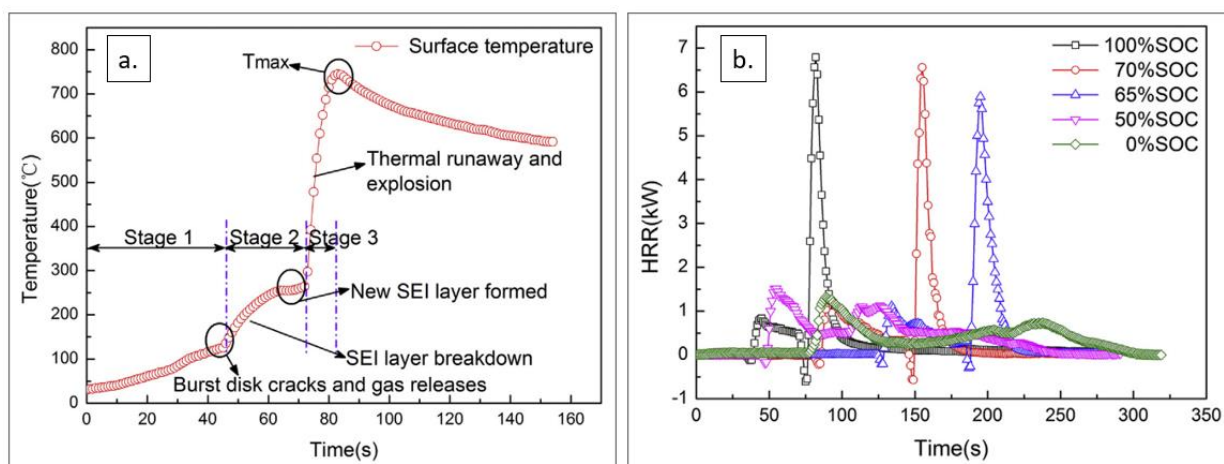


Figure 2.5: Classic profiles of cell temperature (a) and HRR (b) for different SOC during the thermal runaway of 18650 LMO Li-ion cells [48], reproduced with permission

In contrast to the increase of the HRR peak, the total energy released becomes less important when the cell is charged. Indeed, by integrating the HRR curves over time, total energy released is 100 kJ, 101 kJ, 104 kJ, 120 kJ and 109 kJ for 100 %, 70 %, 65 %, 50 % and 0 %, respectively. This counter-intuitive observation can be an artefact of the testing method used, as the thermal runaway of a fully charged cell happens very quickly, possibly resulting in a restriction of oxygen and an incomplete combustion [30, 53].

The total amount of released gas (or the mass loss of the cell) is not affected by the SOC and follows the behaviour expected for the combustion of the different hydrocarbons inside the battery [30, 51]. However, the composition of the released gases is affected. CO and CO₂ increase with the SOC, but hydrogen fluoride (HF) follows an opposite trend. HF is a very corrosive gas that can accumulate into confined areas and react with water to form hydrofluoric acid, a highly corrosive and toxic compound. SO₂ does not follow a clearly identifiable trend and may depend on the composition of the electrolyte salts, because results differ significantly between studies [17, 30, 54]. The literature also reveals that the majority of the toxic gases (HF, SO₂, NO, HCl, etc.) are the result of the combustions of the solvent and salts inside the electrolyte [17, 28]. A study on the degradation of the electrolyte showed that the majority of the gases came from the thermal degradation of the electrolyte with major components being ethylene carbonate (EC) and dimethyl carbonate (DMC) [52]. The study also reveals that a minority of gases (ethyl methyl carbonate (EMC), diethyl carbonate (DEC), CH₃CH₂F, C₂H₄ and C₂H₆) were only detected for cycled cells. This suggests that they may arise from compounds formed during cycling electrochemical reaction [52].

The overall combustion efficiency can be quantitatively estimated from the results of Ribière *et al.* [30]. It appears that the total amount of gas produced increases with SOC for CO but decreases for CO₂. Therefore, the combustion is less efficient when the SOC increases, perhaps as discussed above from the lack of sufficient O₂ in high SOC combustion experiments where gas release is very violent. This is also revealed by the amount of THC measured, revealing that the proportion of the fuel that has not burnt completely increases when the SOC increases. This study also provides production trends for corrosive and toxic gases. Nitrogen oxide (NO) peak production rate increases when the SOC increases but its production time is shortened. Sulphur oxide (SO₂) is found in higher concentration when the SOC increases. The total quantity of hydrochloric acid is not affected by the SOC but differences in the kinetics of its production appear. For hydrogen fluoride (HF) both the quantity and the production kinetics are affected by the SOC. When the SOC increases, although the production peak magnitude increases, the total quantity of HF and the production time decrease.

2.3.1.3 Effect of cell ageing

The influence of ageing phenomenon on the thermal stability of Li-ion cells is less obvious than the influence of the SOC. An analysis of the literature reveals that the main factors that influence the thermal stability of an aged cell are the SEI layer thickening and the Li plating on the anode surface [55, 56]. This is because more material can be exothermically decomposed with a thick SEI layer and because the Li plating results in an increase of the global impedance of the cell. The thermal stability of an aged cathode remains nearly the same as a fresh one whereas the reaction between an aged anode and the electrolyte seems more severe than with a fresh one [55, 56].

The correlation between the calendar ageing and the thermal stability of a Li-ion cell is weak. In their study, Röder *et al.* have tested 18650 Li-ion cells with LiMn₂O₄ (LMO) as cathode material after a storage at 60 °C for 36 weeks (100 % SOC) [56]. It appears that the heating rate of the aged cells follows the same pattern as that of new cells. The initial temperatures of TR were included between 100 °C and 120 °C and the maximum heating rate was slightly inferior for the aged cell. D. Ren *et al.* have studied a Li_x(NiCoMn)_{1/3}O₂ (NMC) pouch Li-ion cells which were stored at 55 °C for 200 days (100 % SOC) [55]. They found that in comparison to a fresh cell, the calendar ageing had improved the resistance against TR by increasing of the initial temperature of TR and by decreasing the heating rate in the early stage of TR.

Cyclic ageing deteriorates the thermal stability of Li-ion cells. Larsson *et al.* tested prismatic Li-ion cells and did not find a clear correlation between the number of cycles and the thermal runaway performances [34]. Their results reveal that thermal runaway is triggered at lower temperature and the weight loss is more important when the cell went through a few hundred cycles. This study revealed that the most critical scenario in terms of cell temperature and weight loss appears to be after approximately 160 cycles for the type of cell they studied. Whether this trend represents a general behaviour of cycled cells is questionable considering the limited number of data points in the study. Wu *et al.* studied the cyclic ageing effects during thermal runaway for 18650-type Li_xCoO_2 (LCO) cells in an oven test [57]. The cells were cycled at 45 °C. The thermal runaway appears earlier in the aged cells. Moreover, the cells subjected to 400 cycles experienced an explosion instead of the typical venting episode. This observation is surprising as an aged cell has less electrical energy storage capacity than a fresh one. The authors advance the hypothesis that this explosion is caused by the decay of a safety mechanism strength. Fleischhammer *et al.* tested 18650-type $\text{Li}_x(\text{NiCoMn})_{1/3}\text{O}_2$ (NMC) cells under different ageing conditions [35]. They compared unaged cells, high-rate cycled cells (charge rate of 4.33 C and discharged rate of 16 C) and low temperature (-10 °C) cycled cells. The cells were cycled until their capacity dropped below 80 %. Their results show that both the high rate cycled cells and the low temperature cycled cells have lower thermal runaway onset temperature. The worst performing cells are those cycled at low temperature, with self-heating starting at temperatures between 30 °C and 53 °C.

2.3.2 Solid phases modelling

A complete simulation of the thermal runaway of Li-ion cells combining detailed chemical reactions in the solid phases, combustion reactions in the gas phase and thermal/mass transfers between the two phases does not exist yet. The modelling of solid phase reaction in a Li-ion cell alone is complicated by several difficulties. First, the composition of the cells is heterogeneous and not always known precisely. Second, the chemical mechanism for the reactions occurring in each solid constituent of the cell is also not known. Finally, transport limited reactions occur in each and between solid phases, which are difficult to model and require precise values of transport properties [6]. Nevertheless, several attempts to model at least partially solid-phase reactions in a Li-ion cell undergoing thermal runaway can be found in the literature.

Several approaches can be found in the literature to model the chemical mechanisms of the solid phases of a Li-ion battery. The amount and the composition of the vented gases as well as the effective heat of combustion can be calculated by taking the composition of the solid phases inside the cell into account [17, 28, 30, 58]. Golubkov *et al.* measured the composition of the solid phases and the composition of the vented gas for NCA and LFP cells. By listing the chemical reactions taking place in the cell, they succeeded in calculating “utilization numbers” that defined how often each of the reactions was applied [58]. This experiment was conducted for discharged and fully charged cells. The “utilization numbers” were determined by a linear algorithm and give a possible set of chemical equations that describe the reactions inside the cell during the thermal runaway. Nevertheless, an important part of the gases was not detected by the gas chromatography system and the modelling was not used to predict the quantities of gases but rather to retrieve the measured ones. Therefore, this type of modelling cannot be used to predict the thermal runaway behaviour under different conditions unless experimental data for the gases emitted is also available in these conditions.

In his paper, K. Leung describes in detail the initial stages of the ethylene carbonate (EC) decomposition on the cathode, a solvent commonly used in the electrolyte of Li-ion cells [36]. From numerical simulations, the mechanisms of this decomposition are understood, and this work represents a first approach in the electrolyte breakdown modelling.

Several general-purpose chemical models for polymer pyrolysis have been developed and can be used for Li-ion cell separator thermal degradation [59-61]. For example, Kruse *et al.* developed a polypropylene pyrolysis model that includes over 24000 reactions and tracks 213 polymeric species [59]. Levine *et al.* developed a high-density polyethylene pyrolysis model that includes over 11000 reactions and tracks 151 polymeric species [60].

Despite the considerable difficulty to assemble a global cell model from sub-models of individual condensed-phase components, attempts can be found in the literature. Kim *et al.* developed a three-dimensional finite volume model for a Li-ion cell [62]. This model considers an oven test simulation where the thermal runaway is triggered by an internal short-circuit represented by a localized heat source. It considers the non-isotropic properties resulting from the different layers of material inside the cell. Several exothermic reactions are modelled including the SEI layer decomposition, the anode-solvent reaction, the cathode-solvent reaction, and the decomposition of the electrolyte. This simulation highlighted that thermal runaway is more easily triggered in cells with a large volume because the surface/volume ratio

is less important and contributes to a worse heat dissipation. The model developed by Melcher *et al.* is similar [63]. This model considers several exothermic reactions and the heat generated by the electric current inside the cell. Nevertheless, the simulation cannot determine the duration of the thermal runaway because it considers the concentrations of the species as constants.

Tanaka provides a good overview of model development for several chemical reactions which take place in Li-ion cells [64]. Chemical reactions including the SEI formation, the SEI decomposition, the oxygen release on the cathode and the solvent oxidation are explained and models are described.

2.3.3 Gas combustion modelling

This section reviews the state of the art on the models for the combustion of the gases released during the thermal runaway. These models aim to describe what happens when the outgassing meets an oxidizer and burns.

Quintiere [50] calculated the energy of combustion of the vented gases using two methods, one by considering the THC and another by considering only methane and ethylene. The relative error between the results was approximately 30%. This result reveals that simple measurements can be useful to estimate heat of combustion if the detailed composition is not known. Johnsplass [65, 66] has simulated the combustion of the vented gases of three different Li-ion cell technologies (LCO, LFP and NMC) in his master's thesis. The objective was to determinate properties such as the laminar burning velocity, the volume expansion ratio at constant pressure, the pressure generated from constant volume combustion and the deflagration index. He used the software Cantera 2.3.0 to implement a detailed chemical simulation based on the two chemical mechanisms: GRI-Mech 3.0 and the DMC-Mech. He relied on data from a calorimetry study where Golubkov *et al.* [24] measured the composition of the vented gases for three Li-ion cells. These properties were then used to simulate the turbulent premixed combustion flow of the vented gases in a confined area with the software OpenFOAM, which was compared with an experiment. The results show that the vented gases have approximately the same combustion properties as methane and propane. Nevertheless, the validation of such results with real experimental data is not trivial because of large uncertainties in the measurements.

2.4 Discussion on the test methods in certification standards

The literature review presented here reveals significant differences between the certification standards and the test methods available in the scientific community. These differences are easily explained because these two activities serve very different purposes. Certifications are only meant to assess the ability of a product to serve a specific purpose, while the scientific studies discussed are designed to increase the understanding of the phenomenon at play during thermal degradation. Certification standards are made to validate a design of Li-ion cells or batteries and consequently they are developed to yield clear pass/fail verdicts while relying on simple instrumentation, to be in line with the needs of the industry. On the contrary, test methods implemented in scientific studies are much more complex and give access to a lot of information. The literature shows that significant effort has to be made to develop and improve tools adapted for the field of lithium-ion cells. For example, cone calorimeter measurements do not appear in Li-ion cells certification standards but allow the quantification of parameter dependencies for the heat release rate.

The thermal runaway is a very complex phenomenon because of the close coupling between phenomena arising from different disciplines, including chemistry, combustion, solid and fluid mechanics. A lot of work has been made in these different domains but complete models that consider them together as well as their interaction in Li-ion cells do not exist. Regarding combustion studies, a lot of progress has been made in recent years. Fire calorimeters allow for the determination of several combustion parameters, including the temperature of combustion, the heat release rate, and the volume of vented gases. Modern gas analysis methods can also yield the composition of the vented gases. Nevertheless, in-line gas analysis is still very challenging when the composition of the gas changes rapidly, which is the case for the outgassing of Li-ion cells undergoing thermal runaway. Finally, complete combustion simulations coupled with detailed solid-phase chemistry still need to be developed to have a better understanding of the risks associated with thermal runaway.

2.5 Project objectives

The literature review reveals that the thermal runaway has been extensively studied over the last few decades. The understanding of this phenomenon remains however incomplete, especially when it comes to the combustion of the outgassing generated during thermal runaway. This combustion is responsible for the main fire threat to adjacent structures in an

aircraft and can drive cascade failure of neighbouring cells. Moreover, the effects of important parameters such as the heating rate or cell ageing remains largely unknown. In previous studies, different gas analysis techniques were used to characterize the outgassing of the cell and characterize the fire hazard it represents, including FTIR and GC-MS. Unlike GC-MS, FTIR allow the measurement of the gas species concentration as a function of time but is not as sensitive. To close this gap, it could be interesting to implement on-line mass spectrometry (MS) to combine the sensitivity of GC-MS with the time resolution of FTIR.

Li-ion cells have a complex composition, and the flames observed following thermal runaway are driven by the combustion of the hydrocarbons they contain. The resulting flame is dirty and results in the formation of particulate matter, known to have severe detrimental health and environmental effects. The size distribution of the particulate matter emitted upon thermal runaway has not been studied significantly and represents a serious knowledge gap that must be closed to enable the development of modelling tools sufficiently powerful to capture all threats associated with Li-ion battery fires.

In this project, a cone calorimeter is used to test and collect data from the combustion of gases released during the thermal runaway of Li-ion cells. The heating system used to impose a thermal stress on the cells controls the temperature and the heating rate, logging the conditions that can then be replicated on further studies. The effects of heating rate and ageing are studied using temperature, heat release, smoke production rate and mass loss measurements. Temperature measurements acquired with an infrared camera are compared to thermocouple measurements to evaluate the suitability of this tool. The composition of the outgassing is studied with a mass spectrometer and the particle size distribution is obtained with two particle-size spectrometers operating simultaneously.

A limited numerical simulation effort is also undertaken in this project, including three models of simplified combustion configurations. The first is a basic premixed 0D combustion simulation where a mixture of gas emitted during a Li-ion cell thermal runaway is burned with air. The second is a 1D counterflow diffusion flame simulation where the combustion takes place between a jet representative of the cell outgassing and an opposed air flow. The third is a 1D premixed flat flame simulation where a mixture of air and combustible is projected through a specific burner (e.g. a porous material inlet) to create a burner-stabilized flat flame.

CHAPTER 3 TEST PROTOCOL AND MODELLING APPROACHES

3.1 Experimental methods

The following details the equipment, the test protocol and the data that is measured during the tests. This first section ends with an error analysis and a critical discussion.

3.1.1 Equipment

3.1.1.1 Cone calorimeter

The cone calorimeter was assembled in Polytechnique by a PhD student (Stefan Cristian Boanta). It was designed in accordance with the ISO 5660-1 standard. This setup allows the measurement of mass loss, temperature of combustion and heat release rate by oxygen consumption. The data from the sensors are recorded using LabVIEW. An overview of the entire setup can be seen in Appendix A. The general operating principle is as follows: the heat released during the combustion is calculated based on the amount of oxygen that reacts. Generally, a sample to be tested is heated by an infrared heater and a continuous flow of air is supplied below the sample holder. An igniter is placed over the sample and initiates the combustion of the gas released by pyrolysis in the sample. The burnt gases are then diluted with air and collected by an exhaust hood to be analysed. The weight of the sample is also measured during the entire test.



Figure 3.1: Picture of the cone calorimeter at Polytechnique Montreal

Two acquisition cards are used in the setup. The first one acquires data from the cone calorimeter and the second one acquires data from the thermocouples on the heating system. The data are read using the LabVIEW software environment. The first acquisition card is the USB-6351 from National Instruments. It has 16 analogue inputs, 2 analogue outputs, 24 digital inputs/outputs and an acquisition frequency of 1.25 MHz. The second acquisition card is the USB-9213 from National Instruments. It has 16 thermocouple inputs and a maximum acquisition frequency of 75 Hz.

A paramagnetic oxygen sensor is used to obtain the O_2 concentration in the exhaust (Paracube Premus- α from Hummingbird). This model was selected because of its precision-cost ratio. It measures the oxygen concentration in the exhaust gases. Knowing the concentration of O_2 in air, the O_2 consumption by the combustion process can be calculated to determine the heat release rate. The specifications certify an intrinsic error of $\pm 0.1\%$ O_2 maximum and an output fluctuation of $\pm 0.01\%$ O_2 . Thus, the total measurement error is $\pm 0.11\%$ O_2 .

A pressure sensor is required to determine the flow rate of the exhaust gas. It measures the pressure differential before and after the orifice plate of the cone calorimeter. The sensor is a P993-1B from Sensata-Kavlico. The specifications certify a measurement error of 2% on the maximal span.

The smoke obscuration measurement instrumentation has been assembled in accordance with the ISO 5660-1 standard. It is composed of a red HeNe laser from Meredith Instruments (ref. HNS-2P-663), with lenses, beam splitters, filters and photodiodes from Edmund Optics and opto-mechanical parts from Newport. A detailed schematic representation of the setup with an exhaustive list of the parts is presented in Appendix B.

The mass sensor is from Bolsen Tech (ref. AREEY470) and is composed of a small aluminium beam equipped with four strain gauges that operate on the principle of the Wheatstone bridge. The measurement error of this sensor is not known but can be approximated by ± 0.01 g in view of the measurements taken. However, considering the thrust exerted on the battery by the violent venting during thermal runaway, the measurement of the mass loss rate within the cone calorimeter will be subject to unknown uncertainties. This sensor, in combination with a conventional scale will therefore also be used to calculate the total mass loss during a test.

3.1.1.2 Li-ion cells and battery charger

The cells used for this study are the SAMSUNG 18650 25R with 2.5 Ah capacity and a 3.6 V nominal voltage. They are widely used rechargeable Li-ion cells.



Figure 3.2: Picture of the SAMSUNG 18650 25R Li-ion cells

The battery charger is a basic model (B083SH6BB3 from VIWIPOW). This device allows four cells to charge simultaneously and gives the current state of charge for each cell. No measurement error on the state of charge is given and cells will be charged at full capacity.

3.1.1.3 Heating system

The heating profile is controlled by a PID controller, model CN16DPT-440 from OMEGA, allowing the definition of several programs to control the heating rates and the temperatures.

The temperature is measured by a thermocouple located on the surface of the cell. This system sends a DC pulse signal to a solid-state relay that controls the electric current in the heating cable (ON/OFF heating). The solid-state relay (SSR) used is the SSRL240DC25 from OMEGA. It is controlled by a DC pulse signal from 3 to 32 Vdc and can support a 24 to 280 AC line voltage. The heating cables are high-temperature heaters for pipes and tubes from McMaster (ref. 3641K22). These 30 cm long cables can reach 482 °C and have a maximum heating power of 50 W.

Type K thermocouples are used to measure the temperature of the cell, over a range between 0 °C and 1100 °C, sufficient for thermal runaway experiments. Type R thermocouples are used for temperature measurements of the gases released and of the flame. This type of thermocouple has a temperature range between 0 °C and 1450 °C. For temperature measurements in the gas released and the combustion environment, these R-type thermocouples are coated with a thin layer of inert material (ceramic cement) to avoid catalytic heating effects, that can increase the temperature measured, while maintaining a fast response time. The sensors are grounded for the temperature measurements of the cell casing. These thermocouples have a measurement error of $\pm 0.75\%$. A diagram of the setup is exposed in Figure 3.3.

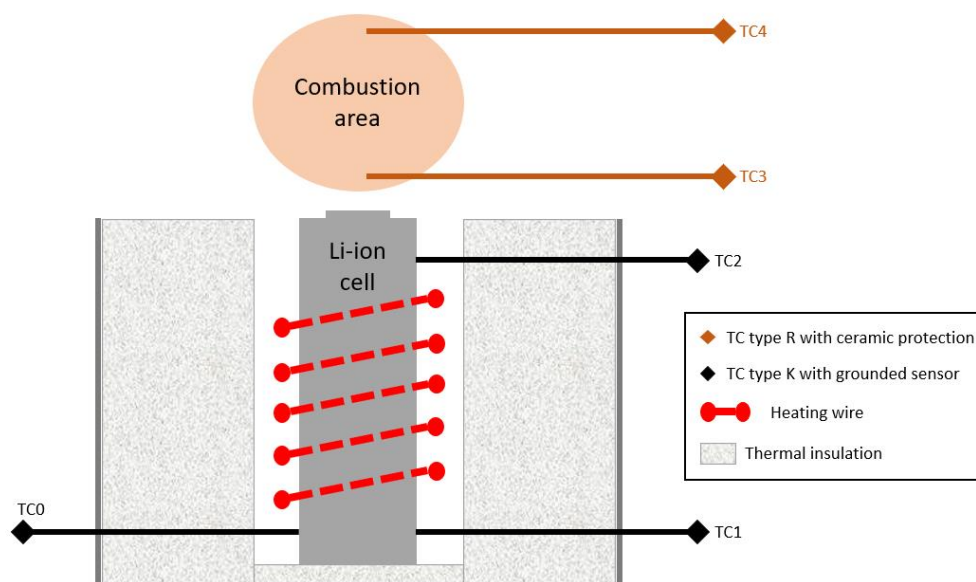


Figure 3.3: Schematic representation of the heating setup

3.1.1.4 Additional instruments

Measurements of gas composition as a function of time are realized with a mass spectrometer (Cirrus 1 (LM99) from MKS Instruments). It is an on-line gas analysis system designed to work

at atmospheric pressure. This instrument is very sensitive with a detection limit of 100 ppb. However, the response is highly variable as a function of the nature of the species measured and of the overall composition of the mixture. An extensive calibration is required to obtain quantitative measurements in multicomponent gas mixtures [67], such as the one expected following thermal runaway. The mass spectrometer can measure over the 1-200 atomic mass units (amu) range, with a full scan requiring approximately 90 seconds. Thus, a limited number of species will be considered to reduce the scan time.

Particle size distribution in the flame is investigated during the experiments with two particle size spectrometers operating simultaneously. The first one is a 3775-3082 scanning mobility particle sizer (SMPS) from TSI. This device has an adjustable measuring range from 10 nm to 1000 nm. In this project, the spectrometer has been set to scan particles with a diameter included between 18.8 nm and 532.8 nm and to have a scan duration of 1 minute and 16 seconds. The second one is the Mini-LAS model 11-R from Grimm Aerosol Technik. This device has a fixed measuring range from 0.25 μm to 32 μm and has been set to have a scan duration of 6 seconds.

A multispectral camera is used to record infrared videos of the experiments. The camera is a MS M350 from Telops. This camera has a rotating wheel that includes eight filters with different temperature ranges and transmittances over different spectral bands. Filters 1, 2 and 3 allow measurements over the whole spectral band of the camera sensor (1.5 μm to 5.4 μm) but are calibrated for different temperatures, the temperature range for each filter is given in the last column of Table 3.1. Filters 4 and 5 focus on the emission peaks of H_2O and CO_2 , respectively. Filters 6, 7 and 8 allow to see through the flame as their transmission peaks correspond to low absorption valleys in the H_2O and CO_2 spectra. This camera can record with a maximal resolution of 640x512 pixels at a frame rate of 500 Hz.

Table 3.1: Description of the eight filters of the multispectral infrared camera

Filter number	Description	λ_{\min} [nm]	λ_{\max} [nm]	Transmittance	Temperature [°C]
1	Broadband window	1500	5400	95.00 %	10-338
2	OD 1.65	1500	5400	2.33 %	207-1500
3	OD 3	1500	5400	0.10 %	539-1500
4	H2O	2987	3038	70,90 %	408-1440
5	CO2 red spike	4382	4597	85.00 %	155-850
6	Through flame 1	3649	3763	80.00 %	225-1194
7	Through flame 2	3773	3809	71.60 %	297-1500
8	Through flame 3	3945	3983	71,71 %	282-1500

A high-speed camera is also used to record the tests. This allows the determination of the flame shape and the visualization of the thermal runaway process, as it can be seen in Figure 3.4. The camera is a Fastcam Mini AX200 from Photron. This model can record colour video at a rate included between 6 400 fps (1024x1024 pixels) and 900 000 fps (128x16 pixels).

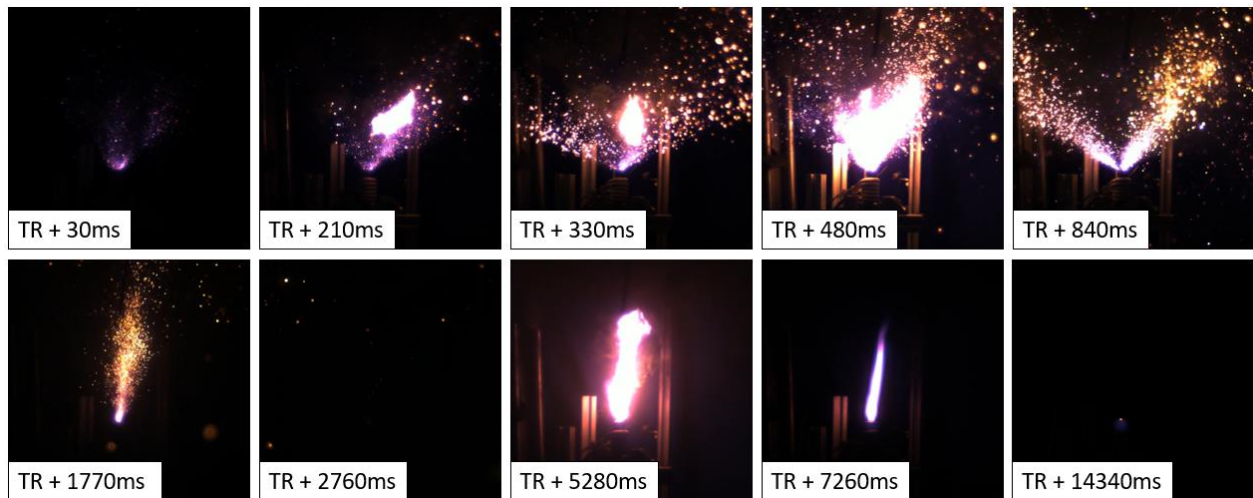


Figure 3.4: High-speed camera recording of Li-ion cell TR

A conventional camera is used to record normal-speed footages of the tests. It also allows to record the sound emitted during the thermal runaway. The camera is a RX100 III from Sony.

3.1.2 Test protocol

The test protocol implemented in this study is based on the section “Test method for single cell thermal runaway via overheating” of the DO-311A standard from the Radio Technical Commission for Aeronautics (RTCA). This document is an international standard for

rechargeable lithium batteries and battery systems, it establishes testing methods for the verification and characterization of the safety and performances. The protocol has been slightly adapted for the needs of this project. The cell is not part of a battery, thus the “element under test” specified in the standard is a single cell. The heating rate can be higher than the standard specification (maximum heating rate in the DO-311A: 10 °C/min). To ensure that combustion is observed in all our tests, the heating ramp resumes and continues until thermal runaway occurs if nothing happens after the first venting and if the cell temperature falls back below 55 °C.

The protocol is based on the following:

- The cell is charged at 100 % state of charge (SOC).
- The ambient temperature is approximately 25 °C.
- The temperature at the surface of the cell is stabilized at 55 °C during 3 min.
- The cell is heated at a rate included between 5 °C/min and 20 °C/min until 200 °C where the temperature is maintained.
- When the first venting appears, the heating system is stopped.
- If the thermal runaway does not happen as the cell temperature falls back below 55 °C, the heating ramp starts again and continues until the thermal runaway is triggered.

3.1.3 Error analysis

The uncertainty of the temperature measurement is given in the thermocouple datasheet.

$$\frac{\Delta T}{T} = 0.0075 = 0.75 \%$$

The heat release rate $\dot{q}(t)$ is determined from the O₂ consumption using the relation given in the ISO 5660-1 standard:

$$\dot{q}(t) = 1.10 * \frac{\Delta h_c}{r_0} * C * \sqrt{\frac{\Delta p}{T_e}} * \frac{X_{O_2}^0 - X_{O_2}(t)}{1.105 - 1.5X_{O_2}(t)}$$

Where the ratio between the net heat of combustion and the stoichiometric oxygen/fuel mass ratio $\frac{\Delta h_c}{r_0}$ is taken as 13.1*10³ kJ/kg as specified in the ISO 5660-1 standard. $X_{O_2}^0$ is the average of the oxygen analyser output (mole fraction of oxygen) during 1 min without combustion,

$X_{O_2}(t)$ is the mole fraction of oxygen at time t (considering the delay time of the oxygen analyser), 1.10 is the ratio of molecular weights of oxygen and air, Δp is the difference of pressure at the orifice plate of the cone calorimeter, T_e is the temperature of the gas mixture at the orifice plate and C is a calibration constant.

The calibration constant C is calculated using:

$$C = \frac{\dot{q}_b}{1.10 * (12.54 * 10^3)} * \sqrt{\frac{T_e}{\Delta p}} * \frac{1.105 - 1.5X_{O_2}}{X_{O_2}^0 - X_{O_2}}$$

Where \dot{q}_b is the heat release rate in kW for the methane supplied during the calibration test ($\dot{q}_b = 5 \pm 0.5$ kW) and $\frac{\Delta h_c}{r_0} = 12.54 * 10^3$ for methane.

The total relative uncertainty on the heat release rate is given by (see appendix C for the development):

$$\frac{\Delta \dot{q}}{\dot{q}} = 0.1 + \frac{\Delta T_e}{T_e} + \frac{\Delta(\Delta p)}{(\Delta p)} + 2 * \frac{\Delta X_{O_2}^0 + \Delta X_{O_2}}{|X_{O_2}^0 - X_{O_2}|} + 2 * \frac{\Delta X_{O_2}}{X_{O_2}}$$

Where 0.1 is the relative uncertainty on \dot{q}_b .

3.2 Modelling

Combustion simulations are implemented on Cantera using the GRI-Mech 3.0 reaction mechanisms. This mechanism considers 53 chemical species and 325 reactions and is widely used to model the combustion of light hydrocarbons such as methane or propane. All the governing equations used in these simulations are summarized in Appendix D and Appendix E.

3.2.1 Modelling approaches

3.2.1.1 0D combustion simulation

The 0D simulation is a simple model that allows the determination of the properties of a reactive gas mixture at chemical equilibrium, following combustion. It requires as inputs the composition and the temperature of the gas mixture that is vented out of the cell, as well as the fuel-air equivalence ratio for the combustion process. It allows the calculation of the composition of the exhaust gas, as well as the temperature and the enthalpy change once the

chemical equilibrium is reached. It also allows the flammability limits of the gas mixture to be investigated and provides the ignition delay (generally a few tens of milliseconds). It does not consider the propagation of the combustible species into the surrounding atmosphere. Therefore, to yield useful results, the composition of the gas mixture must be representative of what is ejected from the cell and mixed with an amount of ambient air controlled by the surrounding fluid mechanics. The air proportion in the mixture can be adjusted by changing the value of the fuel-air equivalence ratio (Φ), defined as the ratio of the actual fuel-to-oxidizer ratio ($n_{fuel}/n_{oxidizer}$) to the stoichiometric fuel-to-oxidizer ratio ($(n_{fuel}/n_{oxidizer})_{stoichiometric}$). Therefore, there is an excess of fuel compared to the stoichiometric reaction (complete combustion) when Φ is greater than one and the opposite is true when Φ is lower than one. The temperature of the gas mixture and the ambient pressure are also required as input.

$$\Phi = \frac{n_{fuel}/n_{oxidizer}}{(n_{fuel}/n_{oxidizer})_{stoichiometric}}$$

With Φ [-] the fuel-air equivalence ratio, n_{fuel} [mol] the number of moles of fuel mixture and $n_{oxidizer}$ [mol] the number of moles of air. This simulation uses the “IdealGasConstPressureReactor” class in Cantera. This class considers a homogeneous, constant pressure and zero-dimensional reactor for ideal gas mixtures combustion.

Table 3.2: Overview of the inputs/outputs of the 0D simulation

Inputs/Parameters	Outputs
<ul style="list-style-type: none"> • Temperature of the gas mixture • Composition of the gas released by the Li-ion cell • Fuel-Air equivalence ratio 	<ul style="list-style-type: none"> • Composition of the combustion gas • Flammability limits • Temperature of combustion • Enthalpy of combustion

3.2.1.2 1D flame simulations

The 1D simulations add realism compared to the previous 0D configuration by considering species and heat transport to the reaction zone, in addition to the stoichiometry of the reaction. Outputs include the temperature and the thickness of the flame, the gas species repartition (flame structure), and the HRR per unit area of the flame. Two approaches are implemented: a counterflow diffusion flame and a premixed flat flame. The counterflow diffusion flame

considers the case of the gas mixture encountering an opposed jet of air. Therefore, this approach is adapted to model the thermal runaway combustion of a cell directly exposed to an oxidizing atmosphere. In the premixed flame approach, the mixing between the vented gas and air is assumed to be complete prior to ignition.

The counterflow diffusion flame configuration considers two axisymmetric inlets with flows in opposed directions. Figure 3.5 shows a schematic representation of this type of model. The gas flow exiting the left inlet is composed of the gases emitted by the Li-ion cell during thermal runaway. The gas flow entering from the right inlet is air (78 % mol N₂; 21 % mol O₂; 1 % mol Ar). The flame is located close to the stagnation plane between the two inlets. Here, the transport and the energy equations are solved in 1D (along the jet axis). A diffusion flame is what is expected at the cell vent during the combustion phase of the thermal runaway. However, the opposed air jet is obviously an oversimplification of what is encountered in practice as the fuel mixture is emitted in quiescent air. Nevertheless, this configuration is a common test case useful to qualitatively investigate ignition and flame structure.

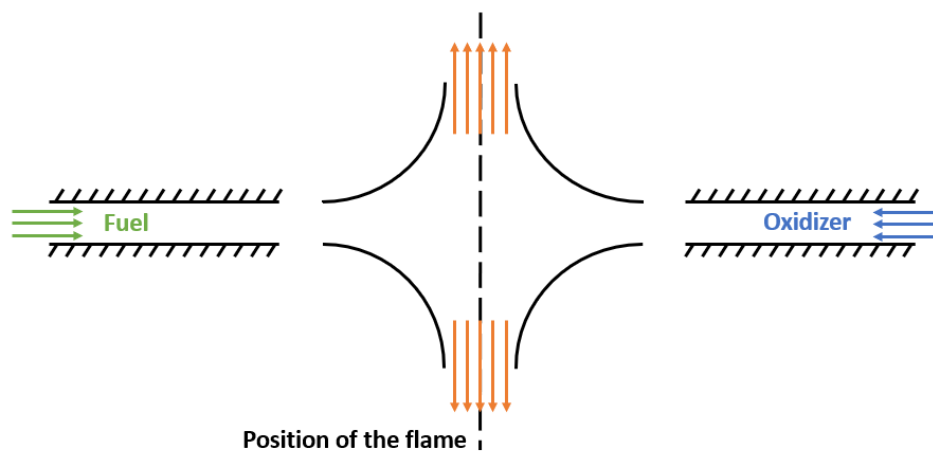


Figure 3.5: Schematic representation of the counterflow diffusion flame model

This model is implemented using the “CounterflowDiffusionFlame” class in Cantera. The simulation requires gas temperatures, gas compositions and mass flow rates per unit area of the two inlets. The distance between the two inlets and the environment pressure are also required. Realistic gas temperatures, flow rates and composition were chosen from experimental data measured on Li-ion cell thermal runaway tests performed by Safran.

Table 3.3: Overview of the inputs/outputs of the counterflow diffusion flame model

Inputs/Parameters	Outputs
<ul style="list-style-type: none"> • Temperature, composition, and mass flow rate per unit area of the released gas mixture • Temperature, composition, and mass flow rate per unit area of the atmospheric air 	<ul style="list-style-type: none"> • Temperature of the flame • Heat release rate (HRR) • Gas species repartition in the flame

The premixed flat flame model considers a homogeneous mixture of fuel and oxidizer flowing through a porous inlet to create a burner-stabilized flat flame. This configuration is relatively easy to reproduce experimentally and is therefore a great approach to study premixed flame. This aims to model what would happen in the vents of a battery module, where the outgassing could mix with air prior to combustion. Figure 3.6 shows a schematic representation of this model. The combustion takes place downstream the porous inlet. The fuel mixture is composed of the gases released during a Li-ion cell thermal runaway, premixed with air (78 % mol N₂; 21 % mol O₂; 1 % mol Ar) added as an oxidizer.

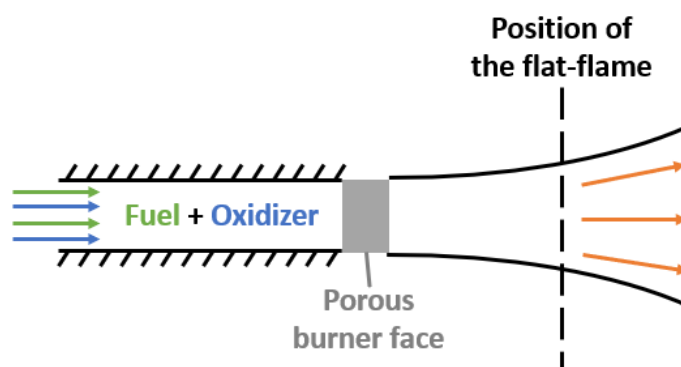


Figure 3.6: Schematic representation of the premixed flat flame

This approach uses the “BurnerFlame” class in Cantera. The simulation requires the inlet gas mixture temperature, composition, and mass flow rate per unit area. The composition can be adjusted with the fuel-air equivalence ratio (Φ). It also needs the environment pressure and the width of the spatial domain.

Table 3.4: Overview of the inputs/outputs of the premixed flame model

Inputs/Parameters	Outputs
<ul style="list-style-type: none"> • Temperature, composition, and mass flow rate per unit area of the released gas mixture • Fuel-Air equivalence ratio 	<ul style="list-style-type: none"> • Temperature of the flame • Heat release rate (HRR) • Gas species repartition in the flame

3.2.2 Critical discussion.

It can be observed that the GRI-Mech 3.0 reaction mechanism does not consider all the chemical species that can be found in Li-ion cell thermal runaway. This reaction mechanism is an optimized model for natural gas combustion where species such as SO₂, HCl or HF are not found. Therefore, the hypothesis that these gas species do not participate in the combustion process is required. Moreover, the configurations implemented in the simulations cannot be experimentally verified in this project due to the specific setup required.

The oversimplification in the different models must be also highlighted. The 0D combustion model considers a homogeneous gas mixture, which is not the case in reality. The 1D flame simulations consider a constant composition of the gas mixture. However, the gas mixture expelled off the cell constantly changes in reality. The geometry and air flow in battery case vent are also not considered in the 1D flame simulations, and this is critical to determine the real flame chemistry. Moreover, the counterflow diffusion flame model considers an opposed air flow, which does not exist in reality, outgassing likely exiting in quiescent atmospheres. A value must be assumed for this parameter to obtain plausible results.

CHAPTER 4 ARTICLE 1: ANALYSIS OF LI-ION CELLS DEGASSING AND COMBUSTION UNDER THERMAL RUNAWAY

Keywords: Lithium-ion; Thermal runaway; Cone calorimeter; Heat release rate; Particle size distribution; Mass spectrometry; Infrared camera; Calorimetry; Smoke production; Overheating; Combustion

Submitted in the Journal of Power Sources on January 19th, 2022.

Authors: V. Goupil^{a,b}, C. Gaya^c, A. Boisard^d, E. Robert^a

^a Ecole Polytechnique Montréal, 2500 chemin de Polytechnique, Montréal, QC H3T 1J4, Canada

^b Ecole des Arts et Métiers, rue Saint-Dominique BP 508, 51000 Châlons-en-Champagne, France

^c Safran Electrical and Power, rue des Longs Quartiers, 93100 Montreuil, France

^d Safran Tech, 1 rue des Jeunes Bois, Châteaufort, CS 80112, 78772 Magny-les-Hameaux, France

4.1 Abstract

Thermal runaway (TR) is a major issue in the development of Li-ion cells, causing security concerns for end-users, especially in the transportation. Here we investigate the TR of 18650 Li-ion cells under constant heating rate in a cone calorimeter. The effect of the heating rate was observed on the outgassing and cell casing temperatures, as well as on the thermal power of the flames produced and resulting smoke characteristics. Analysis of outgassing based on four main gases was enabled through mass spectrometry and the size distribution of the particulate emission was measured with aerosol spectrometers. The results revealed that the heating rate (from 5 °C/min to 20 °C/min) had an impact on the course of TR events, with high heating rates resulting in more violent TR. The initial temperature of the first venting also increased with higher heating rates. However, cell and outgassing temperatures did not seem to be impacted by this parameter. Cells subjected to an intermediate heating rate (i.e. 10 °C/min) showed maximum heat release rate and minimum smoke production. Mass spectrometry measurements revealed that the first venting mainly released vaporized electrolyte (DMC) with a small quantity of CO₂. During the combustion associated with the major venting event, the gases released were mainly CO₂ and H₂O, with small quantities of H₂ and DMC, and sporadic detection of C₃H₆, LiF and C₆H₆. The high-resolution size distributions obtained for the particulate emission showed a bimodal distribution, characteristic of very rich diffusion flames.

4.2 Introduction

Interest for rechargeable batteries is rising with the global increase in energy consumption combined with the need to reduce reliance on fossil fuels. Li-ion batteries are currently the dominating technology, as demonstrated by their extended use in the portable device and electrical vehicle (EV) markets [68, 69]. These developments were made possible by Li-ion cells properties: high energy density and high nominal voltage [1]. The counterpart of these advantages is a significant thermal instability [11, 70] leading to the so-called thermal runaway (TR) phenomenon. TR is the result of an uncontrolled exothermic reaction chain which produces flammable and toxic gases [15, 71-75] and can lead to flaming combustion (i.e. combustion with a visible flame) and explosions [11, 76]. TR can be the result of fabrication defects [77] or triggered by exposure to abusive environments or operating conditions (e.g. overcharging or overheating).

Among the different TR initiation methods, overheating warrants special attention as several causes can generate it within a battery pack : i) failure of the cooling battery management systems, ii) heat transfer from adjacent cells undergoing TR resulting from internal defects (short-circuit), or iii) unexpected high temperature from the environment (external flames). Depending on the heating rate applied and cell state (e.g. state of charge (SOC), state of health (SOH), ageing), TR behaviour can be drastically modified [34, 78, 79]. Understanding the key parameters influencing TR is of paramount importance to develop safe battery pack, especially when targeting aircraft applications [80] where resistance to fire is assessed through stringent certification requirements [81]. Here we investigate the effect of the heating rate on the thermal power released during the flaming combustion associated with the TR of 18650 Li-Ion cells and provide insights on the gaseous species temporal evolution and particulate matter emitted.

The different phases of the TR phenomenon can be described as shown in Figure 4.1: 1) cell heating, 2) outgassing inducing a slight decrease of the cell heating rate and 3) the thermal runaway itself, when a temperature threshold is reached. This leads to violent exothermic reactions within the cell inducing a large outgassing that ejects most of the cell material and often results in the production of flames and smoke. Cell casing rupture and explosion can also be observed.

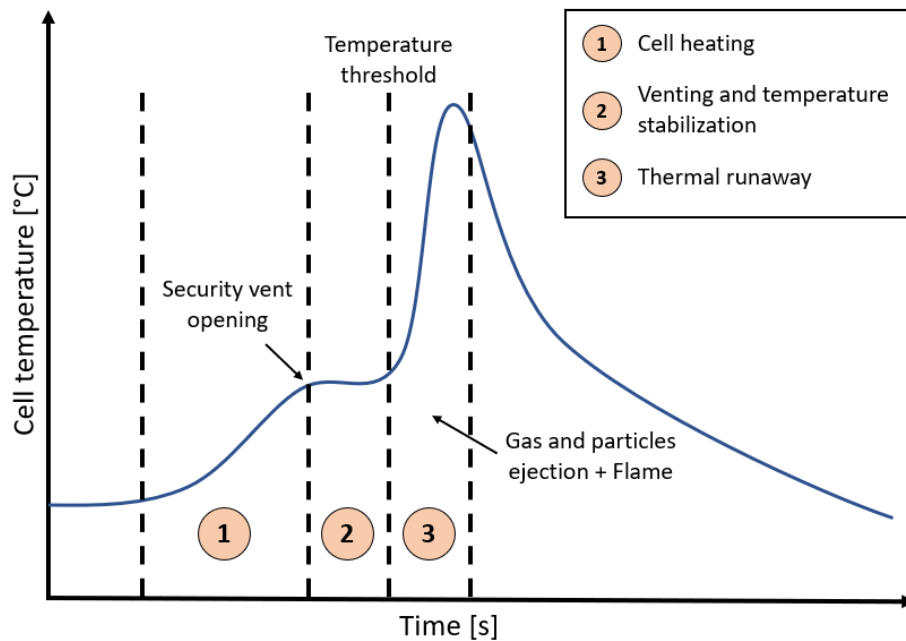


Figure 4.1: Li-ion cell temperature evolution during TR

The opening of the cell safety vent and the subsequent major venting event are critical to characterize, as the risk of fire and explosion is high. The flammable gases emitted have different origins: they can stem from the evaporation or pyrolysis of the organic solvent in the liquid electrolyte or can be the result of thermal decomposition in other components: electrolyte additives, lithium salt, electrode binder, separator, or cell packaging [30]. When a cell is undergoing thermal runaway, the risk of flaming combustion is closely related to the temperature, composition and flow rate of flammable gases emitted. Unfortunately, these parameters evolve quickly during TR, with a timescale of a few seconds, and information that would allow modelling of the risks associated with this combustion is still scarce in the literature. In this work, we are implementing advanced diagnostic tools in the single cell thermal runaway containment test, as described in RTCA's DO-311A standard [8], to provide time-resolved measurement of the combustion heat-release rate, outgassing composition, smoke density, flame and cell casing temperature as well as particle concentration and size distribution.

The combustion phase of the TR has been extensively studied in the literature. Calorimetry-based experiments typically focus on quantifying the heat released within and around the cells [82-85]. In a cone calorimeter, heat release rate (HRR) measurements are usually based on the oxygen consumption principle [9], and therefore only the energy associated with the combustion taking place outside the cells with ambient air as oxidizer can be measured [86]. From the time-dependent signal obtained, the duration, peak HRR and total energy associated with combustion can be extracted to characterize the fire risk posed by the TR. To capture the total heat release, including exothermic processes internal to

the cell and combustion driven by the oxygen it contains, more advanced calorimeters are needed, typically featuring an adiabatic test section or one where the heat flux can be measured [50]. It is interesting to note that material decomposition energy was shown to be as high as 2 times the cell electrical energy while the combustion-linked energy can be up to 6 times the cell electrical energy [87].

The effect of the heating rate on the combustion associated with TR has only been studied partially, but this parameter appears to have a significant influence as the HRR and thus the severity of the fire risk have been observed to increase with the heating power [79]. The heating method must also be considered as local heating can trigger a violent TR while a more uniform temperature increase typically leads to non-explosive TRs [88].

The composition of the outgassing during thermal runaway has been measured using Fourier transform infrared spectrometry (FTIR) and gas chromatography coupled with mass spectrometry (GC-MS). Unlike GC-MS, FTIR allows online gas analysis with a good temporal resolution but has a lower sensitivity. GC-MS is very sensitive, but the results depend on the database used to identify the gas compounds and are dependent on both the concentration and the ionization propensity of each gas specie [67, 89]. Ribière *et al.* analysed the outgassing of pouch-type Li-ion cells by FTIR on a cone calorimeter, quantifying the concentrations of combustion related gases such as CO, CO₂, O₂ and of toxic gases such as HF, NO, SO₂ and HCl [30]. Larsson *et al.* also studied the gas emission of pouch-type Li-ion cells and focused their work on the emission of toxic species such as HF and POF₃, revealing that the amount of HF decreases with the decrease of SOC [49]. Spinner *et al.* analysed the outgassing of cylindrical Li-ion cells by FTIR, focusing on the concentration of CO₂, CO, SO₂, O₂ and CH₄ [29]. Chen *et al.* used GC-MS and analysed lower explosive limit (LEL) as a function of SOC and heating power [72]. They revealed that the LEL increases and then decreases with the increase of the SOC and that the LEL decreases with the increase of heating power. Gachot *et al.* developed a very sensitive gas analysis tool using gas chromatography (GC) coupled with FTIR and mass spectroscopy (MS) [89], but unfortunately it does not allow online measurements. Abd-El-Latif *et al.* used accelerating rate calorimetry (ARC) coupled with a mass spectrometer (MS) to perform online gas analysis on both unaged, cycled and overcharged Li-ion cells, revealing the presence of DMC and EMC during cell venting and of C₂H₄, CO₂ and POF₃ during cell explosion [85].

The increased use of Li-Ion batteries in transportation systems, both terrestrial and airborne, means that in addition to thermal aspects, particulate emissions associated with TR must also be considered to ensure the safety of the occupants. Knowledge of the particle size distribution resulting from the

combustion of the TR outgassing is very limited, for instance Zhang *et al.* reported sizes and compositions, but only for prismatic cells [90]. They revealed that the particulate emission accounts for 11.20 % of the cell initial mass and that the particles median size is 198 μm , but the use of sieves for particulate emission analysis limited the precision and the size range of the results.

In this work, we first perform a quantification of the thermal aspects of the TR of 18650 Li-ion cells using a cone calorimeter, focussing on the effects of the heating rate. We implement multispectral infrared imaging to complement temperature measurements obtained from thermocouples. The effects of the cell heating rate during TR initiation on the cell and outgassing temperatures, heat release rate, volumetric smoke production and mass loss are described. In the second part of the paper, the outgassing is analysed using a mass spectrometer and two particle size spectrometers, yielding time-resolved information on the gas composition and the particles size distribution.

4.3 Experimental methodology

4.3.1 Li-ion cells and heating system

The most extensively used Li-ion cell format is the cylindrical 18650, with an 18 mm diameter and a 65 mm height. In this study, the cells tested were 18650, with 2.5 Ah capacity and a 3.6 V nominal voltage. All the cells were new and fully charged up to 4.2 V (100 % SOC), with the plastic wrapping surrounding the casing removed to facilitate heating.

The heating system is composed of a cylindrical holder (stainless steel) filled with thermal insulation (Fiberfrax HAS from Unifrax). The cell was wrapped with a heating wire (McMaster ref. 3641K22) and inserted within the holder as shown in Figure 4.2. A PID controller (Omega engineering, CN16DPT-440) and a K-type thermocouple (TC0) in contact with the cell casing ensured a controlled and constant heating rate. The cell temperature was also measured using two K-type thermocouples (TC1 and TC2). The outgassing and flame temperatures were obtained 2 cm (TC3) and 12 cm (TC4) above the positive pole of the cell using R-type thermocouples. TC3 and TC4 were coated by a thin layer of liquid ceramic (Omega engineering, Omegabond 500) to prevent catalytic heating effects with the platinum-based thermocouple material.

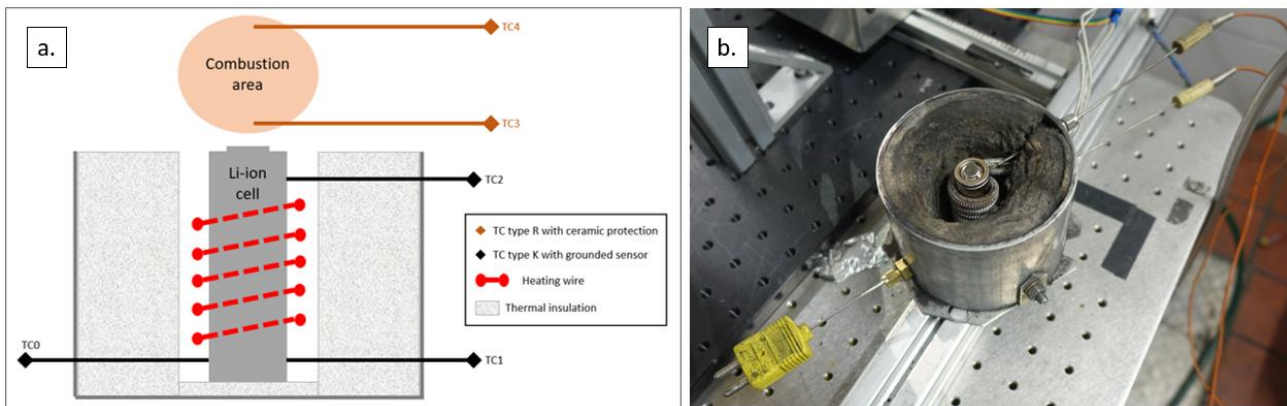


Figure 4.2: Overview of the heating setup: schematic representation (a) and picture of the real setup with TC0, TC1 and TC2 visible (b)

4.3.2 Cone calorimeter

The analysis of the heat released by the outgassing combustion was done using a cone calorimeter with an exhaust flow rate of 24 L/s. The cell holder was placed inside an open chamber made of four Plexiglas panels, located immediately below the cone calorimeter fume hood, to limit leakage. The calorimeter is based on the ISO 5660-1 standard [9], with the heat release rate measured through the oxygen consumption method, using an O₂ sensor (Hummingbird, Paracube Premus- α). The total energy released during the combustion was then calculated by integrating the heat-release-rate over time. It is important to note that only the energy released by the combustion can be measured with this method. Other energy fluxes such as exothermic reactions within the cell and heat transfer with the environment are not considered. The volumetric smoke production rate was measured in the exhaust pipe of the cone calorimeter using a helium-neon laser, again following the procedure described in ISO 5660-1 [9]. The total amount of smoke was then calculated by integrating this value over time.

4.3.3 Particle size spectrometers

Two particle spectrometers were used to cover a size spectrum as wide as possible. An optical aerosol spectrometer (Grimm Aerosol Technik, Mini-LAS model 11R) focused on particles with a diameter ranging from 250 nm to 32000 nm and provided a full size distribution every 6 seconds. The sampling rate was 1.2 L/min. Smaller particles with sizes ranging from 17.5 nm to 532.8 nm were analysed using a scanning mobility particle sizer (SMPS) (TSI, model 3775-3082), sampling aerosols at 0.3 L/min and requiring 76 s to perform a complete scan. The samples drawn by both instruments were taken in a diluted probe lowering the aerosol concentration by a factor 40, to quench the reactions, prevent

aggregation and avoid detector saturation. The sampling approach is shown schematically in Figure 5, with the probe itself built from a 6 mm outer diameter brass tube with a 4 mm orifice, allowing a sampling flow rate of 0.9 L/min and positioned 15 cm above the positive pole of the cell undergoing thermal runaway. The vacuum pump had a flow rate of 36 L/min.

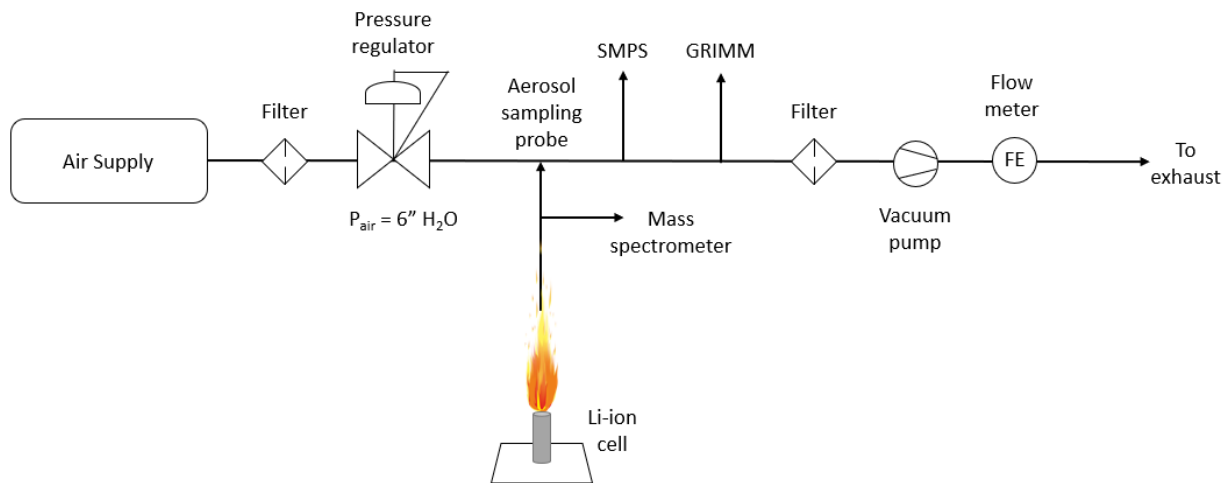


Figure 4.3: Overview of the gas sampling line

4.3.4 Mass spectrometer

The analysis of the outgassing composition was performed using a mass spectrometer (MKS Instruments, Cirrus 1 LM99). Gas samples were collected using the same nozzle as previously described for aerosol analysis (Figure 4.3) but were sent to the mass spectrometer without dilution with a flow rate of 0.2 ml/min. To minimize scan time, a limited number of molecular masses were considered to detect species of interest (m/Z ratio in parenthesis): H_2 (2), CH_4 (15; 16), DMC (15; 45), H_2O (18), HF (20), LiF (25), C_3H_6 (39; 41), CO_2 (44), C_6H_6 (78), POF_3 (85; 104). These species were selected following complete scans to identify the most relevant species and are consistent with similar choices made in the literature [15, 72-74]. This enabled a rapid scan time of 6s, with a detection limit for individual species corresponding to an ionic current of $1 \cdot 10^{-13}$ A. Prior to the tests, a calibration was performed for four species of interest (H_2 , H_2O , CO_2 and DMC) to enable the relative concentration of these species to be quantified. However, since the mixing between the cell outgassing and the surrounding atmosphere is uncontrolled and the resulting dilution ratio unknown, the absolute concentrations cannot be quantified using this approach.

4.3.5 Infrared and high-speed cameras

A high-speed multispectral infrared (IR) camera (Telops, MS M350) was used to simultaneously acquire images through 8 spectral bands or broadband attenuations over the 1.5 μm and 5.4 μm range. The maximum acquisition frequency in multispectral mode was 120 Hz (300 x 500 pixels), while up to 500 full frame images per second (640 x 524 pixels) can be acquired when a single filter position is used. This enabled calibrated thermographic measurements over the very broad temperature ranges encountered during TR, from room temperature to over 1000 °C. Moreover, the multispectral capabilities were leveraged to measure the temperature of the cell positive pole cap by using filters that had spectral wavebands designed to see through the flame (3649-3763 nm, 3773-3809 nm and 3945-3983 nm). Finally, other filters centred on the absorbance peaks of H₂O and CO₂ (2987-3038 nm and 4382-4597 nm, respectively) were used to estimate the flame temperature [91]. For these measurements, the Plexiglass enclosure was removed to maintain the camera calibration and allow optical access to the positive pole and cell casing.

A high-speed camera (Photron, Fastcam Mini AX200) was also used to capture the flame emissions in the visible spectrum, with a 50 mm lens (Nikon). This model records video at up to 6 400 full frames per second (1024 x 1024 pixels).

4.3.6 Experimental methodology

A total of 20 Li-ion cells were tested with three heating rates (5 °C/min, 10 °C/min and 20 °C/min), with an effective heating rate calculated post-hoc from measurements of the cell casing temperature. They were realized in the cone calorimeter with the four Plexiglass walls installed, combined with particle size and mass spectrometry. An additional test with the plexiglass enclosure removed and the heating setup reduced to the heating wire was performed to improve optical access and allow a better visualization of the cell outgassing and cell casing. All the tests were performed at room temperature (25 °C) and followed the same test protocol based on the DO-311A standard, with the resulting evolution of the cell casing temperature shown in Figure 4.4. The cells were initially brought to 55 °C with a heating rate of 6 °C/min. The temperature was then kept constant at 55 °C for three minutes. The desired heating rate was then applied (5 °C/min, 10 °C/min or 20 °C/min) until the first venting was observed. At this point, the heating was stopped, and the cells were left to either undergo thermal runaway or cool down. If no thermal runaway was observed following this initial heating ramp and the cell temperature decreased below 55 °C, a second heating ramp was initiated and was maintained. It is worth noting that self-heating already occurs in the cell during the initial heating ramp, but that

this does not necessarily lead to TR. Since our investigation focuses on the combustion associated with TR, this dual heating ramp protocol allowed us to observe flames for every test. In the following, cells are said to undergo spontaneous TR if a single heating ramp was required while if two heating ramps were needed the TR is referred to as non-spontaneous.

4.4 Results

4.4.1 Cell, outgassing and flame temperature

The main stages of TR are illustrated in Figure 4.4 and can be summarized as follows: (i) the security vent opens, and a small venting occurs, (ii) the temperature of the cell stabilizes or slowly increases, (iii) the temperature of the cell surges and reaches several hundred degrees Celsius, quickly followed by a major venting event accompanied by sparks and unstable flames, (iv) the gas ejection speed decreases and yields a stable flame, (v) the flame extinguishes and the cell cools down.

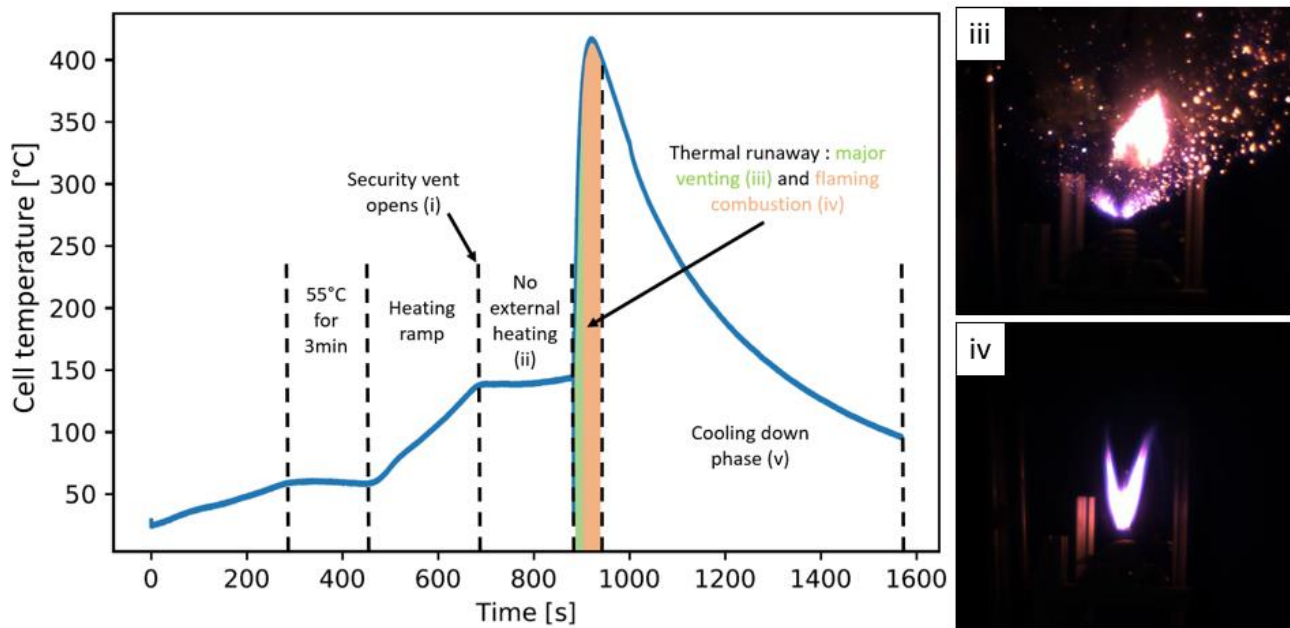


Figure 4.4: The main stages of TR

Figure 4.5 shows an example of the temperature recorded by the 4 thermocouples implemented as described in Section 4.3.1. The first venting temperature was defined as the maximum cell temperature measured by TC1 or TC2 when the security vent opens. The highest temperatures of the cell casing were recorded by these same thermocouples shortly after, typically following sharp increases associated with the major venting events. The maximum temperature of the outgassing and of the flame are recorded in the gas phase above the cell, as very short spikes when combustion occurs. However,

as the positive pole features three venting ports and cell motion occurs during venting, the temperature measured at these two discrete points does not always capture the conditions inside the vented jets and flames, as shown in Figure 4.4.

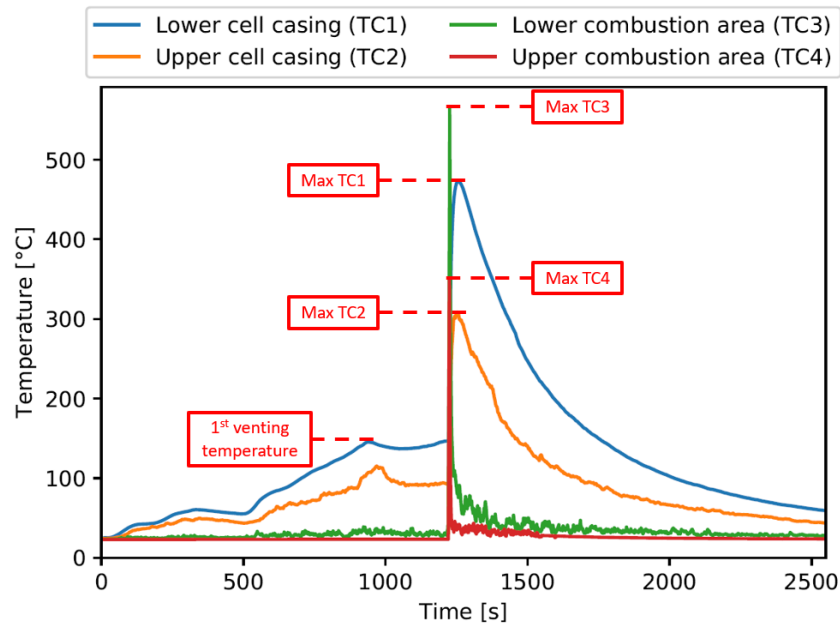


Figure 4.5: Description of the temperature measurements

The cell casing and flame temperature obtained from the multispectral infrared camera was compared against measurements from thermocouples. The use of “through flame” filters also allowed the direct measurement of the temperature of the positive pole during outgassing and combustion. Figure 4.6 shows these three areas of interest, namely the location of TC2 on the cell casing, the positive pole and the location of TC3 above the cell. For each location, the temperature reported below is the average value calculated over all pixels inside the designated area.

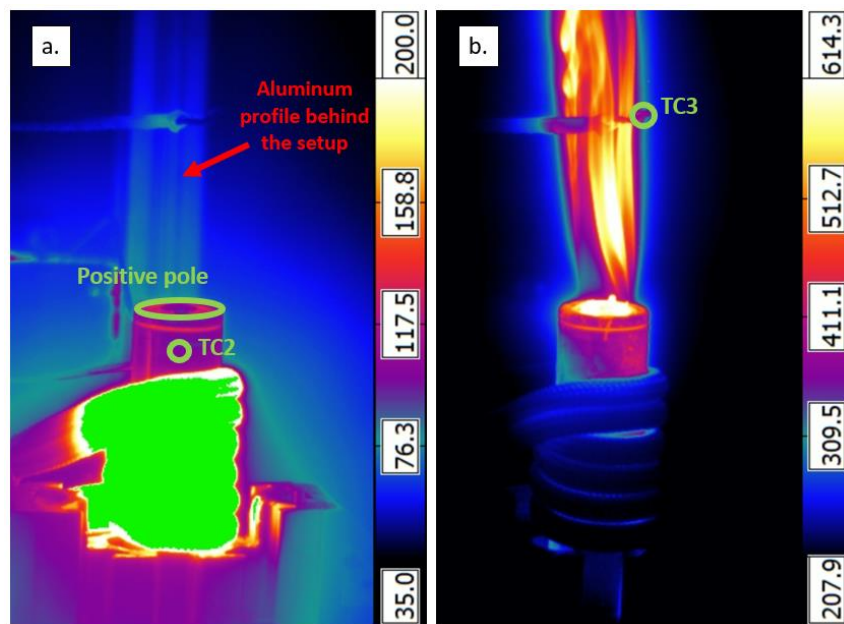


Figure 4.6: Frames extracted from high-speed infrared imaging, for an effective heating rate of $14^{\circ}\text{C}/\text{min}$. (a) Images taken just before TR when the casing temperature is 95°C and the positive pole temperature is 130°C . (b) During TR, the positive pole and outgassing temperatures are 700°C and 450°C , respectively

Figure 4.7 shows comparisons between the temperature measured with the infrared camera and the thermocouple for the cell casing and outgassing (TC2 and TC3). Infrared measurement yields a peak temperature 115°C higher for the cell casing (Figure 4.7a), demonstrating that although the thermocouple is firmly pressed against the surface, the imperfect contact still prevents the true temperature to be obtained [92, 93]. The resulting thermal inertia is easily visible in Figure 4.7a by comparing the two temperature rises at approximately 840 seconds. Moreover, the emissivity of the casing might evolve as its temperature increases and its surface undergoes physical and chemical changes. For this measurement, the emissivity of the surface was taken as 0.8 for the cell casing (cold-rolled steel [94]). For the outgassing or flame temperature, the radiometric temperature is somewhat lower, by approximately 100°C , and should be considered an estimation as the emissivity of the gas plume is unknown but assumed to be unity for the calculation. These measured outgassing and flame temperatures are relatively low at approximately 500°C for this test for which both IR and TC measurements are available. This reveals that the unknown emissivity of the gas results in large errors in radiometric temperatures and that for this particular test the thermocouple was not aligned to capture the hottest point in the flame. A more detailed representation of the range of flame temperatures measured is presented in the following section. The through-flame infrared measurement allowed a

detailed measurement of the temperature evolution of the positive pole during TR, quickly reaching 725 °C during the combustion phase (Figure 4.8). This is significantly higher than for the cell casing (see Figure 4.7a) and is a good proxy to estimate the temperature of the outgassing flow as it exits to the open atmosphere.

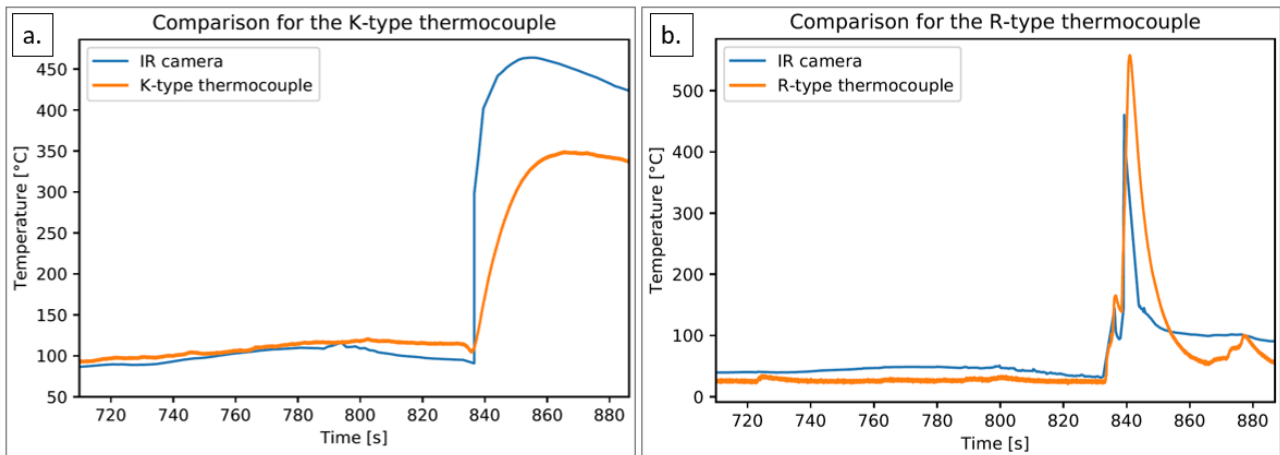


Figure 4.7: Comparisons between the infrared camera and the thermocouple measurements

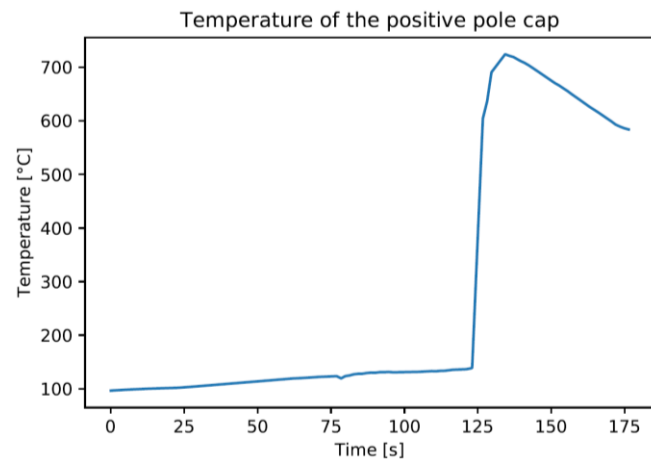


Figure 4.8: Infrared camera measurements of the positive pole temperature during combustion using a through-flame infrared filter

The IR camera also revealed phenomena not apparent in the visible spectral, as shown in Figure 4.9a, with “ t_0 ” representing the instant the security vent opens. 50 ms after t_0 , liquid ejections of electrolyte are observed, quickly followed by liquid electrolyte spilling over the positive pole of the cell and flowing along the cell casing (50 ms to 300 ms after t_0). For a few seconds (0 s to 32 s after t_0), gas ejection due to electrolyte decomposition begins and progressively increase in intensity until the major venting ($t_0 + 33$ s). This observation confirms that no combustion occurs before the major venting event. Only then incandescent particles, sparks and flammable gases are expelled from the cell. The high initial velocity prevents a diffusion flame from stabilizing, meaning that most of the material in the initial ejection remains unburned. Stable ignition is observed 35 seconds after t_0 and continues until the combustible material presents inside the cell is exhausted. The stable flaming combustion phase typically last for about 10 seconds. The last three phases described here are also shown in the visible spectrum in Figure 4.9b.

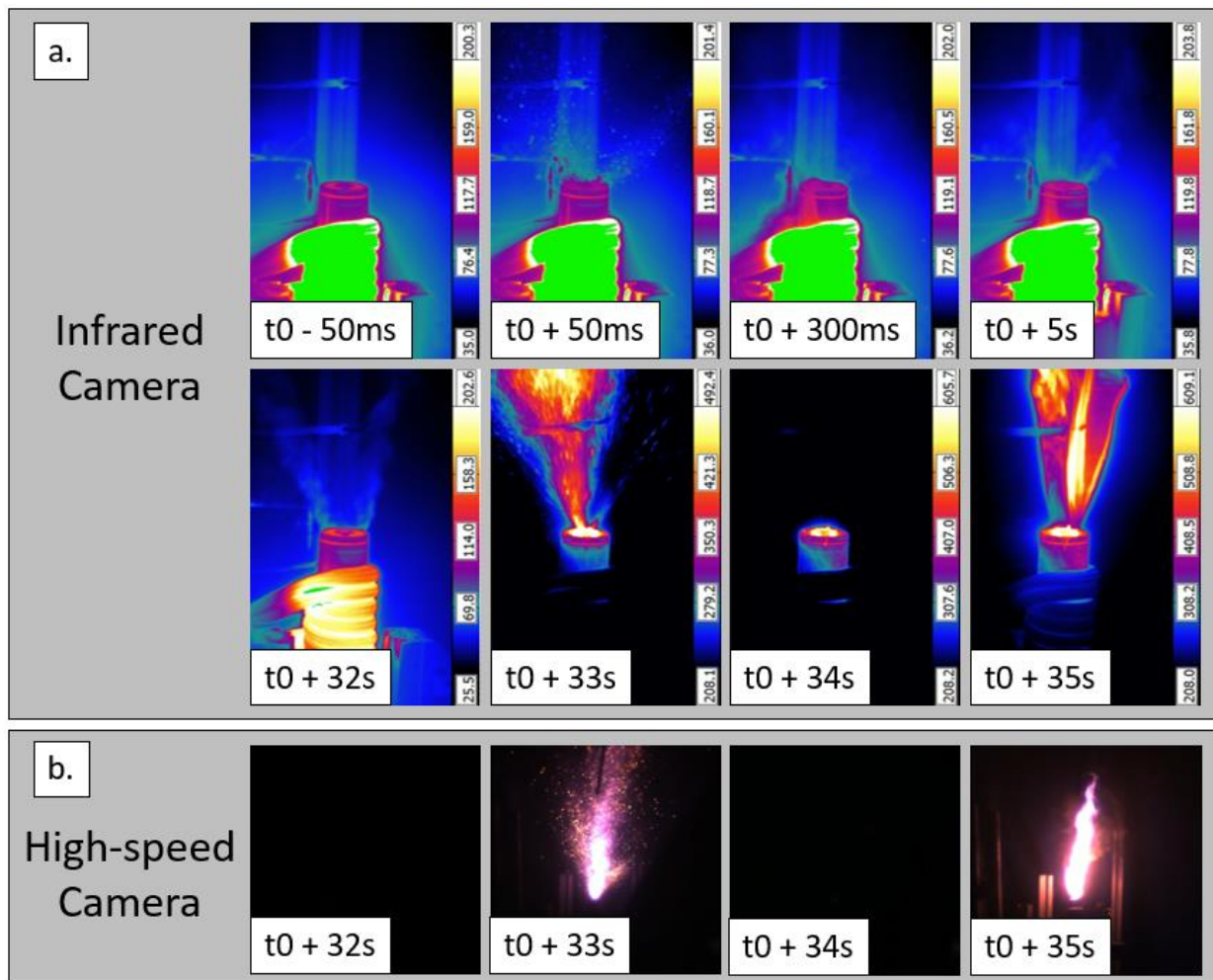


Figure 4.9: Frames extracted from infrared (a) and high-speed (b) imaging recorded during the thermal runaway of a Li-ion cell (both videos are available as supplemental material). The infrared

frames were recorded with two broadband filters that have different temperature ranges. “t0” represents the opening of the security vent

4.4.2 Effect of the heating rate

Thermal runaway was induced in cells with heating rate ranging from 5 °C/min to 20 °C/min, with simultaneous measurement of cell and outgassing temperature, as well as heat release rate (HRR) and volumetric smoke production. The weight of each cell was measured before and after each test to calculate the mass loss. The outgassing composition and particle size distribution were also measured and are presented in the following section.

As it can be seen in Figure 4.10, the spontaneity of the TR is highly affected by the heating rate. For the lowest heating rate (5 °C/min), no cells experienced a spontaneous TR while the opposite was observed for the highest heating rate (20 °C/min). For a moderate heating rate (between 10 °C/min and 14 °C/min), six out of seven cells required a second heating ramp to undergo TR. The spontaneity of the TR thus increases as the heating rate increases. The first venting temperature is also affected by the heating rate (Figure 4.8), being higher when the heating rate increases.

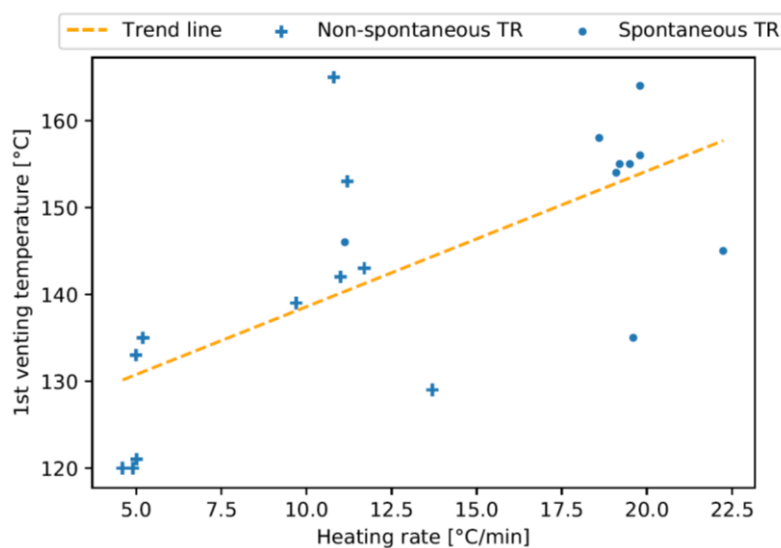


Figure 4.10: First venting temperature of the cell as a function of the heating rate

The maximum temperature reached by the cell casing (TC1 and TC2) during TR does not appear to be significantly affected by the heating rate or the spontaneity of the TR, as it can be seen in Figure 4.11a. The maximum temperature is between 375 °C and 560 °C at the bottom of the cell (TC1) and between 192 °C and 471 °C at the top (TC2). This difference can be due to several factors such as a loss of contact between TC2 and the cell, a temperature gradient between the bottom and the upper part of the

cell or convective effects in the upper part of the heating setup. The maximum temperature in the flame zone as a function of the heating rate is shown in Figure 4.11b, reaching up to 1280 °C for the measurement position closest to the cell vent (TC3). The flame temperature does not seem affected by either the heating rate or the spontaneity of the TR. Again, the large variability can be explained by the spatially discrete measurement obtained from the thermocouple, not necessarily aligned with the narrow flames escaping the three cell vents.

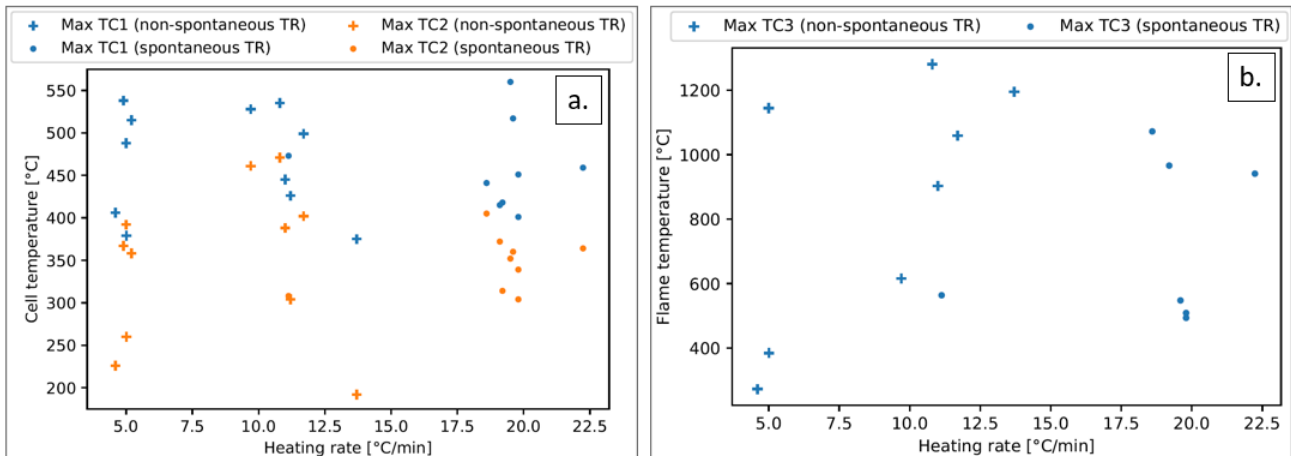


Figure 4.11: Max TC1 and Max TC2 (a), Max TC3 (b) as functions of the heating rate

The peak HRR and the total energy released are shown in Table 4.1. Both appear to be higher for cells subjected to a moderate heating rate (i.e. 10 °C/min). The cells subjected to a high heating rate (i.e. 20 °C/min), and that thus underwent spontaneous TR, seem to have relatively low peak values with a low variability for the HRR, as it can be seen with relatively small standard deviation. It is also important to note that the HRR and the total energy released during the combustion phase of the TR follow similar trends. The maximal heat release measured was up to 92 kJ, well exceeding the electrical energy stored in this type of cell (i.e. 32 kJ).

Table 4.1: Maximum heat release rate and total energy released for the different heating rates

Nominal heating rate [°C/min]	Peak heat release rate [kW]				Total energy released [kJ]			
	Mean	Minimum	Maximum	Standard deviation	Mean	Minimum	Maximum	Standard deviation
5	3.90	2.53	8.09	2.11	37.20	22.80	76.00	19.79
10	5.41	3.61	8.41	1.67	51.68	29.20	92.00	19.64
20	2.29	1.68	2.72	0.33	19.89	5.50	29.40	6.82

The peak value of the smoke production rate and the total amount of smoke produced are shown in Table 4.2. Both appear to be lowest for cells subjected to a moderate heating rate. It is worth mentioning that the maximum volume of smoke measured was up to 100 L, a very large value considering the dimensions of 18650 Li-ion cells.

Table 4.2: Maximum volumetric smoke production rate and total volume of smoke for different heating rates

Nominal heating rate [°C/min]	Peak volumetric smoke production rate [L/s]				Volume of smoke [L]			
	Mean	Minimum	Maximum	Standard deviation	Mean	Minimum	Maximum	Standard deviation
5	10.79	6.79	14.99	3.02	51.99	31.99	99.91	24.45
10	8.55	3.85	14.48	3.87	34.36	17.58	57.12	13.53
20	11.49	6.57	19.41	4.69	57.89	36.23	103.69	20.41

No significant effect of the heating rate nor the spontaneity of the TR was observed on the cell mass loss, as it can be seen in Table 4.3, with between 45 % and 70 % of the initial cell weight lost during TR. The results were highly variable, even for similar heating rates. For a heating rate of 10 °C/min, the mass losses were all above 54 %, which is higher than for lower or higher heating rates.

Table 4.3: Mass loss for different heating rates

Nominal heating rate [°C/min]	Mass loss [%]			
	Mean	Minimum	Maximum	Standard deviation
5	53.60	45.59	67.35	8.77
10	60.81	54.57	69.76	4.77
20	58.45	46.70	66.28	7.18

4.4.3 Gas emission

The mass spectrometer measurements revealed no major difference in the gas composition between spontaneous and non-spontaneous TR, apart from the timing of the outgassing, as seen in Figure 4.12. The outgassing associated with the first venting (i.e. the opening of the security vent) is detected in both cases, with CO₂ and DMC present. As the gas sample is collected after an important dilution occurred with ambient laboratory air, water vapor is also detected. However, the lack of significant shift in the H₂O concentration following the first venting indicates that combustion does not take place at this time. For spontaneous TR, the gas production continues with a slight decrease over a few minutes, until the major venting occurs. For non-spontaneous TR, the gas production follows the same trend but stops completely for 2 to 5 minutes. During the major venting event, H₂, H₂O, CO₂ and DMC were always detected. Traces of C₃H₆ were found in three tests, while LiF and C₆H₆ were found in only one test. The increased presence of water vapor is indicative of combustion while the simultaneous detection of H₂ and DMC reveals that this combustion is incomplete or that combustible gases escape before the flame establishes itself, as discussed in Section 4.4.1 dealing with the IR thermography measurements. The presence of H₂ can also be due to the reaction between water vapor and lithium [95, 96]. The main combustible species emitted appears to be the electrolyte itself, DMC, with a peak concentration reached during the first venting, prior to the apparition of flames.

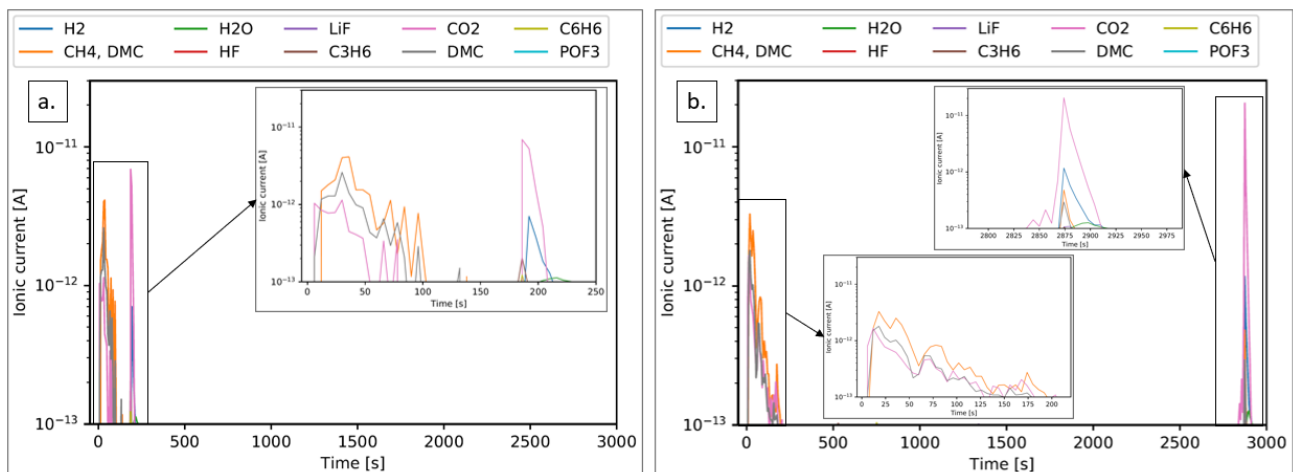


Figure 4.12: Comparison of mass spectrometry measurements between spontaneous (a) and non-spontaneous (b) TR. The first peak in both cases is associated with the initial venting without flames, while the second follows TR and combustion of the outgassing

Figure 4.13 presents the relative peak gas concentration values for the calibrated species during the first venting and the combustion following the major venting event, combining the results of all the tests, no matter the heating rate. The results confirm that the maximum concentration of DMC takes place during the first venting (Figure 4.13a), being 8 times more abundant than CO_2 , and that this outgassing is mainly due to the evaporation of the electrolyte. During the combustion following the major venting, CO_2 and H_2O are mostly detected, with small amount of H_2 and DMC (Figure 4.13b), as expected for gases sampled in a turbulent diffusion flame.

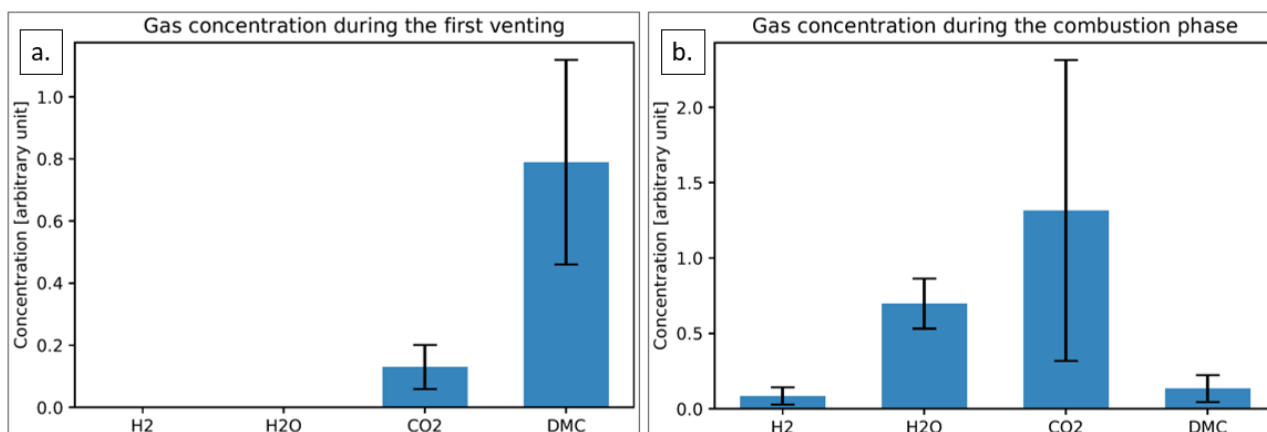


Figure 4.13: Relative gas concentration for major species after calibration, during the first venting (a) and the combustion following the major venting (b). The error bars represent standard deviations

The particle size distributions discussed below are representative of the peak concentration observed during the major venting and the flaming combustion of the outgassing. The results of all the tests, no matter the heating rate, are gathered in Figure 4.14 and Figure 4.15. Figure 4.14 shows the size distributions measured with the GRIMM by considering the number of particles (Figure 4.14a) and the mass of particles (Figure 4.14b). The majority of the particles detected have a diameter smaller than 800 nm. However, the peak concentration appears to be located below the lower size detection limit of the instruments and the size distribution is therefore incomplete (Figure 4.14a). Nevertheless, when considering the particles mass, the peak concentration is located for particles with diameters around 10 μm (Figure 4.14b), revealing that despite the important number of particles with diameters smaller than 800 nm, most of the cell mass loss by particle emission is reached with the formation of larger particles.

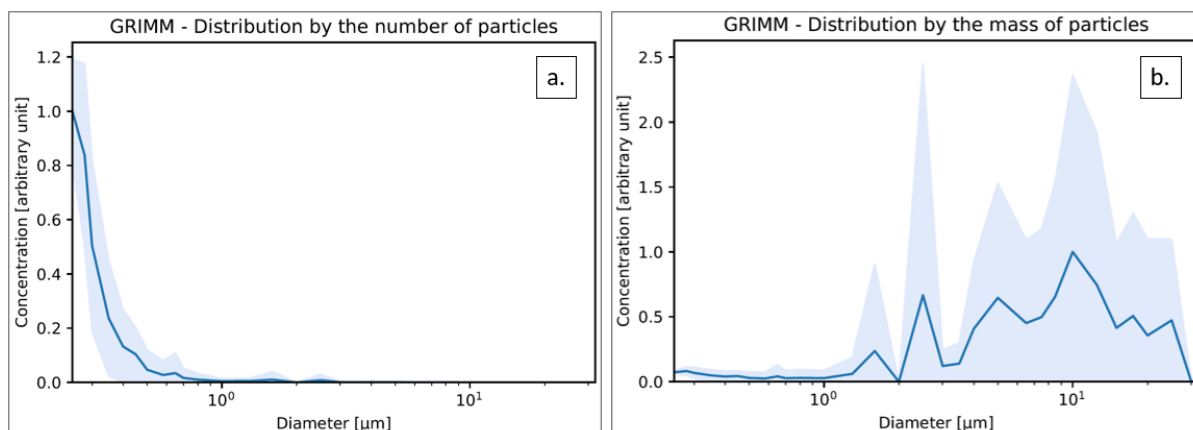


Figure 4.14: Particle size distributions measured by the number of particles (a) and by the mass of the particles (b) with the GRIMM spectrometer. The standard deviation is represented by the shaded area

The size distribution obtained from SMPS measurements appears to be bimodal, as shown in Figure 4.15a, with a first peak for particles with a diameter below 50 nm and another at approximately 125 nm. This type of bimodal distribution is common in soot formation [97]. The first peak corresponds to incipient primary particles and the second to the growth of aggregates. It is worth noting that with the SMPS measurements the first peak was not detected in all measurements and that variability between experiments was significantly higher than with the GRIMM measurements. Both observations are likely the result of the relatively long scanning time of the SMPS instrument. As the combustion associated with TR is a relatively short event, it is likely that some scans only partially capture it, resulting in a lower measured concentration of truncated size distributions. Considering the particles mass (Figure 4.15b), the concentration becomes greater when the particles diameter increases, but the peak concentration seems to be located out of the SMPS measurement range.

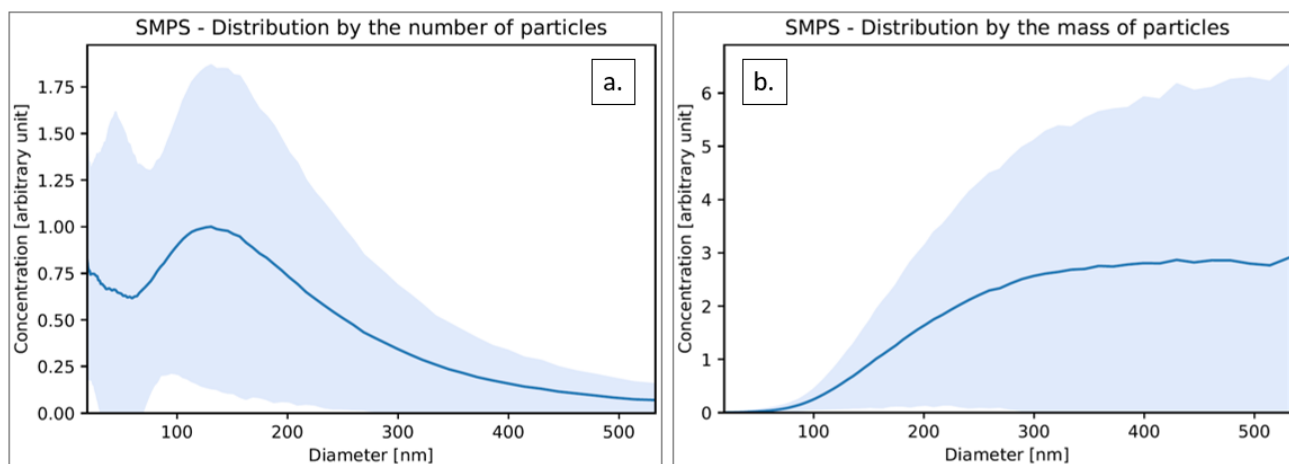


Figure 4.15: Particle size distribution measured by the number of particles (a) and by the mass of the particles (b) with the SMPS spectrometer. The standard deviation is represented by the shaded area

4.5 Discussion

Our results clearly reveal that a larger heating rate is associated with a more spontaneous onset of the TR. The first venting temperature is also observed to be higher compared to cells reaching TR slower, as it can be observed in Figure 4.10. This could be the result of the difference between the heat that can be dissipated to the environment compared to both the heat supplied and the heat generated within the cell. Faster heating rates prevent the cell from dissipating energy at a sufficient rate and this results in a more severe reaction. The heating rate is therefore highly affecting the TR course and should be considered when analysing abusive tests performed on Li-ion cells and battery such as those in the DO-311A standard. It is worth noting that when considering cascading failure in battery packs, the effective heating rates encountered are likely to be much higher than those tested here, strengthening the need to study the gas-phase combustion and its role in heat transfer to adjacent cells.

The slightly higher HRR observed for cells exposed to intermediate heating rates of approximately 10 °C/min can be linked to the duration of the major venting (phase iii on Figure 4.4). This ejection appears to be a little shorter for cells displaying high HRR and total energy release, as shown in Table 4.4. This more violent ejection is therefore associated with more fuel available for combustion in the gas phase and more energy release. However, heat release measurements might be affected by slight leakage occurring during some major venting events, as shown in Figure 4.16. Importantly, it appears that there is limited combustion during this

phase of the TR, which we attribute to the high velocity of the outgassing that prevents flame stabilization, and for the most part chemical reactions in the gas phase appear as sparks, which are well captured by the exhaust hood and therefore properly accounted in the heat release rate calculations.

Table 4.4: Major venting duration for different heating rates

Heating rate [$^{\circ}\text{C}/\text{min}$]	Major venting duration [s]			
	Mean	Minimum	Maximum	Standard deviation
5	2.18	0.87	2.93	0.85
10	0.93	0.64	1.37	0.23
20	2.03	0.92	3.12	0.78

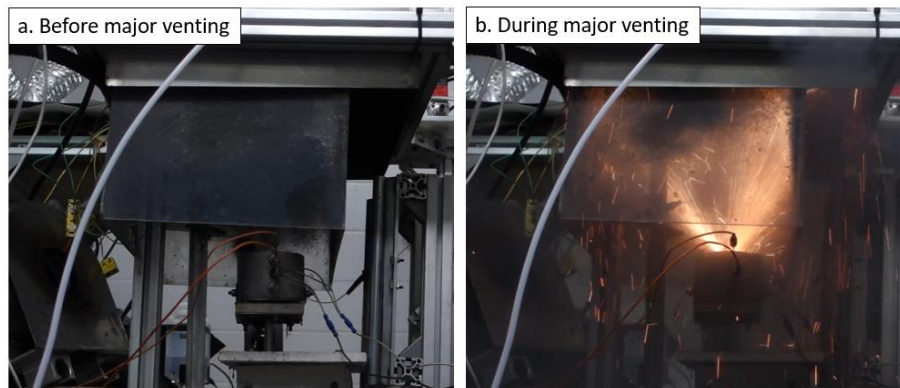


Figure 4.16: Comparison before (a) and during (b) the major venting of the TR

The use of high-speed multi-spectral infrared thermography allowed flame and cell temperatures to be obtained by two independent measurement techniques. Comparison between the two revealed the magnitudes of the uncertainties associated with the dry contact between the thermocouples and the cell casing. The unknown emissivity in the gas phase prevented the acquisition of precise temperature measurements in the flame. The direct measurement of the positive pole temperature using through-flame filters allowed a reliable value to be obtained for the outgassing temperature prior to and during the combustion phase of the TR. Moreover, a precise visualization of the first venting confirmed that no combustion occurs during this phase.

To improve repeatability between tests, the positive pole cap was removed prior to TR initiation for a few cells. By allowing a vertical outgassing and flame, probe positioning was easier. A similar approach was implemented by Mao *et al.* [98] but we did not follow through with this idea as the outgassing failed to ignite. It seems that the narrow vents in the positive pole cap

play an important role in the gas ignition by increasing its temperature and creating sparks by friction during the major venting event.

The measured total smoke production rates obtained through laser obscuration appeared to be minimal for intermediate heating rates. This result, together with the fact that heat release and mass loss are greater for intermediate heating rates, supports the hypothesis that better combustion takes place. Smoke production measurements are rarely available for TR experiments, but as electrical energy storage becomes more prevalent in transportation systems, occupant safety considerations must cover exposure to particulate matter. The total smoke produced was on the order of 50 L, with peak production rates reaching 11 L/s. Although, these results might also be affected by the smoke leak described earlier. The results provided for the particle size distribution cover the full size distribution and reveal a bi-modality typical of fuel-rich combustion processes where both soot nucleation and aggregation processes are present. Particle size playing a key role in human health and environmental effects [99], this microstructure information is of great interest and can contribute to the better design of risk mitigation approaches.

The mass spectrometry measurements provided a glimpse of the temporal variation of the concentration of the main species present in the initial outgassing and during the combustion phase. Considering the short duration of these events and the complexity of the gas mixtures released, these results are however incomplete. Moreover, CO cannot be detected using this technique as its mass coincides with that of nitrogen, with the unknown dilution with laboratory air also preventing quantitative concentration measurements. The instrument calibration however allowed the relative concentrations of H₂, H₂O, CO₂ and DMC to be estimated, revealing the abundance of DMC during the first venting and a mixture of H₂O and CO₂ during the combustion phase. Mass spectrometry and particle size distribution results are a valuable addition to the literature that can be useful to guide the design and provide validation for numerical models of the gas phase combustion associated with Li-Ion cells TR.

4.6 Conclusion

The combustion associated with the thermal runaway of 18650 Li-ion cells was investigated using a cone calorimeter, with a focus on the effects of heating rate. In addition to the heat release and cell temperature, gas-phase measurements were implemented to obtain the

outgassing and flame temperature, as well as the outgassing composition, smoke production and particle size distribution following combustion.

The heating rate had a significant impact on the spontaneity of the thermal runaway, with high heating rates associated with spontaneous onset and higher cell temperatures at the first venting. However, maximum cell and outgassing temperatures did not seem affected by the heating rate. Intermediate heating rates (i.e. approximately 10°C/min) have produced the maximum heat release and the minimum smoke production. Multispectral infrared imaging was used to obtain the temperature of the vents on the positive pole prior to and during combustion, revealing outgassing temperatures exceeding 700 °C.

Time-resolved mass spectrometry measurements allowed the identification of the main gas species released during thermal runaway. The electrolyte DMC and a small quantity of CO₂ are released during the first venting, followed by CO₂ and H₂O as well as small quantities or traces of H₂, DMC, C₃H₆, LiF and C₆H₆ during the combustion following the major venting event. The analysis of the particulate matter emitted during combustion revealed a bimodal distribution, typical of turbulent fuel-rich diffusion flames where both soot nucleation and aggregative growth are present.

CHAPTER 5 AGEING EFFECTS

5.1 Design of experiment

The results presented in this chapter aimed to study the effects of both the heating rate and the cell ageing, including measurements of gas composition and particle size distribution in the outgassing during the thermal runaway of 18650 Li-ion cells. Part of the data collected is included in the scientific article presented in Chapter 4, with results specific to the effect of ageing presented here.

Table 5.1 gives an overview of the tests that were performed. Three types of ageing (calendar, cyclic or none) and three heating rates (5 °C/min, 10 °C/min and 20 °C/min) were considered. A total of 12 aged cells were available for those tests, thus a maximum of 4 tests could be conducted for each ageing type, limiting the parameter range and interactions that could be investigated. The capacity loss (CL) is correlated with the ageing, being between 1 % and 4 % for fresh cells, between 5 % and 6 % for those subjected to calendar ageing and between 10 % and 12 % for those subjected to cyclic ageing. The column “Spontaneous TR?” indicates if the thermal runaway of the cell appeared spontaneously after the first heating ramp or if a second heating cycle was required.

Table 5.1: Overview of the experiments

Cell number	Ageing type	Capacity loss [%]	Heating rate [°C/min]	Spontaneous TR ?
19	Calendar	6	5,54	No
23		6	11,92	Yes
18		5	7,8	No
26		6	23,62	Yes
16	Cyclic	12	5,57	No
20		12	10,33	No
22		10	12,24	No
24		11	22,35	Yes
15	None	1	5,01	No
17		2	8,89	No
21		4	11,13	Yes
25		3	22,24	Yes

5.2 Results and discussion

5.2.1 Temperatures

The cell temperature at the onset of the first venting is presented in Figure 5.1 as a function of CL. This temperature is defined as the highest temperature measured between TC1 and TC2 when the security vent opens. It appears that there is no clear correlation between cell temperature at first venting and the CL. At 20 °C/min, the temperature appears to be higher for the cells that underwent calendar ageing (CL between 5 % and 6 %) while no clear trend is visible for the other heating rates. It appears that the cells that experienced a spontaneous thermal runaway have higher cell temperature at first venting, regardless of the ageing type. This tendency was previously identified in Section 4.4.2 as a consequence of the increased heating rate. Considering the limited number of cells tested for the results presented here, further investigations are required to validate those observations.

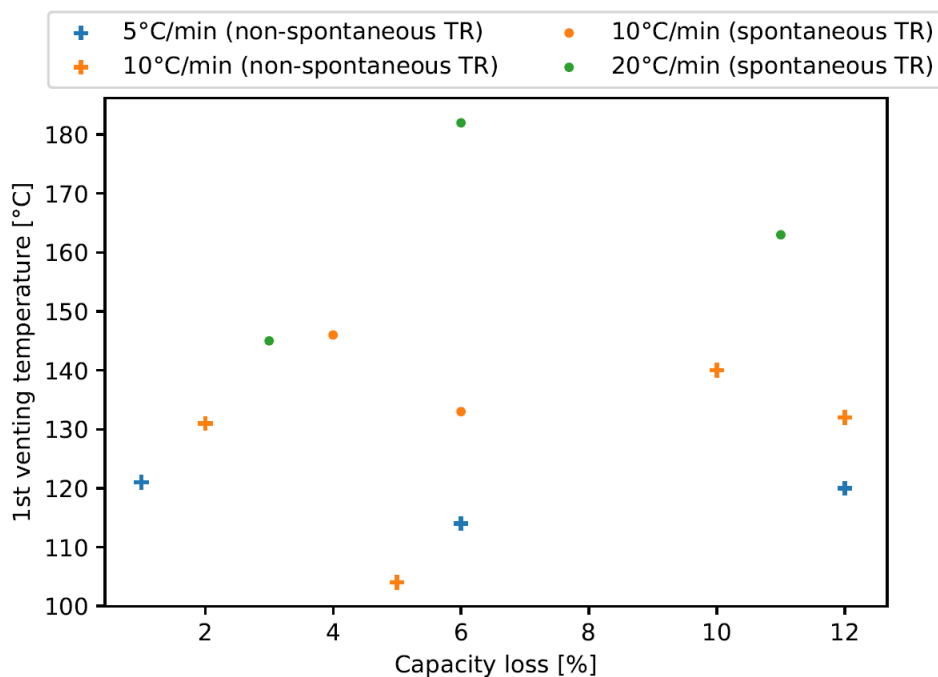


Figure 5.1: Cell temperature at first venting as a function of CL

The maximum cell temperature measured by TC1 and TC2 as a function of CL is shown in Figure 5.2. No clear trend is visible for the temperature measured next to the negative pole of the cell by TC1. However, the temperatures measured around the positive pole by TC2 appear to be higher for cells subjected to calendar ageing (CL between 5 % and 6 %). Nevertheless, a test campaign with more cells is again required to confirm this observation.

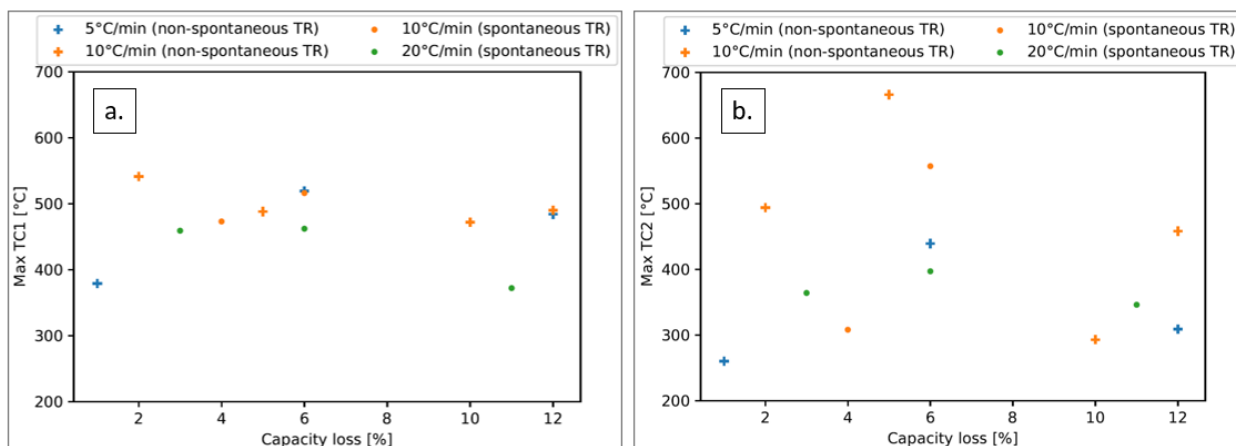


Figure 5.2: Maximum temperatures measured by TC1 (a) and TC2 (b) as functions of CL

The maximum temperatures measured by TC3 and TC4, corresponding to the flame temperature, as a function of CL are shown in Figure 5.3. No clear tendency could be extracted from these results. This variability is most likely the result of the flame position as it depends on whether or not the flame touched the thermocouple during the test.

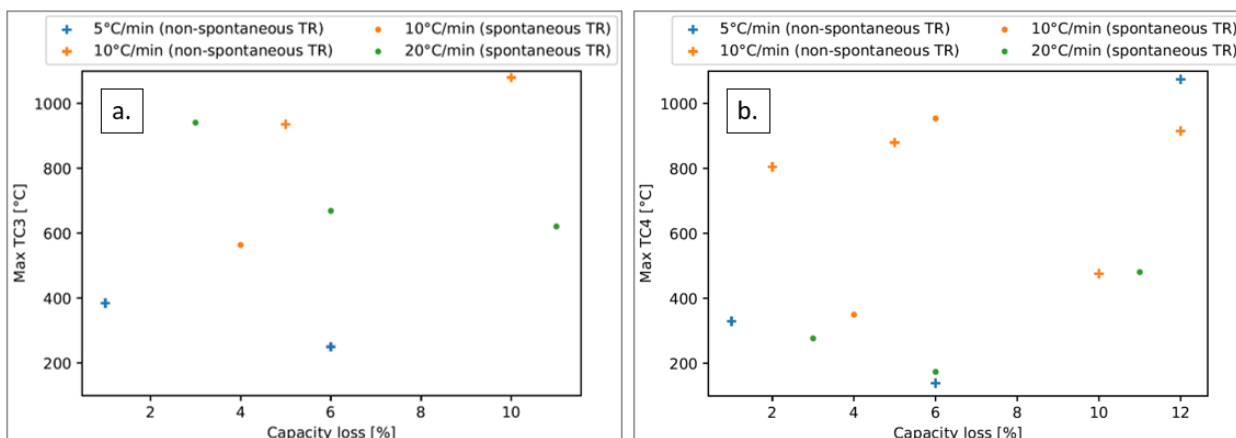


Figure 5.3: Maximum temperatures measured by TC3 (a) and TC4 (b) as functions of CL

5.2.2 Heat release rate and total energy released

The maximum heat release rate and total energy released as a function of CL are presented in Figure 5.4. It appears that these two values are slightly lower for cells subjected to calendar ageing (CL between 5 % and 6 %), as it can be seen for heating rates of 5 °C/min and 20 °C/min. Two tests provide high values of HRR at approximately 8 kW. This might be caused by the smoke leak around the exhaust chimney that affected the repeatability between the tests, as HRR measurement strongly depends on the amount of combustion gas mixture collected by the cone calorimeter. This issue will be more extensively discussed in Section 8.1.

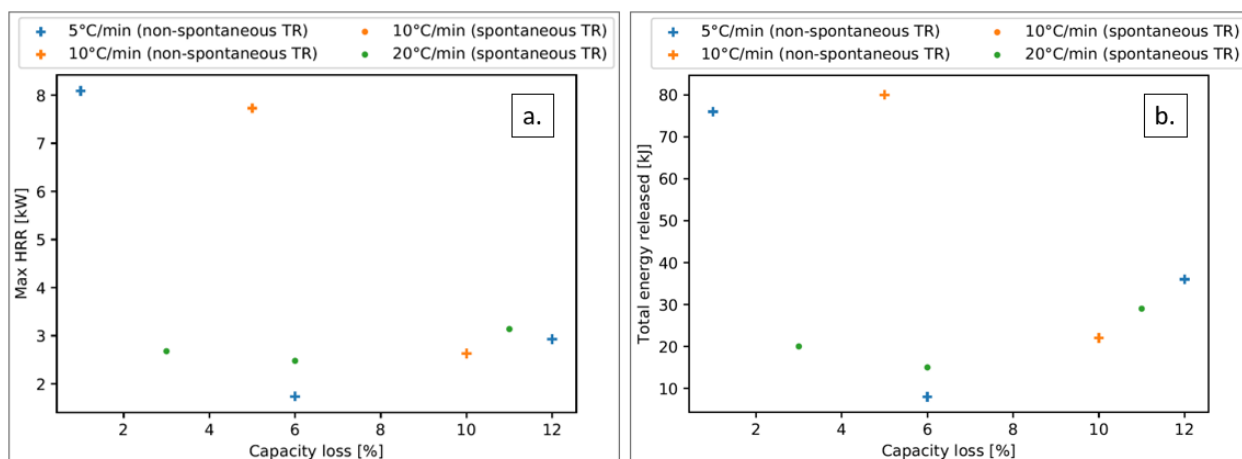


Figure 5.4: Maximum HRR (a) and total energy released (b) during the thermal runaway as functions of CL

CHAPTER 6 MODELLING

6.1 0D simulation

A sample of results of the simulation is presented in the following to illustrate its capabilities. The initial temperature is set at 600 °C (approximately the temperature of the cell casing during the outgassing) and the initial gas composition is chosen to match with previous experimental results given by Safran (CO₂: 0.32720 mol; CO: 0.12614 mol; CH₄: 0.01600 mol; NO: 0.00050 mol; NO₂: 0.00004 mol; C₂H₂: 0.01717 mol; C₂H₄: 0.00153 mol; CH₂O: 0.00019 mol; H₂: 0.02515 mol). It is important to note that this composition was observed by Fourier-transform infrared spectroscopy (FTIR) and that combustion events might have happened prior to the gas sampling. Three values for the fuel-air equivalence ratios are chosen ($\Phi = 0.5, 1$ and 2) to illustrate the behaviour of lean, stoichiometric, and rich flames. The environment pressure is set at one atmosphere.

Figure 6.1 shows examples of the gas compositions for different values of fuel-air equivalence ratios (Φ). The gas species plotted can be any of the 53 considered in the GRI-Mech 3.0 mechanism, with major species shown here. Unsurprisingly, the equivalence ratio has a strong impact on the molar fraction of CO₂ and CO present at equilibrium. The proportion of CO after the combustion becomes more important when Φ increases, and the production of CO₂ is more important when Φ decreases.

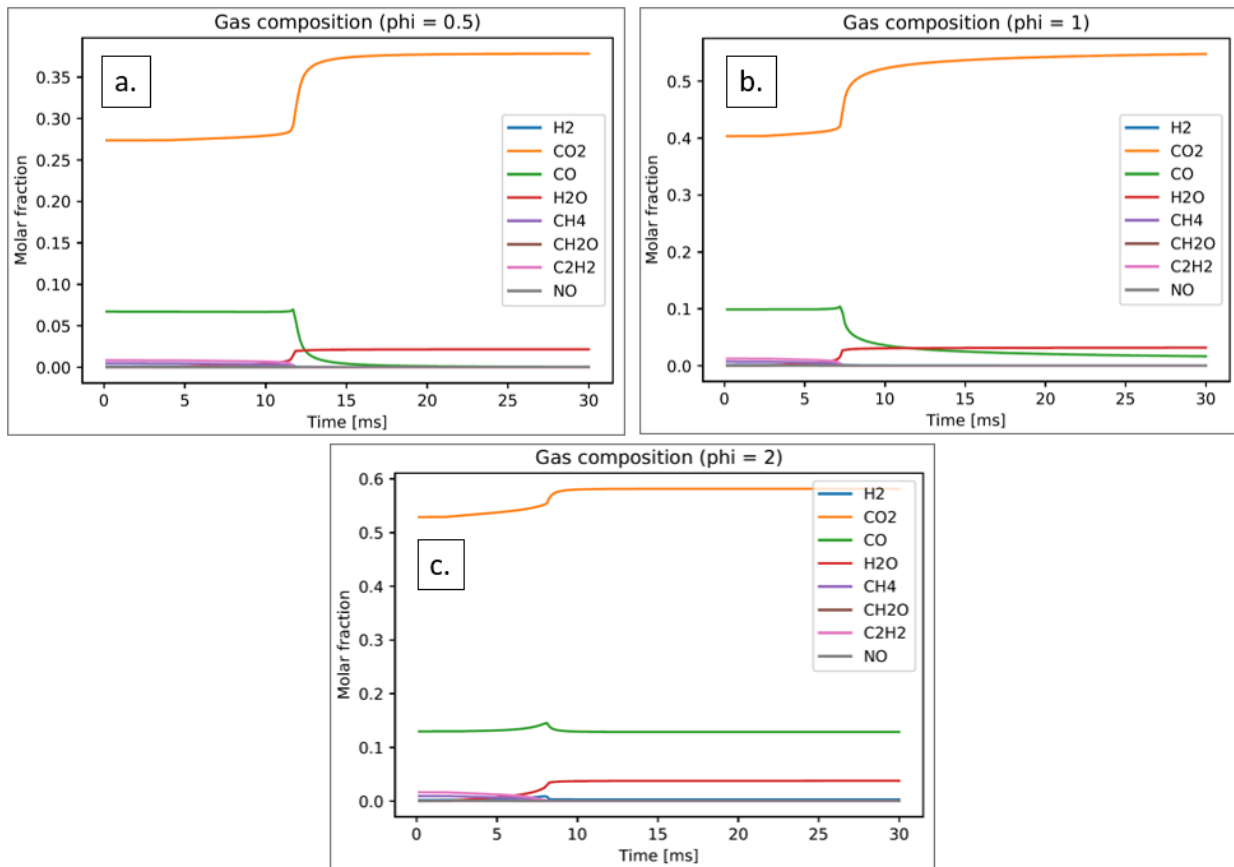


Figure 6.1: Gas composition as a function of time for $\Phi = 0.5$ (a), $\Phi = 1$ (b) and $\Phi = 2$ (c)

Temperature profiles as a function of time for the different values of Φ are plotted in Figure 6.2. As expected, the temperature is maximal for complete combustion ($\Phi = 1$) and reaches approximately 1600 °C. As a comparison, the maximum temperature measured experimentally was approximately 1100 °C. In the thermal runaway experiments, the combustion is incomplete because the flammable gas mixture is released in a quiescent air atmosphere, and mixing is therefore imperfect. Thus, the flame is non-premixed and equivalence ratio value changes depending on the location in the flame. The simulation shows that the temperature is strongly affected by the equivalence ratio and decreases rapidly as the equivalence ratio deviates from unity, explaining that the temperature measured experimentally is lower than 1600 °C. This difference between experimental and simulated results can also be due to the radiation losses on the thermocouple surface. Indeed, no radiation correction for the thermocouple measurements has been done in this project. It also seems that the time to ignition (ignition delay) of the gas mixture becomes longer as Φ decreases.

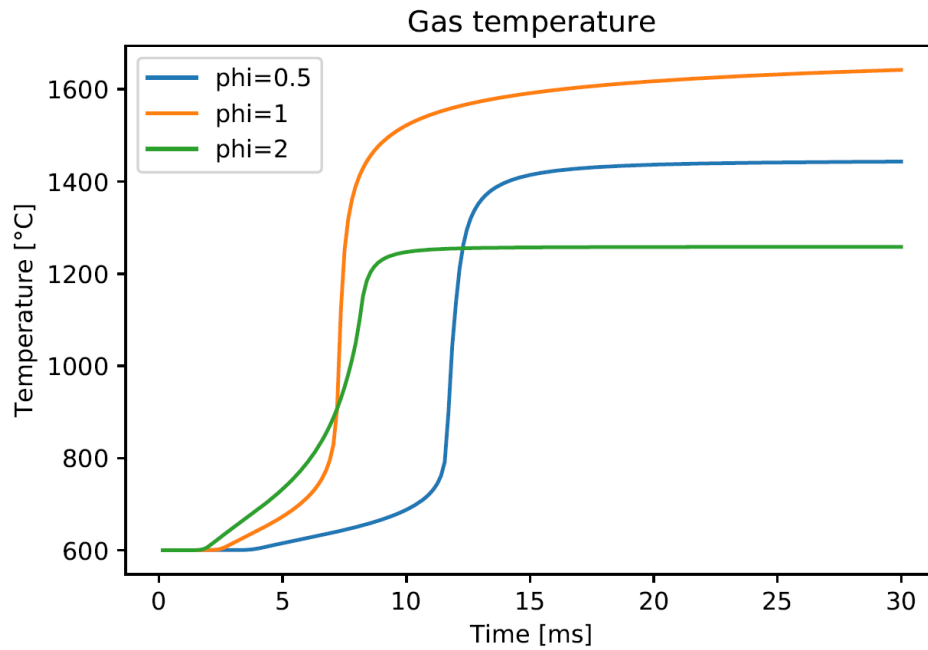


Figure 6.2: Temperatures profiles over time for different fuel-air equivalence ratios

Figure 6.3 shows the absolute values of enthalpy of combustion for the three equivalence rates considered. This value is expressed in kilojoules per kilomoles of gas mixture released during the thermal runaway. As expected, more energy can be converted to heat for the complete combustion case ($\Phi = 1$). Nevertheless, no comparison with the experimental results can be done because the gas composition values measured by the mass spectrometer are not sufficiently precise.

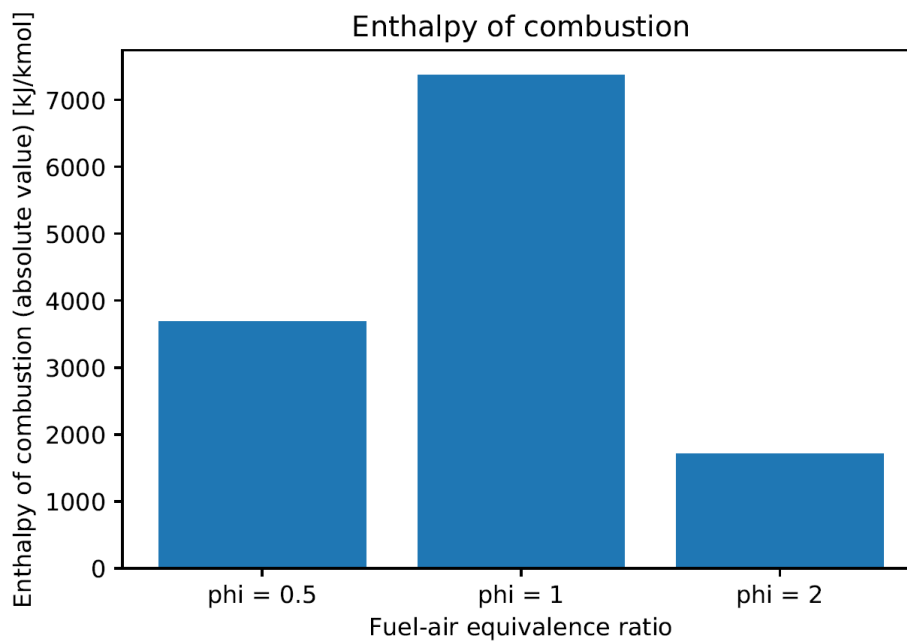


Figure 6.3: Enthalpy of combustion for different fuel-air equivalence ratios

6.2 1D simulations

6.2.1 Counterflow diffusion flame

The counterflow diffusion flame configuration considers two axisymmetric inlets with opposed flows. To achieve representative values for the momentum fluxes directed at the reaction zone, the envelope surface of the flame estimated from high-speed videos was used as the area of the fuel inlet. For simplicity, the flame was considered to be a cylinder 2 cm in diameter (2-3.5 cm experimentally) with a height of 15 cm (14-17 cm experimentally). It is important to note that this simulation does not provide any geometrical value of the flame shape. Indeed, although a flame with this configuration could be realized in practice, the simulation is far from the flame observed in our ignition tests and any interpretation in terms of flame position is not possible with such a simple model. Therefore, the results that will be presented and discussed are the flame temperature, the flame structure, and the heat release rate peak value.

The following results consider these parameters: fuel temperature = 600 °C; air temperature = 25 °C; air mass flow rate per unit area = 0.500 kg/(m².s); fuel mass flow rate per unit area = 1.043 kg/(m².s); distance between the two inlets = 20 cm; environment pressure = 1 atm. The fuel gas composition is based on experimental data from Safran (CO₂: 0.32720 mol; CO: 0.12614 mol; CH₄: 0.01600 mol; NO: 0.00050 mol; NO₂: 0.00004 mol; C₂H₂: 0.01717 mol; C₂H₄: 0.00153 mol; CH₂O: 0.00019 mol; H₂: 0.02515 mol).

Figure 6.4 shows the temperature as a function of the distance from the fuel inlet. The reaction zone is located approximately 15 cm from the fuel inlet and the maximum temperature reaches 1330 °C. This temperature value is not far from the maximum temperature measured experimentally (1280 °C). The difference can be due to the location of the thermocouple in the flame and to radiation losses that are not accounted for on the thermocouple surface.

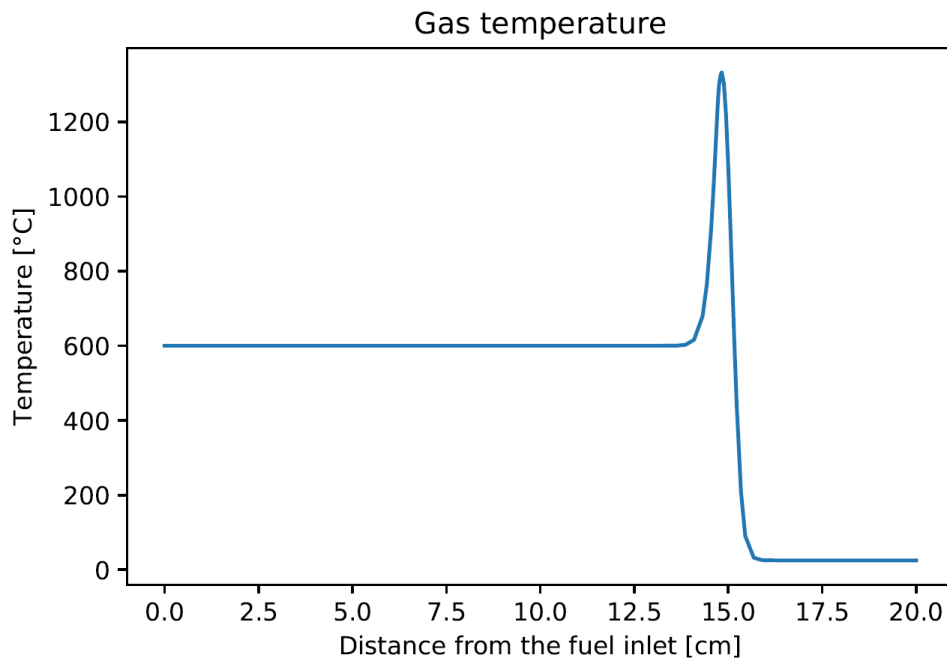


Figure 6.4: Gas temperature as a function of the distance from the fuel inlet

Gas composition as a function of the distance from the inlet (i.e. the flame structure) is presented in Figure 6.5. The gas composition at the fuel inlet (i.e. on the left of the graph) is mostly CO_2 and CO while the oxidizer gas (i.e. on the right of the graph) is air. Chemical reactions take place in the flame at 15 cm from the security vent, a value not linked to the approximation used for the flame envelope surface calculation.

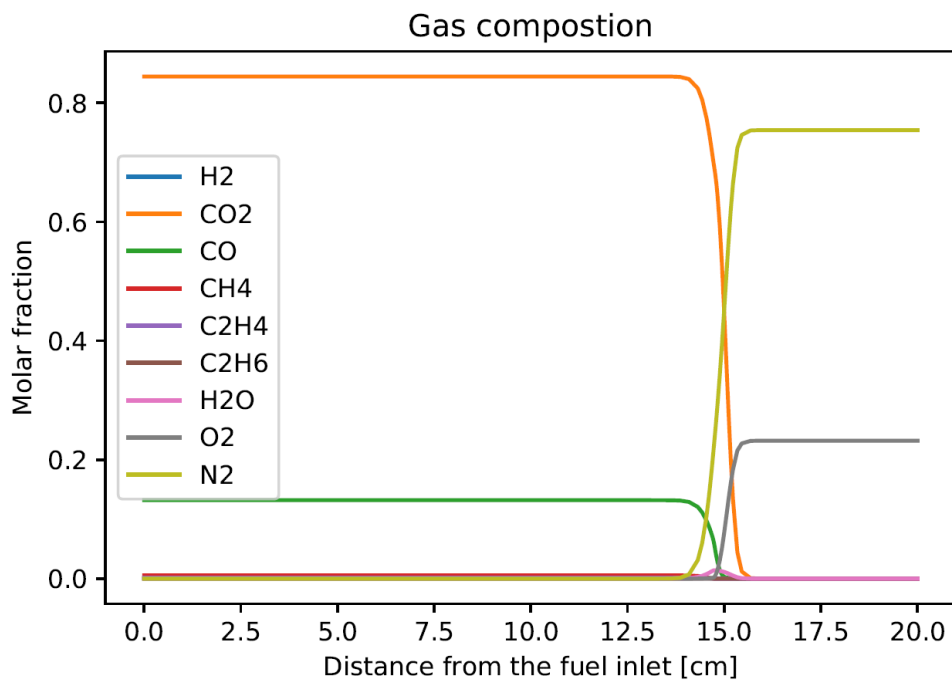


Figure 6.5: Gas composition as a function of the distance from the fuel inlet

Figure 6.6 shows the volumetric heat release rate as a function of the distance from the fuel inlet. The peak value again represents the flame position. This value is expressed in kilowatts per volume of flame (in other words, volume of gas that is reacting). By integrating the volumetric heat release rate over the spatial domain, thus capturing the thermal power released by the flame per unit area over its thickness, and by multiplying this value with the envelope surface of the flame (i.e. a cylinder of 2 cm diameter with a height of 15 cm), a peak value of the heat release rate during the combustion can be calculated. In this example, the heat release rate peak value is 8.3 kW. This value is coherent with the experimental measurement. Indeed, the measurements were included between 8.6 kW and 9 kW for the three tests at 10 °C/min with the chimney mounted around the setup.

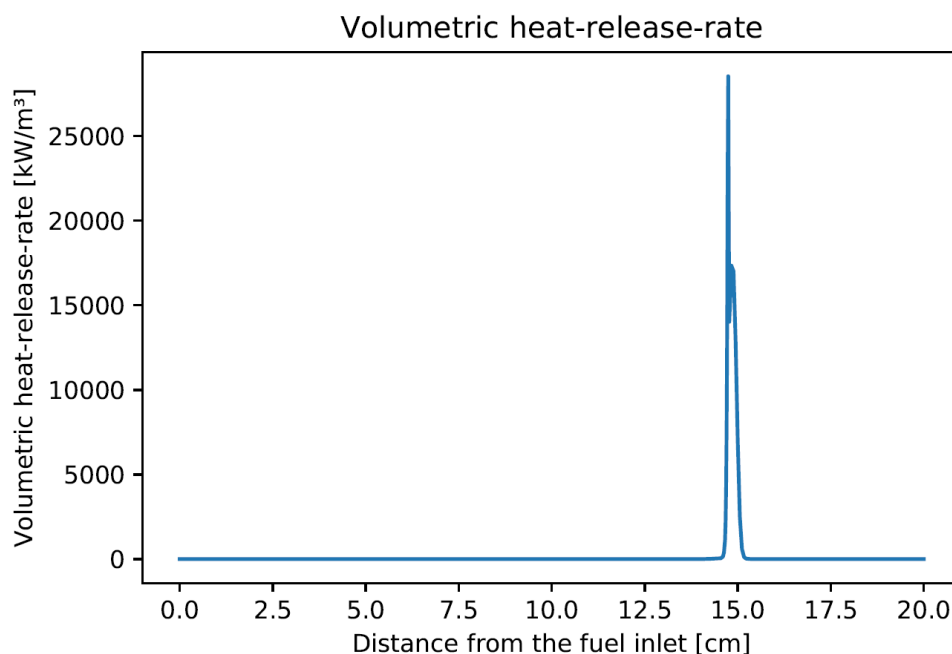


Figure 6.6: Volumetric heat release rate as a function of the distance from the fuel inlet

6.2.2 Premixed flame

The premixed flat flame model considers a homogeneous mixture of fuel and oxidizer flowing through a porous burner to create a stabilized flat flame. This model cannot be used to simulate the thermal runaway combustion of an isolated single cell. Indeed, in such a configuration, the flow of gas emitted by the cell is not directly mixed with air and there is no inlet to redirect the gas flow and to create a flat flame. However, this model is implemented to simulate a thermal runaway that could take place inside a battery module. In this configuration, the gas emitted during thermal runaway could mix with the air circulated inside the module with the porous

material representing a module outlet or vent. An external heating source (i.e. fire or spark) would in this case be required to ignite the gas mixture and create a flat flame.

For the results presented here, the simulation has been run with the following parameters: gas mixture temperature = 800 °C; mass flow rate per unit area = 103.138 kg/(m².s); $\Phi = 0.5$; spatial domain width = 40 cm; environment pressure = 1 atm. The fuel composition is again obtained from experimental data. The mass flow rate per unit area considers the thermal runaway of one Li-ion cell and a security vent with a surface corresponding to the security vent of the cell (i.e. disk of diameter 9 mm).

Gas temperature as a function of the distance from the burner face is presented in Figure 6.7. The flat flame is located at approximately 12.5 cm from the inlet and the temperature reaches values over 1400 °C at 40 cm from the inlet.

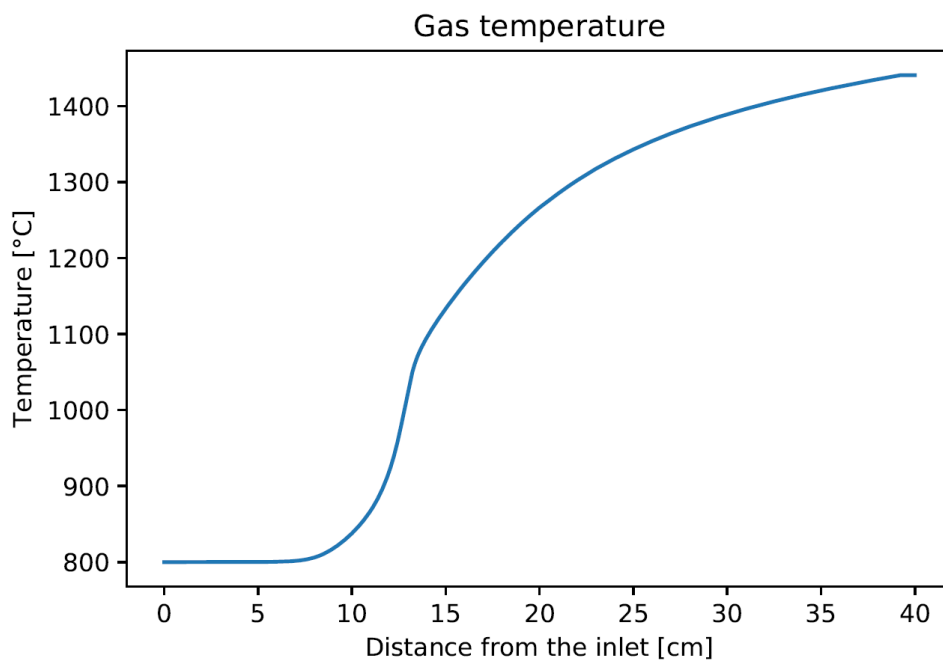


Figure 6.7: Gas temperature as a function of the distance from the inlet

Figure 6.8 shows the gas composition as a function of the distance from the inlet. Chemical reactions begin to take place 12.5 cm from the inlet but continue with a lower intensity until the maximum temperature is reached. The proportions of CO₂ and H₂O increase while the proportion of CO and hydrocarbons decreases. Concentrations of other minor gas species are very low upstream and downstream the flame.

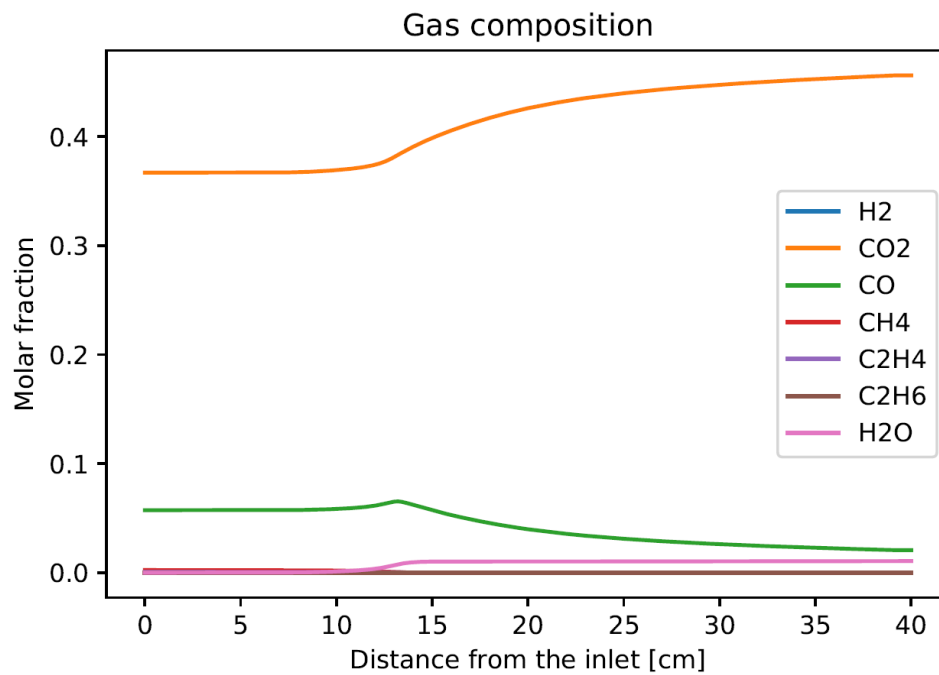


Figure 6.8: Gas composition as a function of the distance from the inlet

Volumetric heat release rate as a function of the distance from the inlet is plotted in Figure 6.9. This value is expressed in kilowatts per unit volume of flame. The peak value is reached close to the burner face, shortly after the chemical reactions are initiated. As previously mentioned for the counterflow diffusion flame, the heat release rate peak value can be calculated from this profile. In this configuration, a peak value of 14.1 kW is obtained from the simulation. Nevertheless, since the configuration of this model does not represent the experimental setup, there is no experimental value to validate this result.

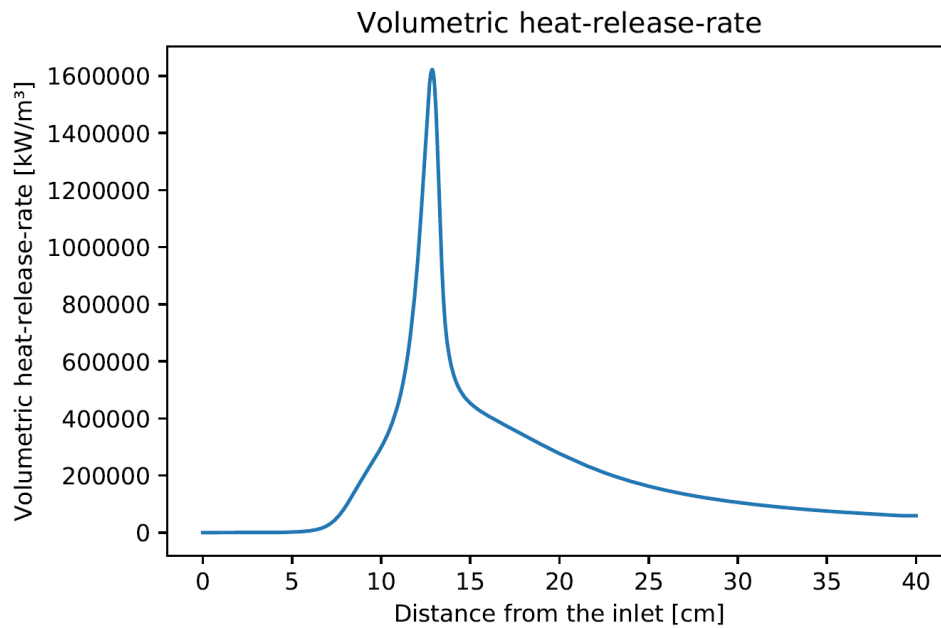


Figure 6.9: Volumetric heat release rate as a function of the distance from the inlet

6.3 Critical analysis

As previously mentioned, these three simulations are very simple compared to reality and are a first step toward more complex work. Nevertheless, results such as gas temperature, gas composition and heat release rate are of the same order of magnitude as experimental data and can be used to assist in the interpretation of experiments, especially to understand the effect of critical parameters. In the following, key simplifications that had to be implemented are explained and discussed.

The three simulations are implemented on Cantera using the GRI-Mech 3.0 mechanism. This mechanism is largely used to simulate the combustion of light hydrocarbons such as propane and methane. Therefore, several gas species released during the thermal runaway of Li-ion cells such as hydrogen fluoride (HF), hydrogen chloride (HCl), dimethyl carbonate (DMC), ethylene carbonate (EC) and propylene carbonate (PC) are not considered. In particular, dimethyl carbonate is one of the three major species (with CO_2 and CO) released during thermal runaway and has a high energy content. Therefore, it may influence the results of the simulation, especially in terms of total energy released.

The 0D simulation is the simplest of the three but is still useful to have approximations of gas temperature and composition. The major uncertainty is the fuel-air equivalence ratio. Indeed, there is no proper way to obtain this value experimentally, as it depends strongly on the

geometrical and flow configurations. Nevertheless, this model is a great tool to know the exhaust gas composition.

The 1D counterflow diffusion flat flame is a more realistic configuration that allows the investigation of complete combustion, while avoiding the difficulty of having to choose an equivalence ratio. The model requires a mass flow rate of air to calculate the equilibrium between the two inlets and to create the flat flame, but this is not the case in reality for our experiment where the thermal runaway takes place in a quiescent atmosphere. Because of this, it is not possible to predict the shape of the flame with this simulation.

As previously mentioned, the 1D premixed flat flame is not representative of a Li-ion cell thermal runaway. Indeed, in reality the gas mixture released by the cell is not homogeneously mixed with the air and no specific inlet is present to redirect the gas flow and to create a flat flame. Nevertheless, in case of a battery module design that would allow air to be mixed with the outgassing prior to combustion, the simulation yields interesting results such as the laminar flame speed and flame temperature, but this could not be verified in this project.

CHAPTER 7 GENERAL DISCUSSION

The experimental setup can be improved to concentrate and decrease the amount of smoke that escapes the exhaust of the cone calorimeter during the major venting. To investigate this issue, three TR tests were performed with a stainless-steel chimney mounted around the heating setup, allowing the cell outgassing to be captured more efficiently by the cone calorimeter. HRR was strongly impacted by the smoke leak (Figure 7.1a), doubling the mean value of the measurements and highly improving the repeatability as shown by the decreased standard deviation. However, the smoke production measurements did not seem significantly affected by the presence of the chimney (Figure 7.1b). Surprisingly, the measurements with the chimney mounted revealed a slight decreased of smoke production rate. Such a configuration, although preventing visualization of the thermal runaway, could therefore improve the calorimetry measurements in future work.

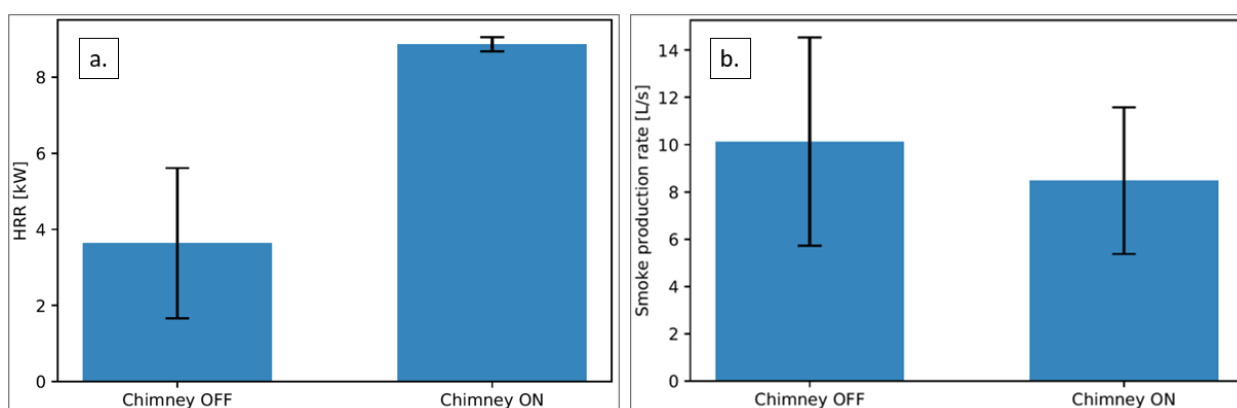


Figure 7.1: Comparison with or without the chimney for: (a) HRR and (b) smoke production rate. Uncertainties are represented as standard deviations

Several points for improving the results presented in this work can be highlighted. The number of tests was limited due to their relatively long overall duration, which is a concern for a phenomenon as random and unsteady as the thermal runaway. This prevented definitive conclusions and further work is required to validate the results gathered in this work. Repeatability was not studied and could be interesting to investigate in a forthcoming work since the thermal runaway of Li-ion cells is highly variable under certain conditions. The situation becomes even more complicated due to the two types of thermal runaway observed in this project: spontaneous and non-spontaneous. Indeed, as observed in the mass spectrometry results, internal reactions in the Li-ion cell are taking place between the two heating ramps when thermal runaway does not occur spontaneously. This must influence the behaviour of the

cell during the combustion phase and the comparison between the two types of thermal runaway may be improved by further studies. Also, the cone calorimeter only allowed the measurement of the heat released associated with the combustion of the outgassing, other forms of energy such as what is released through electrical effects were therefore neglected.

This work demonstrated that the use of a multispectral infrared camera can significantly improve the temperature measurements of both the cell casing and the outgassing. Indeed, despite having a good accuracy and being easy to use, the thermocouples measure the temperature locally and their results are highly affected by their position and by the quality of the contact with the cell. This not optimal in thermal runaway studies because the cell temperature is not homogeneous, and the outgassing geometry is unpredictable. Finally, it could be interesting to perform the tests in a controlled atmosphere. In the current setup, CO is not detectable because its mass spectrum overlaps N₂ in the mass spectrometry measurements. The use of an ambient gas other than air could remedy this problem. Finally, the numerical simulations implemented were very simple and only considered the combustion of the released gases. The chemical reactions that take place inside the cell, the heat transfer between the different surfaces and the flow physics of the outgassing were neglected.

CHAPTER 8 CONCLUSION, IMPACT AND OUTLOOK

8.1 Conclusion

The state of the art related to the thermal runaway of Li-ion cells explained the phenomenon and summarized the current available knowledge. To expand this knowledge, the effects of heating rate and ageing were studied experimentally. The initial temperature of thermal runaway increased with the heating rate and the thermal runaway was more spontaneous for high heating rates (approximately 20 °C/min) while the effects of ageing could not be clearly identified due to a limited number of tests. The temporal evolution of the concentrations of several gas species in the outgassing (H_2 , H_2O , CO_2 , DMC, C_3H_6 , C_6H_6 and LiF) were identified by mass spectrometry. The particle emissions were successfully analysed with two particle-size spectrometers running simultaneously. The results showed two peaks in the particle distribution, the first one being for particles with a diameter below 50nm and the second one for particles with a diameter between 100 and 150nm. Temperature measurement by infrared analysis was compared with thermocouple measurements. This new technique could potentially improve the measurements in thermal runaway testing by providing a complete map of temperature. The temperature of hard-to-reach areas such as the positive pole through the flame was monitored by using the multispectral camera. Finally, the combustion models implemented in this work were able to give good temperature approximations and allowed the study of the combustion products.

8.2 Impact and outlook

The modification of a standard cone calorimeter implemented in this work enabled the precise quantification of the combustion-mediated heat release during the thermal runaway of Li-ion cells. The heating system allowed the effect of the heating rate to be investigated. These instruments were extensively tested during this study and constitute a strong basis for future experimental work. The results gathered confirm data found in the literature in terms of outgassing composition and extends them to provide temporal information and the effects of heating rate. This method could be an alternative to FTIR measurements, allowing the detection of minority gas species with a better sensitivity. Novel results are also presented on the particle-size distribution resulting from the combustion and the use of a multispectral camera to obtain temperature information. To our knowledge, particle size distribution during the thermal

runaway of Li-ion cells was never characterized prior to this study. Infrared imaging measurements appear to be a powerful tool to acquire temperature of both the cell casing and the outgassing and to measure the temperature of hard-to-reach areas. It also allowed a clear visualization of both venting events and of the flame.

REFERENCES

- [1] A. Yoshino, "The birth of the lithium-ion battery," *Angewandte Chemie - International Edition*, vol. 51, no. 24, pp. 5798-5800, 2012, doi: 10.1002/anie.201105006.
- [2] S. Abada, G. Marlair, A. Lecocq, M. Petit, V. Sauvart-Moynot, and F. Huet, "Safety focused modeling of lithium-ion batteries: A review," *Journal of Power Sources*, vol. 306, pp. 178-192, 2016, doi: 10.1016/j.jpowsour.2015.11.100.
- [3] Q. Wang, P. Ping, X. Zhao, G. Chu, J. Sun, and C. Chen, "Thermal runaway caused fire and explosion of lithium ion battery," vol. 208, ed, 2012, pp. 210-224.
- [4] J.-M. Tarascon, "Histoire et évolution des technologies d'accumulateurs," Laboratoire de Réactivité et de Chimie des Solides, Class presentation, 2011.
- [5] S. Abada, "Compréhension et modélisation de l'emballage thermique de batteries Li-ion neuves et vieillies," PhD Thèse de Doctorat, Université Pierre et Marie Curie, 2016.
- [6] J. C. Hewson and S. P. Domino, "Thermal runaway of lithium-ion batteries and hazards of abnormal thermal environments," *9th US National Combustion Meeting*, pp. 1-9, 2015.
- [7] Z. Zhang and P. Ramadass, "Lithium-Ion Battery lithium-ion battery Systems and Technology lithium-ion battery technology," in *Encyclopedia of Sustainability Science and Technology*, R. A. Meyers Ed. New York, NY: Springer New York, 2012, pp. 6122-6149.
- [8] I. Rtca, "DO-311A - Minimum Operational Performance Standards for Rechargeable Lithium Batteries and Battery Systems," 2017.
- [9] ISO, "ISO 5660-1 - Reaction-to-fire tests - Heat release, smoke production and mass loss rate," 2015.
- [10] R. Jack and A. Jean, "Accumulateurs Accumulateurs au lithium," (in fre), *Techniques de l'ingénieur Accumulateurs d'énergie*, Article de base documentaire vol. base documentaire : TIB243DUO, no. ref. article : d3354, 2005. [Online]. Available: <https://www.techniques-ingenieur.fr/base-documentaire/energies-th4/accumulateurs-d-energie-42243210/accumulateurs-d3354/>.
- [11] X. Feng, M. Ouyang, X. Liu, L. Lu, Y. Xia, and X. He, "Thermal runaway mechanism of lithium ion battery for electric vehicles: A review," *Energy Storage Materials*, vol. 10, no. December 2016, pp. 246-267, 2018, doi: 10.1016/j.ensm.2017.05.013.
- [12] A. W. Golubkov *et al.*, "Thermal runaway of large automotive Li-ion batteries," *RSC Advances*, vol. 8, no. 70, pp. 40172-40186, 2018, doi: 10.1039/C8RA06458J.
- [13] A. Nedjalkov *et al.*, "Toxic gas emissions from damaged lithium ion batteries-analysis and safety enhancement solution," *Batteries*, vol. 2, no. 1, pp. 1-10, 2016, doi: 10.3390/batteries2010005.
- [14] D. H. Doughty, E. P. Roth, C. C. Crafts, G. Nagasubramanian, G. Henriksen, and K. Amine, "Effects of additives on thermal stability of Li ion cells," *Journal of Power Sources*, vol. 146, no. 1-2, pp. 116-120, 2005, doi: 10.1016/j.jpowsour.2005.03.170.
- [15] S. Koch, A. Fill, and K. P. Birke, "Comprehensive gas analysis on large scale automotive lithium-ion cells in thermal runaway," *Journal of Power Sources*, vol. 398, no. June, pp. 106-112, 2018, doi: 10.1016/j.jpowsour.2018.07.051.

- [16] N. Ponchaut *et al.*, "Thermal Runaway and Safety of Large Lithium-Ion Battery Systems Single Cell Failure," *Battcon 2015*, pp. 1-10, 2015.
- [17] A. Lecocq, G. G. Eshetu, S. Grugeon, N. Martin, S. Laruelle, and G. Marlair, "Scenario-based prediction of Li-ion batteries fire-induced toxicity," *Journal of Power Sources*, vol. 316, pp. 197-206, 2016, doi: 10.1016/j.jpowsour.2016.02.090.
- [18] G. Marlair, L. Dupont, and M. Demissy, "Approche de la maîtrise des risques spécifiques de la filière véhicules électriques - Analyse préliminaire des risques," 2011. [Online]. Available: http://ridum.umanizales.edu.co:8080/jspui/bitstream/6789/377/4/Muñoz_Zapata_Adriana_Patricia_Artículo_2011.pdf
- [19] N. Warner, "Overview of a Year of Battery Fire Testing by DNV GL for Con Ed, NYSERDA and FDNY," in *NFPA 855 Committee Meeting*, 2017.
- [20] P. Economy. "Lithium-Ion Battery on Delta Air Lines Flight Explodes, Catches Fire." <https://www.inc.com/peter-economy/lithium-ion-battery-on-delta-air-lines-flight-explodes-catches-fire-quick-thinking-crew-averts-disaster.html> (accessed).
- [21] D. Jones. "A passenger's battery charger exploded on United flight, forcing an emergency landing." <https://www.washingtonpost.com/travel/2020/02/27/passengers-laptop-battery-exploded-united-flight-forcing-an-emergency-landing/> (accessed).
- [22] N. Guillet, "Les risques liés aux batteries lithium-ion," INES - National Institute of Solar Energy, 2019.
- [23] X. Liu *et al.*, "Thermal Runaway of Lithium-Ion Batteries without Internal Short Circuit," *Joule*, vol. 2, no. 10, pp. 2047-2064, 2018, doi: 10.1016/j.joule.2018.06.015.
- [24] A. W. Golubkov *et al.*, "Thermal-runaway experiments on consumer Li-ion batteries with metal-oxide and olivin-type cathodes," *RSC Advances*, vol. 4, no. 7, pp. 3633-3642, 2014, doi: 10.1039/c3ra45748f.
- [25] W. Li, H. Wang, M. Ouyang, C. Xu, L. Lu, and X. Feng, "Theoretical and experimental analysis of the lithium-ion battery thermal runaway process based on the internal combustion engine combustion theory," *Energy Conversion and Management*, vol. 185, no. October 2018, pp. 211-222, 2019, doi: 10.1016/j.enconman.2019.02.008.
- [26] S. Scharner, "Quantitative safety characterization of Li-ion cells," in *JRC Exploratory Research Workshop*, 2018: BMW Group.
- [27] M. Lammer, A. Königseder, and V. Hacker, "Holistic methodology for characterisation of the thermally induced failure of commercially available 18650 lithium ion cells," *RSC Advances*, vol. 7, no. 39, pp. 24425-24429, 2017, doi: 10.1039/c7ra02635h.
- [28] G. G. Eshetu *et al.*, "Fire behavior of carbonates-based electrolytes used in Li-ion rechargeable batteries with a focus on the role of the LiPF₆ and LiFSI salts," *Journal of Power Sources*, 2014, doi: 10.1016/j.jpowsour.2014.07.065.
- [29] N. S. Spinner *et al.*, "Physical and chemical analysis of lithium-ion battery cell-to-cell failure events inside custom fire chamber," *Journal of Power Sources*, vol. 279, pp. 713-721, 2015, doi: 10.1016/j.jpowsour.2015.01.068.
- [30] P. Ribière, S. Grugeon, M. Morcrette, S. Boyanov, S. Laruelle, and G. Marlair, "Investigation on the fire-induced hazards of Li-ion battery cells by fire calorimetry,"

- Energy and Environmental Science*, vol. 5, no. 1, pp. 5271-5280, 2012, doi: 10.1039/c1ee02218k.
- [31] Y. Wang, S. Song, C. Xu, N. Hu, J. Molenda, and L. Lu, "Development of solid-state electrolytes for sodium-ion battery—A short review," *Nano Materials Science*, 2019, doi: 10.1016/j.nanoms.2019.02.007.
- [32] M. A. Manzo *et al.*, "NASA Aerospace Flight Battery Systems Program," NASA Langley Research Center; Hampton, VA, United States, 2010002806, 2010.
- [33] P. V. Chombo and Y. Laonual, "A review of safety strategies of a Li-ion battery," *Journal of Power Sources*, vol. 478, p. 228649, 2020/12/01/ 2020, doi: <https://doi.org/10.1016/j.jpowsour.2020.228649>.
- [34] F. Larsson, S. Bertilsson, M. Furlani, I. Albinsson, and B. E. Mellander, "Gas explosions and thermal runaways during external heating abuse of commercial lithium-ion graphite-LiCoO₂ cells at different levels of ageing," *Journal of Power Sources*, vol. 373, no. October 2017, pp. 220-231, 2018, doi: 10.1016/j.jpowsour.2017.10.085.
- [35] M. Fleischhammer, T. Waldmann, G. Bisle, B. I. Hogg, and M. Wohlfahrt-Mehrens, "Interaction of cyclic ageing at high-rate and low temperatures and safety in lithium-ion batteries," *Journal of Power Sources*, vol. 274, pp. 432-439, 2015, doi: 10.1016/j.jpowsour.2014.08.135.
- [36] K. Leung, "First-principles modeling of the initial stages of organic solvent decomposition on Li xMn₂O₄(100) surfaces," *Journal of Physical Chemistry C*, vol. 116, no. 18, pp. 9852-9861, 2012, doi: 10.1021/jp212415x.
- [37] "RTCA Website." <https://www.rtca.org/> (accessed).
- [38] T. O'Hara, "Navigating the Regulatory Maze of Lithium Battery Safety," Intertek, 2014. [Online]. Available: www.intertek.com/energy-storage
- [39] D. H. Doughty, "The Landscape of Thermal Runaway Propagation Testing," *JRC Exploratory Research Workshop*, pp. 1-30, 2018. [Online]. Available: <https://ec.europa.eu/jrc/sites/jrcsh/files/landscape-thermal-runaway-propagation-testing.pdf>.
- [40] "Metlabs Website." <https://www.metlabs.com/battery/top-3-standards-for-lithium-battery-safety-testing/> (accessed).
- [41] "Lithium-batterie-service Website." <https://www.lithium-batterie-service.de/en/un-38.3-test-series> (accessed).
- [42] L. Florence, "Safety Issues for Lithium-Ion Batteries," *Underwriters Laboratories - Whitepapers*, 2013. [Online]. Available: <http://www.ul.com/global/eng/pages/library/index.jsp?document=Safety> Issues for Lithium-Ion Batteries.
- [43] "IEC Webstore." <https://webstore.iec.ch/publication/29052> (accessed).
- [44] "IEEE Standard for Rechargeable Batteries for Multi-Cell Mobile Computing Devices," *IEEE Std 1625-2008 (Revision of IEEE Std 1625-2004)*, pp. 1-0, 2008, doi: 10.1109/IEEESTD.2008.4657368.
- [45] "IEEE Standard for Rechargeable Batteries for Cellular Telephones - Redline," *IEEE Std 1725-2011(Revision to IEEE Std 1725-2006) - Redline*, pp. 1-101, 2011.

- [46] P. T. Coman, S. Rayman, and R. E. White, "A lumped model of venting during thermal runaway in a cylindrical Lithium Cobalt Oxide lithium-ion cell," *Journal of Power Sources*, 2016, doi: 10.1016/j.jpowsour.2015.12.088.
- [47] L. Kong, C. Li, J. Jiang, and M. G. Pecht, "Li-ion battery fire hazards and safety strategies," *Energies*, vol. 11, no. 9, pp. 1-11, 2018, doi: 10.3390/en11092191.
- [48] Y. Fu, S. Lu, K. Li, C. Liu, X. Cheng, and H. Zhang, "An experimental study on burning behaviors of 18650 lithium ion batteries using a cone calorimeter," *Journal of Power Sources*, 2015, doi: 10.1016/j.jpowsour.2014.09.039.
- [49] F. Larsson, P. Andersson, P. Blomqvist, A. Lorén, and B. E. Mellander, "Characteristics of lithium-ion batteries during fire tests," *Journal of Power Sources*, vol. 271, pp. 414-420, 2014, doi: 10.1016/j.jpowsour.2014.08.027.
- [50] J. G. Quintiere, "On methods to measure the energetics of a lithium ion battery in thermal runaway," *Fire Safety Journal*, vol. 111, no. November 2019, pp. 102911-102911, 2020, doi: 10.1016/j.firesaf.2019.102911.
- [51] V. Somandepalli, K. Marr, and Q. Horn, "Quantification of combustion hazards of thermal runaway failures in lithium-ion batteries," *SAE International Journal of Alternative Powertrains*, vol. 3, no. 1, pp. 98-104, 2014, doi: 10.4271/2014-01-1857.
- [52] G. Gachot *et al.*, "Gas chromatography/mass spectrometry as a suitable tool for the lithium battery electrolyte degradation mechanisms study," *Analytical Chemistry*, vol. 83, no. 2, pp. 478-485, 2011, doi: 10.1021/ac101948u.
- [53] Q. Wang, P. Huang, P. Ping, Y. Du, K. Li, and J. Sun, "Combustion behavior of lithium iron phosphate battery induced by external heat radiation," *Journal of Loss Prevention in the Process Industries*, vol. 49, pp. 961-969, 2017, doi: 10.1016/j.jlp.2016.12.002.
- [54] T. Maloney, "Lithium Battery Thermal Runaway Vent Gas Analysis - Composition and Effect of Combustion," Federal Aviation Administration, 2015.
- [55] D. Ren *et al.*, "A comparative investigation of aging effects on thermal runaway behavior of lithium-ion batteries," *eTransportation*, vol. 2, pp. 100034-100034, 2019, doi: 10.1016/j.etrans.2019.100034.
- [56] P. Röder, B. Stiaszny, J. C. Ziegler, N. Baba, P. Lagaly, and H. D. Wiemhöfer, "The impact of calendar aging on the thermal stability of a LiMn₂O₄-Li(Ni_{1/3}Mn_{1/3}Co_{1/3})O₂/graphite lithium-ion cell," *Journal of Power Sources*, vol. 268, pp. 315-325, 2014, doi: 10.1016/j.jpowsour.2014.06.040.
- [57] A. Wu, D. Wu, and C. Wang, "Failure mechanism due to aging effects in lithium-ion batteries," *INTELEC, International Telecommunications Energy Conference (Proceedings)*, vol. 2016-September, 2016, doi: 10.1109/INTLEC.2015.7572369.
- [58] A. W. Golubkov *et al.*, "Thermal runaway of commercial 18650 Li-ion batteries with LFP and NCA cathodes - Impact of state of charge and overcharge," *RSC Advances*, vol. 5, no. 70, pp. 57171-57186, 2015, doi: 10.1039/c5ra05897j.
- [59] T. M. Kruse, H. W. Wong, and L. J. Broadbelt, "Mechanistic modeling of polymer pyrolysis: Polypropylene," *Macromolecules*, vol. 36, no. 25, pp. 9594-9607, 2003, doi: 10.1021/ma030322y.
- [60] S. E. Levine and L. J. Broadbelt, "Detailed mechanistic modeling of high-density polyethylene pyrolysis: Low molecular weight product evolution," *Polymer*

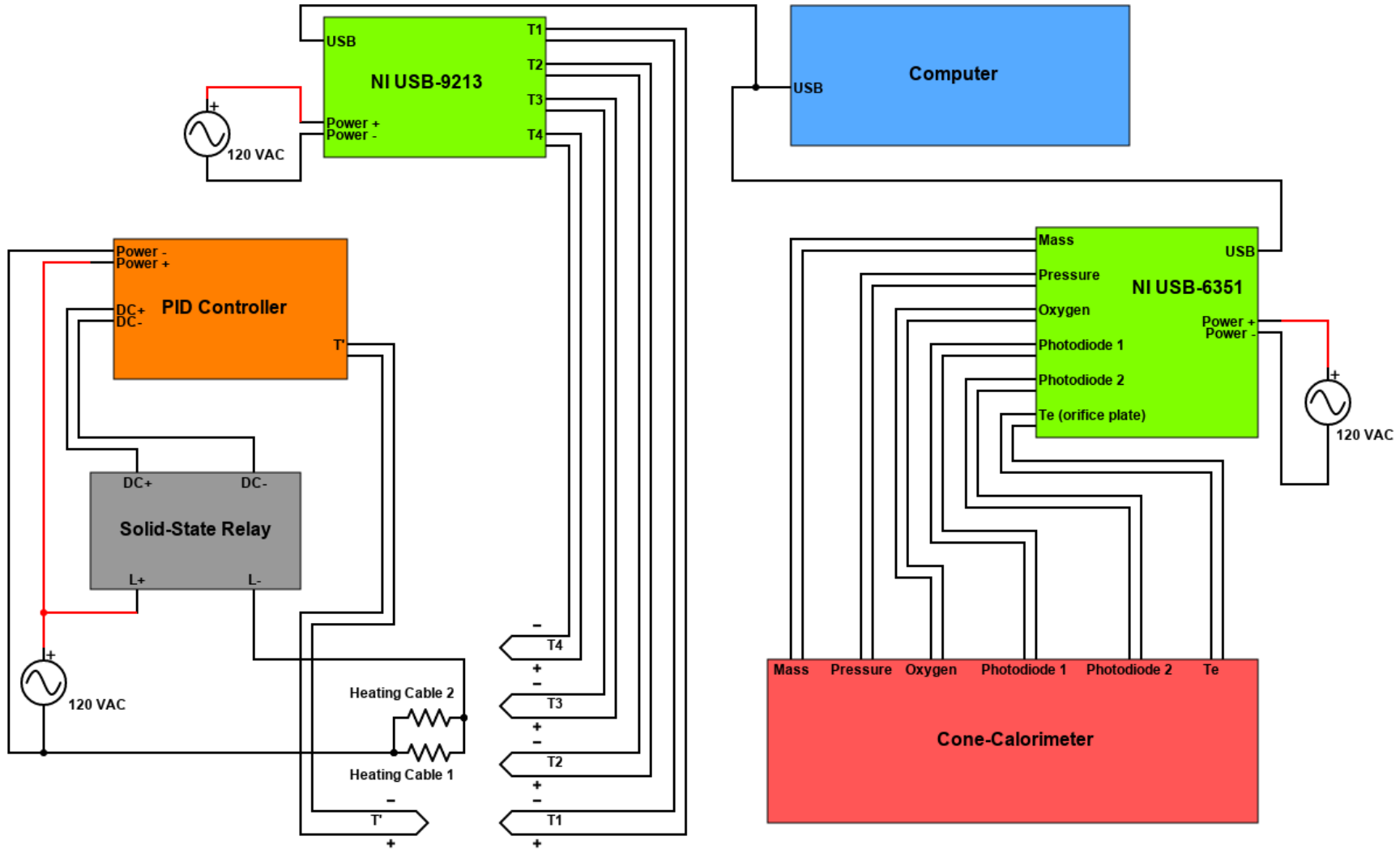
- Degradation and Stability*, vol. 94, no. 5, pp. 810-822, 2009, doi: 10.1016/j.polymdegradstab.2009.01.031.
- [61] R. W. J. Westerhout, J. Waanders, J. A. M. Kuipers, and W. P. M. Van Swaaij, "Kinetics of the low-temperature pyrolysis of polyethene, polypropene, and polystyrene modeling, experimental determination, and comparison with literature models and data," *Industrial and Engineering Chemistry Research*, vol. 36, no. 6, pp. 1955-1964, 1997, doi: 10.1021/ie960501m.
- [62] G. H. Kim, A. Pesaran, and R. Spotnitz, "A three-dimensional thermal abuse model for lithium-ion cells," *Journal of Power Sources*, vol. 170, no. 2, pp. 476-489, 2007, doi: 10.1016/j.jpowsour.2007.04.018.
- [63] A. Melcher, C. Ziebert, M. Rohde, and H. J. Seifert, "Modeling and simulation of the thermal runaway behavior of cylindrical Li-ion cells-computing of critical parameters," *Energies*, vol. 9, no. 4, pp. 1-19, 2016, doi: 10.3390/en9040292.
- [64] N. Tanaka, "Modeling and Simulation of Thermo-Electrochemistry of Thermal Runaway in Lithium-Ion Batteries," *Journal of Chemical Information and Modeling*, vol. 53, no. 9, pp. 1689-1699, 2013, doi: 10.1017/CBO9781107415324.004.
- [65] J. Johnsplass, "Lithium-ion battery safety," Master's Thesis, University College of Southeast Norway, 2017.
- [66] J. Johnsplass, M. Henriksen, K. Vaagsaether, J. Lundberg, and D. Bjerketvedt, "Simulation of burning velocities in gases vented from thermal run-a-way lithium ion batteries," in *The 58th Conference on Simulation and Modeling (SIMS 2017)*, Reykjavik, Iceland, 2017 2017, pp. 157-161, doi: 10.3384/ecp17138157.
- [67] E. Robert, "Mass spectrometer calibration over wide concentration ranges in multicomponent gas mixtures," *Measurement Science and Technology*, vol. 21, no. 2, 2010, doi: 10.1088/0957-0233/21/2/025102.
- [68] A. Masias, J. Marcicki, and W. A. Paxton, "Opportunities and Challenges of Lithium Ion Batteries in Automotive Applications," *ACS Energy Letters*, vol. 6, no. 2, pp. 621-630, 2021, doi: 10.1021/acsenerylett.0c02584.
- [69] D. Stampatori, P. P. Raimondi, and M. Noussan, "Li-ion batteries: A review of a key technology for transport decarbonization," *Energies*, vol. 13, no. 10, 2020, doi: 10.3390/en13102638.
- [70] P. Jindal and J. Bhattacharya, "Review—Understanding the Thermal Runaway Behavior of Li-Ion Batteries through Experimental Techniques," *Journal of The Electrochemical Society*, vol. 166, no. 10, pp. A2165-A2193, 2019, doi: 10.1149/2.1381910jes.
- [71] L. Yuan, T. Dubaniewicz, I. Zlochower, R. Thomas, and N. Rayyan, "Experimental study on thermal runaway and vented gases of lithium-ion cells," *Process Safety and Environmental Protection*, vol. 144, pp. 186-192, 2020, doi: 10.1016/j.psep.2020.07.028.
- [72] S. Chen, Z. Wang, J. Wang, X. Tong, and W. Yan, "Lower explosion limit of the vented gases from Li-ion batteries thermal runaway in high temperature condition," *Journal of Loss Prevention in the Process Industries*, vol. 63, no. December 2018, pp. 103992-103992, 2020, doi: 10.1016/j.jlp.2019.103992.

- [73] B. S. Parimalam, A. D. MacIntosh, R. Kadam, and B. L. Lucht, "Decomposition Reactions of Anode Solid Electrolyte Interphase (SEI) Components with LiPF₆," *Journal of Physical Chemistry C*, vol. 121, no. 41, pp. 22733-22738, 2017, doi: 10.1021/acs.jpcc.7b08433.
- [74] X. G. Teng, F. Q. Li, P. H. Ma, Q. D. Ren, and S. Y. Li, "Study on thermal decomposition of lithium hexafluorophosphate by TG-FT-IR coupling method," *Thermochimica Acta*, vol. 436, no. 1-2, pp. 30-34, 2005, doi: 10.1016/j.tca.2005.07.004.
- [75] A. W. Golubkov, R. Planteu, B. Rasch, C. Essl, A. Thaler, and V. Hacker, "Thermal runaway and battery fire: comparison of Li-ion, Ni-MH and sealed lead-acid batteries," *7th Transport Research Arena TRA 2018*, vol. 43, no. 316, 2018, doi: 10.5281/zenodo.1491317.
- [76] K. Liu, Y. Liu, D. Lin, A. Pei, and Y. Cui, "Materials for lithium-ion battery safety," *Science Advances*, vol. 4, no. 6, 2018, doi: 10.1126/sciadv.aas9820.
- [77] F. Larsson and B. E. Mellander, "Abuse by External Heating, Overcharge and Short Circuiting of Commercial Lithium-Ion Battery Cells," *Journal of the Electrochemical Society*, vol. 161, pp. A1611-A1617, 06/27 2014, doi: 10.1149/2.0311410jes.
- [78] Q. Zhang, T. Liu, and Q. Wang, "Experimental study on the influence of different heating methods on thermal runaway of lithium-ion battery," *Journal of Energy Storage*, vol. 42, no. April, pp. 103063-103063, 2021, doi: 10.1016/j.est.2021.103063.
- [79] Z. Huang, T. Shen, K. Jin, J. Sun, and Q. Wang, "Heating power effect on the thermal runaway characteristics of large-format lithium ion battery with Li(Ni_{1/3}Co_{1/3}Mn_{1/3})O₂ as cathode," *Energy*, vol. 239, pp. 121885-121885, 2021, doi: 10.1016/j.energy.2021.121885.
- [80] S. Sripad, A. Bills, and V. Viswanathan, "A review of safety considerations for batteries in aircraft with electric propulsion," *MRS Bulletin*, vol. 46, no. 5, pp. 435-442, 2021, doi: 10.1557/s43577-021-00097-1.
- [81] ISO, "ISO 2685:1998 : Aircraft — Environmental test procedure for airborne equipment — Resistance to fire in designated fire zones," 1998.
- [82] M. Chen *et al.*, "Investigation on the thermal hazards of 18650 lithium ion batteries by fire calorimeter," *Journal of Thermal Analysis and Calorimetry*, vol. 122, 06/02 2015, doi: 10.1007/s10973-015-4751-5.
- [83] J. Lamb, L. Torres-Castro, J. C. Hewson, R. C. Shurtz, and Y. Preger, "Investigating the Role of Energy Density in Thermal Runaway of Lithium-Ion Batteries with Accelerating Rate Calorimetry," *Journal of The Electrochemical Society*, vol. 168, no. 6, pp. 060516-060516, 2021, doi: 10.1149/1945-7111/ac0699.
- [84] D. Patel, J. B. Robinson, S. Ball, D. J. L. Brett, and P. R. Shearing, "Thermal Runaway of a Li-Ion Battery Studied by Combined ARC and Multi-Length Scale X-ray CT," *Journal of The Electrochemical Society*, vol. 167, no. 9, pp. 090511-090511, 2020, doi: 10.1149/1945-7111/ab7fb6.
- [85] A. A. Abd-El-Latif, P. Sichler, M. Kasper, T. Waldmann, and M. Wohlfahrt-Mehrens, "Insights Into Thermal Runaway of Li-Ion Cells by Accelerating Rate Calorimetry Coupled with External Sensors and Online Gas Analysis," *Batteries & Supercaps*, pp. 1-11, 2021, doi: 10.1002/batt.202100023.

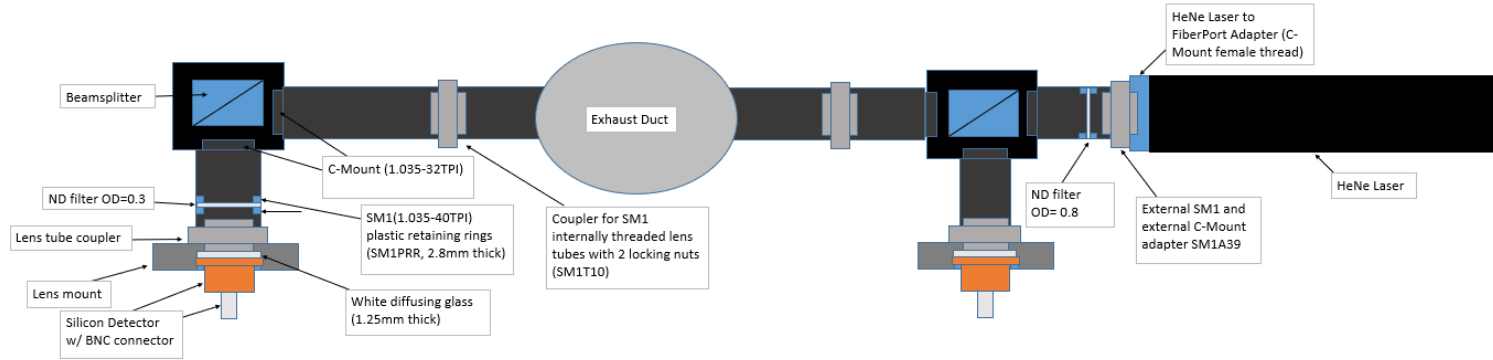
- [86] M. L. Janssens, "9 - Material Flammability," in *Handbook of Environmental Degradation of Materials (Second Edition)*, M. Kutz Ed. Oxford: William Andrew Publishing, 2012, pp. 283-307.
- [87] J. G. Quintiere, "More on methods to measure the energetics of lithium ion batteries in thermal runaway," vol. 124, ed, 2021.
- [88] H. Wang, W. Shi, F. Hu, Y. Wang, X. Hu, and H. Li, "Over-heating triggered thermal runaway behavior for lithium-ion battery with high nickel content in positive electrode," *Energy*, vol. 224, p. 120072, 2021/06/01/ 2021, doi: <https://doi.org/10.1016/j.energy.2021.120072>.
- [89] G. Gachot *et al.*, "Gas chromatography/Fourier transform infrared/mass spectrometry coupling: A tool for Li-ion battery safety field investigation," *Analytical Methods*, vol. 6, no. 15, pp. 6120-6124, 2014, doi: 10.1039/c4ay00054d.
- [90] Y. Zhang, H. Wang, W. Li, C. Li, and M. Ouyang, "Size distribution and elemental composition of vent particles from abused prismatic Ni-rich automotive lithium-ion batteries," *Journal of Energy Storage*, vol. 26, p. 100991, 2019/12/01/ 2019, doi: <https://doi.org/10.1016/j.est.2019.100991>.
- [91] T elops, "Observation and Quantification of CO2 passive degassing at sulphur Banks from Kilauea Volcano using thermal Infrared Multispectral Imaging," pp. 8-8, 2020.
- [92] J. Kopp and G. A. Slack, "Thermal contact problems in low temperature thermocouple thermometry," *Cryogenics*, vol. 11, no. 1, pp. 22-25, 1971/02/01/ 1971, doi: [https://doi.org/10.1016/0011-2275\(71\)90005-1](https://doi.org/10.1016/0011-2275(71)90005-1).
- [93] Y. P. Shlykov and Y. A. Ganin, "Thermal resistance of metallic contacts," *International Journal of Heat and Mass Transfer*, vol. 7, no. 8, pp. 921-929, 1964/08/01/ 1964, doi: [https://doi.org/10.1016/0017-9310\(64\)90147-4](https://doi.org/10.1016/0017-9310(64)90147-4).
- [94] L. Wang *et al.*, "Unlocking the significant role of shell material for lithium-ion battery safety," *Materials & Design*, vol. 160, pp. 601-610, 2018/12/15/ 2018, doi: <https://doi.org/10.1016/j.matdes.2018.10.002>.
- [95] M. Klanchar, B. D. Wintrode, and J. A. Phillips, "Lithium–Water Reaction Chemistry at Elevated Temperature," *Energy & Fuels*, vol. 11, no. 4, pp. 931-935, 1997/07/01 1997, doi: 10.1021/ef970047e.
- [96] J. H. Leckey, L. E. Nulf, and J. R. Kirkpatrick, "Reaction of Lithium Hydride with Water," *Langmuir*, vol. 12, no. 26, pp. 6361-6367, 1996/01/01 1996, doi: 10.1021/la950843h.
- [97] M. M. Maricq, "A comparison of soot size and charge distributions from ethane, ethylene, acetylene, and benzene/ethylene premixed flames," *Combustion and Flame*, vol. 144, no. 4, pp. 730-743, 2006/03/01/ 2006, doi: <https://doi.org/10.1016/j.combustflame.2005.09.007>.
- [98] B. Mao, H. Chen, L. Jiang, C. Zhao, J. Sun, and Q. Wang, "Refined study on lithium ion battery combustion in open space and a combustion chamber," *Process Safety and Environmental Protection*, vol. 139, pp. 133-146, 2020, doi: 10.1016/j.psep.2020.03.037.

- [99] D. E. Schraufnagel, "The health effects of ultrafine particles," *Experimental & Molecular Medicine*, vol. 52, no. 3, pp. 311-317, 2020/03/01 2020, doi: 10.1038/s12276-020-0403-3.
- [100] "Cantera Website." <https://cantera.org/index.html> (accessed).
- [101] R. J. Kee and M. E. Coltrin, *CHEMICALLY REACTING FLOW CHEMICALLY REACTING FLOW Second Edition*. 2018.

APPENDIX A WIRING DIAGRAM OF THE SETUP



APPENDIX B SMOKE OBSCURATION SYSTEM (TAKEN FROM S.C. BOENTA)



Item	Qty. reqd.	Supplier	Part no.	Diameter	Length	Thread Type	Thread Gender	Thread depth
Cube	2	NewPort	OC1-CM	1-inch	N/A	SM1	Female	
Cube Mount	2	NewPort	OC1-CM-A	N/A	N/A	N/A	N/A	
Cube Mount Cover Plate	2	NewPort	OC1-CMC	N/A	N/A	N/A	N/A	
Cube Beamsplitter	2	NewPort	10BC16NP.4	N/A	1-inch	N/A	N/A	
Lens Tube 3-inch	2	NewPort	LT10-30	1-inch	76.2mm	SM1/SM1	Male/Female	3mm/76.2mm
Lens Tube 2-inch	4	NewPort	LT10-20	1-inch	50.8mm	SM1/SM1	Male/Female	3mm/50.8mm
Lens Tube 1-inch	1	NewPort	LT10-10	1-inch	25.4mm	SM1/SM1	Male/Female	3mm/25.4mm
Optical Cage Adaptor 30mm and 40mm	4	Newport	OC1-A30	1-inch	N/A	SM1	Female	10.2mm
Retaining Rings	10	NewPort	LT10-RR	1-inch	N/A	SM1	Male	2mm
Spanner Wrench	1	NewPort	LT10-WR	N/A	1-inch	N/A	N/A	N/A
Lens Tube Coupler	4	NewPort	LT10-LX	1-inch	12.7mm	SM1	Male	12.7

Post Mount	4	NewPort	OC1-PM	N/A	N/A	N/A	N/A	N/A
Post Holder with Clamp	4	NewPort	Q-TMS-3	1-inch	3-inch	N/A	N/A	N/A
Pedestal Optical Post	4	NewPort	PS-3E	1-inch	3-inch	M4	Female	N/A
Laser Coupler	1	NewPort	R-30646-R	1-inch	N/A	C-Mount (1,000-32TPI)	Female	12.7mm
Cage rods 6-inch	8	NewPort	OC1-GR-6S	6mm	6-inch	M4	Female	N/A
Cage rods 3-inch	8	NewPort	OC1-GR-3	6mm	3-inch	M4	Female	N/A
Beam splitter	2	Edmund Optics	49-685	1-inch	N/A	C-Mount (1,000-32TPI)	Female	N/A
Silicon Detector	2	Edmund Optics	53-379	1-inch	N/A	N/A	N/A	N/A
ND Filter 0,3	1	Edmund Optics	84-024	1-inch	N/A	N/A	N/A	N/A
ND Filter 0,8	1	Edmund Optics	84-029	1-inch	N/A	N/A	N/A	N/A
White diffusing glass	2	Edmund Optics	34-473	1-inch	N/A	N/A	N/A	N/A

APPENDIX C UNCERTAINTY ON THE HEAT RELEASE RATE (HRR)

Data:

HRR can be determined by O₂ consumption. The relation is given in the ISO 5660-1 standard:

$$\dot{q}(t) = 1.10 * \frac{\Delta h_c}{r_0} * C * \sqrt{\frac{\Delta p}{T_e}} * \frac{X_{O_2}^0 - X_{O_2}(t)}{1.105 - 1.5X_{O_2}(t)}$$

Where $\frac{\Delta h_c}{r_0}$ is taken as $13.1 * 10^3$ kJ/kg (unless a more accurate value is known), $X_{O_2}^0$ is the average of the oxygen analyser output (mole fraction of oxygen) during 1min without combustion, $X_{O_2}(t)$ is the mole fraction of oxygen at time t (considering the delay time of the oxygen analyser), 1.10 is the ratio of molecular weights of oxygen and air, Δp is the difference of pression at the orifice plate of the cone calorimeter, T_e is the temperature of the gas mixture at the orifice plate and C is a calibration constant.

The calibration constant C is calculated using:

$$C = \frac{\dot{q}_b}{1.10 * (12.54 * 10^3)} * \sqrt{\frac{T_e}{\Delta p}} * \frac{1.105 - 1.5X_{O_2}}{X_{O_2}^0 - X_{O_2}}$$

Where \dot{q}_b is the HRR in kW of the methane supplied during the calibration test ($\dot{q}_b = 5 \pm 0.5$ kW) and $12.54 * 10^3$ is $\frac{\Delta h_c}{r_0}$ for methane.

Uncertainty calculation:

The relative uncertainty of the HRR is:

$$\frac{\Delta \dot{q}}{\dot{q}} = \frac{\Delta C}{C} + 0.5 * \frac{\Delta(\Delta p)}{(\Delta p)} + 0.5 * \frac{\Delta T_e}{T_e} + \frac{\Delta X_{O_2}^0 + \Delta X_{O_2}}{|X_{O_2}^0 - X_{O_2}|} + \frac{\Delta X_{O_2}}{X_{O_2}}$$

Where $\frac{\Delta X_{O_2}^0 + \Delta X_{O_2}}{X_{O_2}^0 - X_{O_2}}$ is the relative uncertainty of $X_{O_2}^0 - X_{O_2}$.

Moreover, the relative uncertainty on C is:

$$\frac{\Delta C}{C} = \frac{\Delta \dot{q}_b}{\dot{q}_b} + 0.5 * \frac{\Delta(\Delta p)}{(\Delta p)} + 0.5 * \frac{\Delta T_e}{T_e} + \frac{\Delta X_{O_2}^0 + \Delta X_{O_2}}{|X_{O_2}^0 - X_{O_2}|} + \frac{\Delta X_{O_2}}{X_{O_2}}$$

And $\frac{\Delta \dot{q}_b}{\dot{q}_b} = \frac{0.5}{5} = 0.1$.

Therefore, the total relative uncertainty of HRR is:

$$\frac{\Delta \dot{q}}{\dot{q}} = 0.1 + \frac{\Delta T_e}{T_e} + \frac{\Delta(\Delta p)}{(\Delta p)} + 2 * \frac{\Delta X_{O_2}^0 + \Delta X_{O_2}}{|X_{O_2}^0 - X_{O_2}|} + 2 * \frac{\Delta X_{O_2}}{X_{O_2}}$$

APPENDIX D GOVERNING EQUATIONS FOR THE 0D SIMULATION

Reactors 0D are the simplest combustion simulations in Cantera. They are composed of a homogeneous control volume V . Several state variables are defined in this type of model: m [kg] the mass of the reactor's content, V [m³] the reactor volume, Y_k [-] the mass fractions for each species and a variable (U [J] the total internal energy, H [J] the total enthalpy or T [K] the temperature) describing the energy of the system.

The model implemented in this project is an "Ideal Gas Constant Pressure Reactor" reactor. Therefore, the gas is considered as an ideal gas and the pressure inside the reactor is constant over time. In order to keep a constant pressure, the simulation constantly adapts the reactor volume V .

Three governing equations permit calculating the steady state of the system: the mass conservation, the species conservation and the energy conservation equations. The following development is based on the work of Kee *et al.* and precisions are given on Cantera website [100, 101].

- Mass conservation

The total mass of the mixture inside the reactor is continually changing due to the flow through the inlets and the outlets:

$$\frac{dm}{dt} = \sum_{in} \dot{m}_{in} - \sum_{out} \dot{m}_{out}$$

With m [kg] the total mass of the mixture inside the reactor, \dot{m}_{in} [kg/s] the mass flow rate from one of the inlets and \dot{m}_{out} [kg/s] the mass flow rate from one of the outlets.

- Species conservation

The mass production rate for a given specie k is:

$$\dot{m}_{k,gen} = \dot{\omega}_k W_k V$$

With $\dot{m}_{k,gen}$ [kg/s] the mass production rate of specie k , $\dot{\omega}_k$ [mol.m⁻³.s⁻¹] the molar production rate by homogeneous chemical reactions of specie k , W_k [kg.mol⁻¹] the molar mass of specie k and V [m³] the volume of the reactor.

Inside the reactor, the rate of change in the mass of each species is:

$$m \frac{dY_k}{dt} = \sum_{in} \dot{m}_{in} Y_{k,in} - \sum_{out} \dot{m}_{out} Y_k + \dot{m}_{k,gen}$$

With m [kg] the total mass of the mixture inside the reactor, Y_k [-] the mass fraction of specie k inside the reactor, \dot{m}_{in} [kg/s] the mass flow rate from one of the inlets, $Y_{k,in}$ [-] the mass fraction of specie k in the flow of one of the inlets and \dot{m}_{out} [kg/s] the mass flow rate from one of the outlets.

- Energy conservation

The total enthalpy is expressed as a function of the temperature:

$$H = m \sum_k Y_k h_k(T)$$

With H [J] the total enthalpy inside the reactor, m [kg] the total mass of the mixture inside the reactor, Y_k [-] the mass fraction of specie k inside the reactor and $h_k(T)$ [J/kg] the specific enthalpy of the specie k at temperature T .

From this formulation, the derivative of H as a function of time can be expressed as:

$$\frac{dH}{dt} = h \frac{dm}{dt} + m c_p \frac{dT}{dt} + m \sum_k h_k \frac{dY_k}{dt}$$

With c_p [J.K⁻¹.kg⁻¹] the heat capacity of the gas mixture inside the reactor.

The energy conservation equation in a constant pressure reactor is:

$$\frac{dH}{dt} = -\dot{Q} + \sum_{in} \dot{m}_{in} h_{in} - h \sum_{out} \dot{m}_{out}$$

With \dot{Q} [J/s] the rate of heat transferred to the system and h_{in} [J/kg] the specific enthalpy of the mixture in one of the inlets.

By combining these two previous equations with the species conservation equation, a new formulation is found:

$$m c_p \frac{dT}{dt} = -\dot{Q} - \sum_k h_k \dot{m}_{k,gen} + \sum_{in} \dot{m}_{in} (h_{in} - \sum_k h_k Y_{k,in})$$

APPENDIX E GOVERNING EQUATIONS FOR THE 1D SIMULATIONS

Flame models in Cantera are steady axisymmetric stagnation flow simulations and compute the solution along the stagnation streamline. These equations can be used to model different flame types such as freely propagating premixed laminar flames, burner-stabilized premixed flames, counterflow diffusion flames or counterflow premixed flames. In this project, a counterflow diffusion flame and a burner-stabilized premixed flame are implemented.

Four governing equations permit to simulate this type of flame: the continuity equation, the radial momentum conservation equation, the energy conservation equation, and the species conservation equation. The following development is based on the work of Kee *et al.* and precisions are given on Cantera website [100, 101].

The system of equations is derived from the steady-state three dimensional Navier-Stokes equations by considering a flow only in the z-r plane. A similarity solution is used to reduce the three-dimensional governing equations to a single equation.

- Continuity (or mass conservation)

$$\frac{\partial \rho u}{\partial z} + 2\rho V = 0$$

- Radial momentum conservation

$$\rho u \frac{\partial V}{\partial z} + \rho V^2 = -\Lambda + \frac{\partial}{\partial z} \left(\mu \frac{\partial V}{\partial z} \right)$$

- Energy conservation

$$\rho c_p u \frac{\partial T}{\partial z} = \frac{\partial}{\partial z} \left(\lambda \frac{\partial T}{\partial z} \right) - \sum_k j_k c_{p,k} \frac{\partial T}{\partial z} - \sum_k h_k W_k \dot{\omega}_k$$

- Species conservation

$$\rho u \frac{\partial Y_k}{\partial z} = -\frac{\partial j_k}{\partial z} + W_k \dot{\omega}_k$$

With ρ [kg/m³] the density of the gas mixture, u [m/s] the axial velocity, v [m/s] the radial velocity, V [s⁻¹] the scaled radial velocity ($V = v/r$), Λ the pressure eigenvalue independent of

z ($\Lambda = \frac{1}{r} \frac{\partial p}{\partial r} = \text{constant}$), μ [Pa.s] the dynamic viscosity, c_p [J.K⁻¹.kg⁻¹] the specific heat capacity of the gas mixture, T [K] the temperature, λ [W.m⁻¹.K⁻¹] the thermal conductivity, j_k [kg.m⁻².s⁻¹] the diffusive mass flux of specie k , $c_{p,k}$ [J.K⁻¹.kg⁻¹] the specific heat capacity of specie k , h_k [J/kg] the specific enthalpy of the specie k , W_k [kg.mol⁻¹] the molar mass of specie k , $\dot{\omega}_k$ [mol.m⁻³.s⁻¹] the molar production rate by homogeneous chemical reactions of specie k and Y_k [-] the mass fraction of specie k .

The diffusive flux j_k is computed according to a mixture-averaged formulation:

$$j_k^* = -\rho \frac{W_k}{\bar{W}} D'_{km} \frac{\partial X_k}{\partial z}$$

and

$$j_k = j_k^* - Y_k \sum_i j_i^*$$

With \bar{W} [kg.mol⁻¹] the mean molecular weight of the gas mixture, D'_{km} [m²/s] the mixture-averaged diffusion coefficient for specie k and X_k [-] the mole fraction of specie k .

The second equation applies a correction to ensure that the sum of the mass fluxes is zero. This condition is not guaranteed by the mixture-averaged formulation alone.

The mixture-averaged diffusion coefficient for specie k (D'_{km}) is expressed as:

$$D'_{km} = (1 - X_k) * \left(\sum_{j \neq k} \frac{X_j}{D_{kj}} \right)^{-1}$$

With D_{kj} [m²/s] the binary diffusion coefficient (or multicomponent Stephan-Maxwell diffusivity).

The different types of flame (i.e. counterflow diffusion flame or burner-stabilized premixed flame) are defined by the boundary conditions. For a counterflow diffusion flame with a one-dimensional spatial domain $[z_{start}, z_{end}]$, the two boundary conditions are an inlet at $z = z_{start}$ and an opposed inlet at $z = z_{end}$. For a burner-stabilized premixed flame with a one-dimensional spatial domain $[z_{start}, z_{end}]$, the two boundary conditions are an inlet at $z = z_{start}$ and an outlet at $z = z_{end}$.

- Inlet boundary

For an inlet located at $z = z_0$ with a temperature T_0 , a mass flow rate per unit area \dot{m}_{0surf} , a scaled radial velocity V_0 and species mass fractions $Y_{k,0}$, the equations are:

$$T(z_0) = T_0$$

$$V(z_0) = V_0$$

$$\dot{m}_{0surf} Y_{k,0} - j_k(z_0) - \rho(z_0) u(z_0) Y_k(z_0) = 0$$

$$\rho(z_0) u(z_0) = \dot{m}_{0surf}$$

- Outlet boundary

For an outlet located at $z = z_0$, the equations are:

$$\Lambda(z_0) = 0$$

$$\left. \frac{\partial T}{\partial z} \right|_{z_0} = 0$$

$$\left. \frac{\partial Y_k}{\partial z} \right|_{z_0} = 0$$

$$V(z_0) = 0$$